UiO : University of Oslo

Henrik Eklund

Investigating dynamic small-scale events in the Sun with the Atacama Large Millimeter/sub-millimeter Array

Thesis submitted for the degree of Philosophiae Doctor

Institute of Theoretical Astrophysics
Faculty of Mathematics and Natural Sciences

Rosseland Centre for Solar Physics

2021

Series of dissertations submitted to the
Faculty of Mathematics and Natural Sciences, University of Oslo
No. 2435

ISSN 1501-7710

Cover: Hanne Baadsgaard Utigard.
Print production: Reprosentralen, University of Oslo.

Preface

This thesis, "Investigating dynamic small-scale events in the Sun with the Atacama Large Millimeter/sub-millimeter Array", has been written for the degree of *Philosophiae Doctor* at the University of Oslo. The research described here was conducted at the University of Oslo under supervision of assoc. professor Sven Wedemeyer. The research was supported by the Solar ALMA project which has received funding from the European Research Council, under the European Union's Horizon 2020 research and innovation programme (grant No. 682462), and the Research Council of Norway through its Centres of Excellence scheme (project No. 262622) for the Rosseland Centre for Solar Physics.

The aim of the Solar ALMA project is to facilitate novel observations of the Sun using the Atacama Large Millimeter/sub-millimeter Array, and provide science ready data for the solar physics community. As always, when applying new instrumental techniques, many challenges arise, which are brought out at all intermediate stages from the instrumental measurements, calibration, data reduction and post-processing and to the analysis of the resulting data. Much time and effort have went into the development of data-reduction techniques and calibration in order to establish data with high quality suitable for scientific analysis towards various scientific goals.

The nearby proximity of the Sun provides good opportunities to observe different phenomena at relatively small scales, but this also comes with challenges in the image reconstruction procedure. This along with the inherently high intensity and highly dynamic nature of the Sun, results in that well established tools and methodology that are applied for observations of other celestial targets do not function or are sub-optimal for solar observations. Behind the research presented in this thesis, thus lies much work which has been focused on, in particular, establishing reliable ways to reconstruct high-cadence time series of images of the interferometric measurements towards the Sun. The recent development of the Solar ALMA pipeline (SoAP) for producing science ready data from the measurements now facilitates meaningful analysis of the Solar ALMA data.

The thesis presents a collection of three papers. I am the first author and carried out most of the research for the development of all the included papers. In these papers we make use of the resulting science-ready data obtained with ALMA in combination with state-of-the art numerical simulations and co-observations with other instruments. The overall goal is to provide further understanding and aid in the analysis of small-scale events in the solar ALMA observations.

Acknowledgements

Firstly, I would like to acknowledge my supervisor Sven and co-authors, Mikołaj, Shahin and Juan, which is a majority of the solar ALMA group, and thank them for the help, valuable input and fruitful discussions throughout the last four years.

I also want to thank them along with the newer additions to the group and to closely related projects, Sneha, Atul, Maryam, Vasco and Daniel for motivating and inspiring discussions.

In addition I wish to thank all of my co-authors, including the ones not mentioned above, for the very constructive input, support and assistance in the development of the papers. I also wish to thank the IT-staff for supporting me with the computational infrastructure, that made it possible for me to conduct my research.

A special thanks goes to my initial office mates, including Charalambos and Max for a nice welcoming to the Institute of Theoretical Astrophysics, and to my current office mates Souvik and Juan for constantly providing support and a very nice and motivating climate, that makes it a pleasure to come to the office and spend the long hours working. Contributing to this, are of course also many other people in the Svein Rosseland building. I will not go into naming each and everyone here. The list would indeed get long. I wish to thank all my colleagues and guests at the Rosseland Centre for Solar Physics, and ITA, for all the nice times spent during lunches, coffee breaks and contributing to a nice working environment in general.

I want to thank everyone in my family, for the great moral support and unconditionally believing in me.

Last and mostly, I want to thank Reyna, for the moral support and understanding, and for helping me get through the tough times. Thank you (!) for all the inspiring discussions, the patience listening to my theories and for the valuable input you give, not only as a fellow physicist, but also as a loving partner.

Henrik Eklund
Oslo, August 2021

List of Papers

Paper I

Eklund, H.; Wedemeyer, S.; Szydlarski, M.; Jafarzadeh, S. and Guevara Gómez, J. C. "The Sun at millimeter wavelengths II. Small-scale dynamic events in ALMA Band 3". In: *Astronomy & Astrophysics*. Vol. 644, no. 152 (2020),

Paper II

Eklund, H.; Wedemeyer, S.; Snow, B.; Jess, D. B.; Jafarzadeh, S.; Grant, S. D. T.; Carlsson, M. and Szydlarski, M. "Characterisation of shock wave signatures at millimetre wavelengths from Bifrost simulations". In: *Philosophical Transactions of the Royal Society A*. Vol. 379, no. 20200185 (2021),

Paper III

Eklund, H.; Wedemeyer, S.; Szydlarski, M. and Jafarzadeh, S. "The Sun at millimeter wavelengths III. Impact of the spatial resolution on solar ALMA observations". *Submitted for publication in Astronomy & Astrophysics.*

Contents

List of Figures

List of Tables

Chapter 1

The structure of the Sun

1.1 Solar interior

Processes of nuclear fusion transforming hydrogen into helium are taking place in the core of the Sun, where the pressure and temperature are so high ($T \sim 15$ MK) that atomic nuclei get close enough to each other so that the Coulomb barrier can be overcome, primary by quantum tunneling. In the fusion-process, a large amount of energy is released. Outside the core, is the radiative zone which extends out to about 0.7 solar radii ($r_\odot \approx 7 \times 10^5$ km). The solar interior is highly opaque and an average single photon does not travel far before it is reabsorbed, after which it will be re-emitted in a random direction. This results in that the transport of an energy quanta to the solar surface takes long time, on average many thousands of years (Mitalas and Sills 1992). This process is the dominating energy transport process in the radiative zone. Further out, between $r = 0.7\ r_\odot - 1.0\ r_\odot$ is the convective zone, where transport of energy is largely dominated by the movements of the plasma convection. Heated plasma moves upwards. There is hot plasma moving upwards in the centre of the convection cells and cooler plasma moving down at the edges. The inner radiative zone rotates largely as a rigid body and the outer convective zone exhibits a differential rotation with a greater speed at the equator than at the poles. Between these two zones, a large shear is displayed, in a thin layer region referred to as the tachocline (Spiegel and Zahn 1992).

The motions of the plasma and the transport of energy through the different layers in the solar interior play an important role in the global conditions of the solar atmosphere.

1.2 Solar atmosphere

At heights larger than 1.0 $r_\odot$, the overlying medium is largely optically thin for electromagnetic radiation and thus constitutes the atmosphere of the Sun. In Figure 1.1, the general atmospheric structure of the solar atmosphere and the average temperature and density of the different layers are shown, according to the one-dimensional (1D) VAL model (Vernazza, Avrett, and Loeser 1981).

The photosphere around the height of $r = 1.0\ r_\odot$ (i.e., height equal to zero in Figure 1.1) marks the lower boundary of the solar atmosphere. More specifically, the height of the photosphere is usually defined as where radiation at a wavelength of 500 nm has an optical depth of unity, which effectively means that approximately 50% of the photons will escape (Hubeny and Mihalas 2014). The photosphere has a thickness of a few hundreds of km, usually defined with an average upper limit of 500 km. The temperature of the photosphere is on

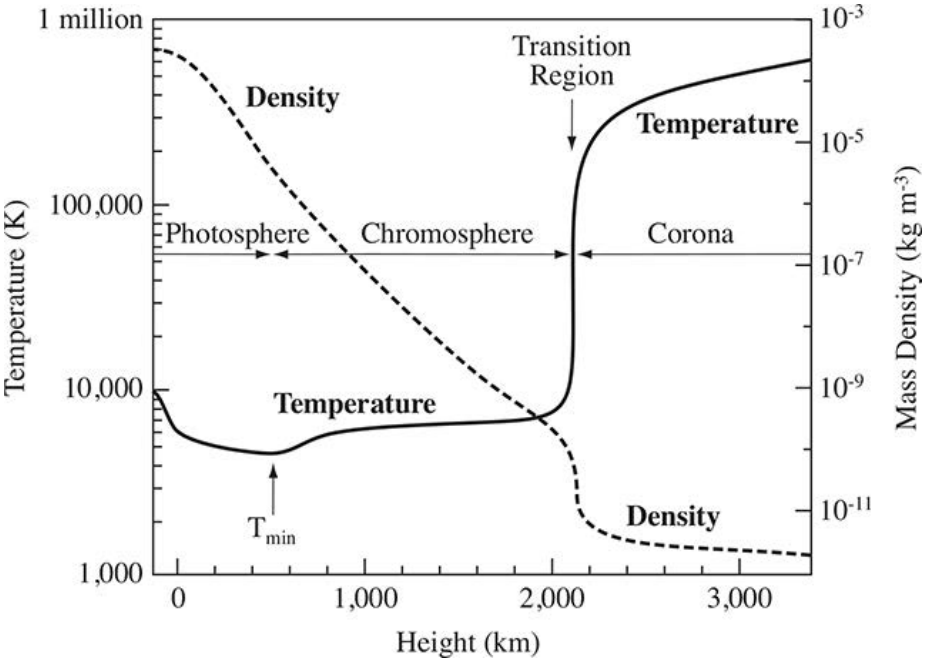

Figure 1.1: The average temperature and density, in accordance to the VAL model (Vernazza, Avrett, and Loeser 1981), of the different layers in the solar atmosphere, as a function of height. (Courtesy of Eugene H. Avrett).

average about 6 kK and is decreasing with increasing height out to approximately 3.8 kK (Avrett 2003) at the temperature minimum ($T_{\rm min}$; see Figure 1.1). The photosphere is largely dominated by a pattern of granules, originating from the convection cells in the underlying layer.

Above the photosphere is the chromosphere. The chromosphere shows an average temperature of about 3.8 kK at the lower boundary and increase on average with increasing height. The chromosphere is highly dynamic with variations on small spatial and temporal scales, which makes it difficult to define precise heights for the lower or upper boundaries. However, the average extent of the chromosphere can be estimated to be between roughly 0.5–2.5 Mm.

Above the chromosphere lies the transition region, where a steep rise in temperature is seen with increasing height, connecting the chromosphere with temperatures of a few thousands of K to the corona with temperatures of up to several millions K. The corona constitutes the top layer of the atmosphere. The transport of energy from the photosphere to the upper layers of the solar atmosphere is not fully understood yet, nor how the energy is dissipated at different heights. Many processes have been proposed to explain and fit observational constraints to current theoretical models.

The temperatures indicated here are based on the VAL model and could be

considered as an average of the actual temperatures which can vary significantly, in particular at small scales, depending on the dynamical processes taking place. The chromosphere is heavily dynamic with many different phenomena taking place, on different spatial and temporal scales.

The dominating phenomena are very dependent on the strength and topology of the magnetic field. There are regions with high magnetic field strengths, referred to as an active region. Sunspots or plage regions are indicators of active regions. Various dynamic processes can take place in *active regions*, some seemingly more energetic than others, such as solar flares and coronal mass ejections. Regions with generally lower magnetic field strengths often displaying closed magnetic field lines, are referred to as *quiet Sun*. In the photosphere of a quiet Sun region, the hydrodynamic pressure dominates over the magnetic pressure. The convective motions therefore advect the magnetic field horizontally from the centre towards the edges of the granules (Galloway and Weiss 1981), giving rise to a weak magnetic field in the granular cells and magnetic field concentrations in the intergranular pattern (Steiner et al. 2008). At larger scales, between supergranular cells ($\sim$ 30 Mm; Rieutord and Rincon 2010), network patches with concentrations of magnetic field strength on the order of thousands of Gauss can form. In the network patches, the magnetic field lines extend up into the chromosphere, forming canopies of closed loops by connecting to another network patch with opposite polarity, or even extend further up in the corona (Wedemeyer-Böhm, Lagg, and Nordlund 2009). Between the network patches, in the inter-network regions, the magnetic field strength remains low, on the order of up to hundreds of Gauss. With increasing height in the atmosphere, the magnetic pressure becomes increasingly dominant over the hydrodynamic gas pressure and the magnetic field lines far up in the atmosphere therefore tend to spread out. The magnetic field lines stretching up through chromosphere can interfere with the upwardly propagating acoustic waves. Much depending on the inclination of the magnetic field lines (Hasan, Steiner, and van Ballegooijen 2008), the acoustic waves can be refracted, reflected or even change wave mode, to magnetoacoustic waves (Bogdan et al. 2003; Rosenthal et al. 2002).

The quiet Sun atmosphere is characterised by propagating acoustic waves that are excited by the motions at the top of the convection zone. As the acoustic waves propagate upwards into the atmosphere, they steepen into shock waves because of the decreasing density. The density of the atmosphere is steadily decreasing (on average) with increasing height (see Figure 1.1). Therefore, there are many shock waves propagating through the chromosphere, which we in chapter 2.2 will see is the layer of origin of continuum radiation at mm-wavelengths.

In the current work, presented in this thesis, the scientific analysis is focused on predicting, detecting and analysing signatures of propagating shock waves in mm-wavelength observations of the quiet Sun.

Chapter 2

Radiation at mm and sub-mm wavelengths

Ever since the first detection of the first absorption lines in the solar spectra (Hyde Wollaston 1802), spectral lines have been a very central tool in the analysis and interpretation of the solar atmosphere. Measuring spectral lines at mm-wavelengths in the solar atmosphere have been shown to be a difficult task (see e.g., Berger and Simon 1972, Shimabukuro and Wilson 1973). However, there have been detections of spectral lines at sub-mm wavelengths. The neutral hydrogen line of HI between electron levels n=20-19 (0.34 mm; Clark, Naylor, and Davis 2000a) and then shortly afterwards the HI 22-21 line (0.45 mm; Clark, Naylor, and Davis 2000b), are the spectral lines observed in the Sun with the longest wavelengths. The Atacama Large Millimeter/sub-millimeter Array (ALMA; further discussed in section 3.2) provides a new valuable tool for solar observations. The wavelengths of the HI n=20-19 and HI 22-21 lines fall within the ALMA spectral receiver bands 9 and 10 (cf., Table 1 in paper III; Eklund, Wedemeyer, Szydlarski, and Jafarzadeh 2021). These receiver bands are so far not offered for solar observations, but only receiver bands measuring radiation at longer wavelengths (0.85 mm – 3.26 mm) are offered (further discussed in section 3.2). Spectral lines at longer wavelengths, within receiver bands offered for solar observations, are presumably too weak because of increasing line broadening (Hoang-Binh et al. 1987; Khersonskii and Varshalovich 1980).

In the current work, we therefore resort to measurements and analysis of the continuum intensities.

2.1 Continuum radiation formation

The continuum radiation at mm or sub-mm wavelengths of the solar atmosphere is mostly produced by free-free emission from interactions between electrons and positively charged ionized atoms. The energies of the unbound electrons are non-quantized and thus radiation at all energies are allowed, giving rise to the continuum. The process of the free-free radiation is thermal and can be considered to form under the conditions of local thermodynamic equilibrium (LTE). Under LTE-conditions, the spectral distribution of the radiation is represented by a black body, given by Planck's law

$$B_\nu(T) = \frac{2h\nu^3}{c^2}\frac{1}{e^{h\nu/kT} - 1} \tag{2.1}$$

where h is the Planck constant, ν the frequency, c the speed of light, k is the Boltzmann constant and T the temperature of the plasma. In the regime of the Rayleigh-Jeans law $h\nu \ll kT$, which is the case at mm- and sub-mm wavelengths ($0.32 - 3.6$ mm; $84 - 950$ GHz observable with ALMA) and solar temperatures of several thousand K, the exponential term can be estimated by the expansion

$$e^{h\nu/kT} \approx 1 + \frac{h\nu}{kT}, \tag{2.2}$$

so that Eq. (2.1) can be rewritten as

$$B_\nu(T) = \frac{2\nu^2}{c^2} kT. \tag{2.3}$$

The brightness is thus linearly dependent on the temperature. The temperature which gives the same brightness as the black body radiation at a certain frequency, i.e.,

$$B_\nu(T_\mathrm{b}) = I_\nu, \tag{2.4}$$

is referred to as the brightness temperature, which is given by

$$T_b = \frac{c^2}{2k\nu^2} I_\nu. \tag{2.5}$$

The brightness temperature is linked to the thermodynamic gas temperature (T_g) of the source as

$$T_\mathrm{b} = \int_{-\infty}^{\infty} dz \chi_\nu T_\mathrm{g} e^{-\tau_\nu(z)}, \tag{2.6}$$

where χ_ν is the opacity and $\tau_\nu(z)$ is the optical depth defined as

$$\tau_\nu(z) = \int_z^{\infty} dz \chi_\nu, \tag{2.7}$$

which for an optically thin target ($\tau_\nu \ll 1.0$), leads to $T_\mathrm{b} = \tau_\nu T_\mathrm{g}$ and for an optically thick target ($\tau_\nu \gg 1.0$), $T_b = T_\mathrm{g}$. These approximations are however assuming that the target is homogeneous and have large angular size.

The formation of continuum radiation at mm- and sub-mm wavelengths under LTE-conditions provides a straightforward way to get indications on the plasma temperature in comparison to other so far commonly used chromospheric diagnostic techniques for radiation at optical, ultraviolet or infrared wavelengths. The latter are often formed under non-LTE conditions (Carlsson, De Pontieu, and Hansteen 2019; de la Cruz Rodrıguez and van Noort 2017), which complicates the interpretation of the observations. Measurements of the intensities at mm- and sub-mm wavelengths provide an excellent tool for studying small-scale structures and transport of heat in the dynamic chromosphere. However, there are other challenges that come with performing observations at mm-wavelengths, such as the wavelength-dependent angular resolution, with decreasing resolution for increasing wavelength, which we discuss further in Chapter 3.

2.2 Formation heights

The continuum radiation at mm and sub-mm wavelengths from the Sun originates mostly from chromospheric heights (see e.g., Vernazza, Avrett, and Loeser 1981; Wedemeyer, Bastian, et al. 2016). The wavelength dependency of the opacity causes the average height of formation to vary with wavelength as well, where the average height of formation is increasing with wavelength. Estimations of the formation heights based on three-dimensional (3D) numerical modeling of the quiet Sun were conducted by Wedemeyer-Böhm, Ludwig, et al. 2007, where the average contribution function showed a maximum at a height of 490 km at $\lambda = 0.3$ mm close to the classical temperature minimum (cf. Figure 1.1), 730 km at $\lambda = 1.0$ mm to 960 km at $\lambda = 3.0$ mm. This agrees well with the radiative transfer calculations based on other numerical models. Loukitcheva, Solanki, Carlsson, and White 2015 performed calculations on the Bifrost enhanced-network 3D model (see section 4.1) which exhibits larger magnetic field strengths, where average heights of formation between 900 km at $\lambda = 1.0$ mm and 1500 km at $\lambda = 3.0$ mm, were reported. The larger average heights compared to Wedemeyer-Böhm, Ludwig, et al. 2007, can be explained by the presence of canopies formed by magnetic field loops through the chromosphere, which display increasing optically thickness with increasing wavelength (Eklund, Wedemeyer, Szydlarski, and Jafarzadeh 2021 Eklund et al 2021; paper III).

Martınez-Sykora et al. 2020 conducted calculations of synthetic observables from 2D atmospheric models with different methods for treating the ionization balance: (*i*) in LTE and (*ii*) non-equilibrium for hydrogen and helium. They report resulting average formation heights for the two different cases of (*i*) 0.9 Mm and (*ii*) 2.7 Mm at $\lambda = 1.2$ mm, and (*i*) 1.8 Mm and (*ii*) 2.8 Mm at $\lambda = 3.0$ mm, respectively. The first approach (*i*), shows agreement of the average formation heights reported by previous studies based on 3D models as mentioned above (Loukitcheva, Solanki, Carlsson, and White 2015; Wedemeyer-Böhm, Ludwig, et al. 2007. The second approach (*ii*), however, shows a significantly larger average formation height, at both $\lambda = 1.2$ mm and $\lambda = 3.0$ mm. For the second approach (*ii*) in Martınez-Sykora et al. 2020, the difference in average formation height between $\lambda = 1.2$ mm and $\lambda = 3.0$ mm is very small (about 0.11 Mm). Hence, the continuum radiation at both wavelengths is optically thick and samples the basically the same structures at high altitudes, which is contradictory to the results based on the Bifrost 3D model (Loukitcheva, Solanki, Carlsson, and White 2015, Eklund et al 2021; paper III). Observations of similar structures as presented in the 2D simulations of Martınez-Sykora et al. 2020 at the two wavelengths would provide constraints that could clarify how realistic the models are and how to potentially improve them to reproduce the millimetre observations. In this regard, observing features with presumably large formation heights like, for instance, magnetic loop structures as reported by Wedemeyer, Szydlarski, et al. 2020, could be useful to give further clarity.

Loukitcheva, Solanki, Carlsson, and Stein 2004 showed that for a time-dependent 1D simulation with propagating shock waves, the height of formation varies significantly at mm-wavelengths as the shocks disturb the chromosphere.

In common for the studies of the dynamic 1D models or the models in 2D and 3D, is that they display that the formation height varies considerably with the small-scale dynamical structure of the chromosphere. This is obviously lacking in static classical 1D models such as the VAL (Vernazza, Avrett, and Loeser 1981) or FAL models (Fontenla, Avrett, and Loeser 1993).

Finally, as a consequence of the wavelength dependency of the opacity, the sequential order of formation heights of the radiation at two wavelengths remain the same. For instance, the height of optical depth unity of continuum radiation at 3.0 mm is at larger heights than for the 1.0 mm radiation. Based on radiative transfer calculations from numerical 3D Bifrost model (further discussed in Chapter 4), we see that this is valid also at relatively small differences in wavelength, i.e., between the sub-bands of the ALMA receiver bands (see Section 3.2). As a result that the order of formation with height of the sub-bands are definite, it follows that the slope of the brightness temperature within a receiver band could provide valuable information on the local plasma temperature gradient at the sampled layers, further discussed in Section 5.3.

Chapter 3

Interferometric radio observations

3.1 Introduction to interferometric radio observations

The angular resolution θ, that can be achieved with an antenna scales with the wavelength of the radiation (λ) and the diameter of the antenna (d) and can be roughly estimated according to

$$\theta \simeq \epsilon \frac{\lambda}{d} \tag{3.1}$$

where ϵ is a numerical factor, often ~ 1.22 for many apertures, originating from the minimum distance between two points sources in the diffraction pattern to resolve them separately.

For comparison, typical (wavelength dependent) angular resolution of solar observations at optical wavelengths is for example around 0.13 arcsec for the Swedish 1-m Solar Telescope or 0.08 arcsec for the GREGOR 1.5-m Solar Telescope (Schmidt et al. 2012). To achieve similar angular resolution in radio observations, we see from relation (3.1) that for example, at a wavelength of 1 mm, an antenna diameter of approximately 2 km would be necessary. Building such large antennas is clearly technically challenging and not very economically feasible. Instead, aperture synthesis can be used where several antennas are targeting the same source and simultaneously measure the amplitude and phase of the radiation emitted by that source. Fortunately, because of the low frequencies in the radio regime, the phase correlation can be done electronically, in contrast to for instance in optical wavelengths, so that the instrumental setup becomes less costly.

The separation of the antennas determines the sampling in Fourier space. The separation between two antennas is referred to as a *baseline*. The plane perpendicular to the line-of-sight to the target source, is referred to as the uv-plane, (with the third dimension w being aligned to the line-of-sight), where the units are represented in multiples of the wavelength. A measurement on one particular baseline provides one visibility in the uv-space (in the case of monochromatic measurements), at the distance from the centre relative to the length of the baseline and at the angle determined by the angle of the baseline relative to the reference system. Each pair of antennas (A_1, A_2) provides two baselines ($A_1 \rightarrow A_2$ and $A_2 \rightarrow A_1$) and thus gives rise to two visibilities in the uv-space, with same distance from the centre, but at an rotation of angle π radians relative to each other. However, these two visibilites samples the same angular scale and orientation and the effective amount of visibilites are half.

Therefore, the total number of unique baselines n' scales with the number of antennas n as

$$n' = \frac{n^2 - n}{2} \tag{3.2}$$

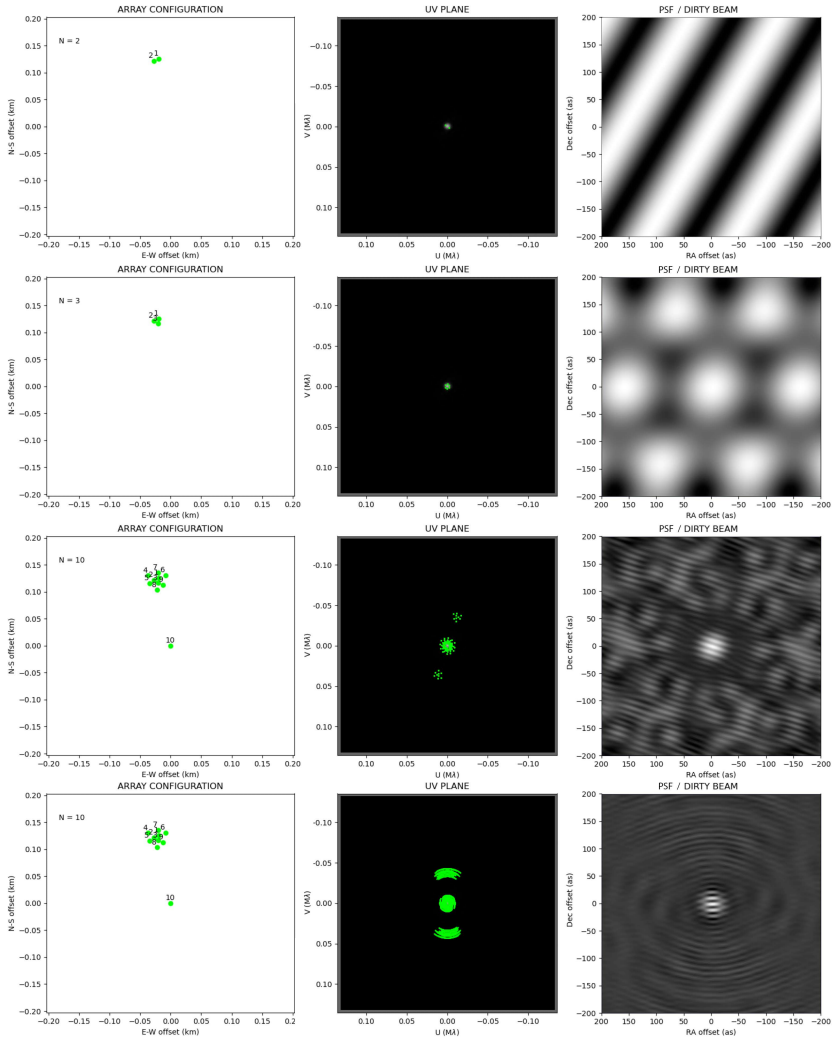

Figure 3.1: View of different configurations of antennas (left column) with the sampling in the *uv*-space (middle column) and the resulting PSF (right column). The sampling is monochromatic with a wavelength of 3 mm. Top row: Using only two antennas, the *uv*-sampling is performed only at one spatial scale and one angle, giving rise to the fringes in the PSF (dirty beam). Second row: The case of three antennas in an equilateral triangular formation samples the same scale at three different angles. Third row: a cluster of 9 antennas with an additional 10th antenna located far away. Large scales are reasonably well sampled, but small scales are only sampled in one direction. Bottom row: Same as the case in the third row, with integration time of 6 hours, (instead of snapshots as above) largely increasing the *uv*-sampling, improving the resulting PSF (see main text).

Figure 3.1 shows the relative distances between the antennas for examples of simple interferometric arrays with 2 to 11 antennas, along with the sampling in the *uv*-space and the resulting point spread function (PSF), also referred to as the *dirty beam*). The calculations are performed using the Aperture Synthesis Simulator (APSYNSIM) (Marti-Vidal 2017). In the first case, there are only two antennas, so that only one scale is sampled at one specific angle. The PSF therefore show the simple fringe pattern. When adding one antenna, forming an equilateral triangle, there is still only one spatial scale sampled. The resulting PSF has the shape of a rounded hexagon-type of pattern. When adding several antennas in a small cluster, slightly different scales at different angles are sampled. The larger scales are then more well sampled and the main lobe of the PSF becomes dominant. Then, when adding one additional antenna at a relatively far-away distance, the *uv*-space is boosted by well separated visibilities (third row of Figure 3.1). In this case, also smaller scales are sampled, along the axis of the well-separated visibilities in the *uv*-space. This is seen in the PSF by the wiggly small-scale pattern with lines crossing from the left-top to the bottom-right corner (the wave-like pattern seen instead of straight lines as in the first case, originates from the slight variation of the relative angles of the visibilities). The sampling in the *uv*-space consequently defines which scales and at what angles those scales are mapped.

In general, a large evenly distributed *uv*-sampling allows for more refined measurements. To acquire larger sampling in the *uv*-space, one could technically alternate the positions of the antennas. This is a difficult task to perform mechanically, but the technique is very often applied by using the rotation of Earth, which effectively changes the angles of the baselines, relative to the target source. This technique is referred to as *Earth-rotation aperture synthesis*. In the bottom row of Figure 3.1, the same example antenna array with 10 antennas as above is shown, but for an integration time of 6 hours, instead of the instantaneous sampling as shown above. The visibilities are sampled along curved lines in the *uv*-space as a result of Earth's rotation. The resulting PSF is significantly refined, with relatively larger contrast between the central main lobe and the side lobes. Still evident is the small-scale fringe pattern because of the sparse sampling with only one long baseline. Adding even more antennas with different relative sizes and angles of the baselines would further improve the sampling of visibilities in the *uv*-space. Although, as a result of the dynamics at short time-scales seen in the chromosphere (Section 1.2), the Earth rotation synthesis can not be used in the case of solar observations. In order to resolve the small-scale structures that show short dynamical time-scales, high cadence imaging is required.

In addition, as the visibilities are wavelength dependent, the visibilities in the *uv*-space can also be increased by measuring at several frequencies simultaneously, thus increasing the bandwidth of the measurement. In the examples displayed in Figure 3.1, we only consider the case of monochromatic measurements (at 3 mm). Increasing the bandwidth, to for instance that corresponding to the ALMA receiver bands (Section 3.1.1), provides larger sampling of scales but keeping the angles that are sampled constant. One monochromatic visibility-point in the

uv-space would thus instead form a line, extending in radial direction, with a length relative to the bandwidth.

3.1.1 Atacama Large Millimeter/sub-millimeter Array

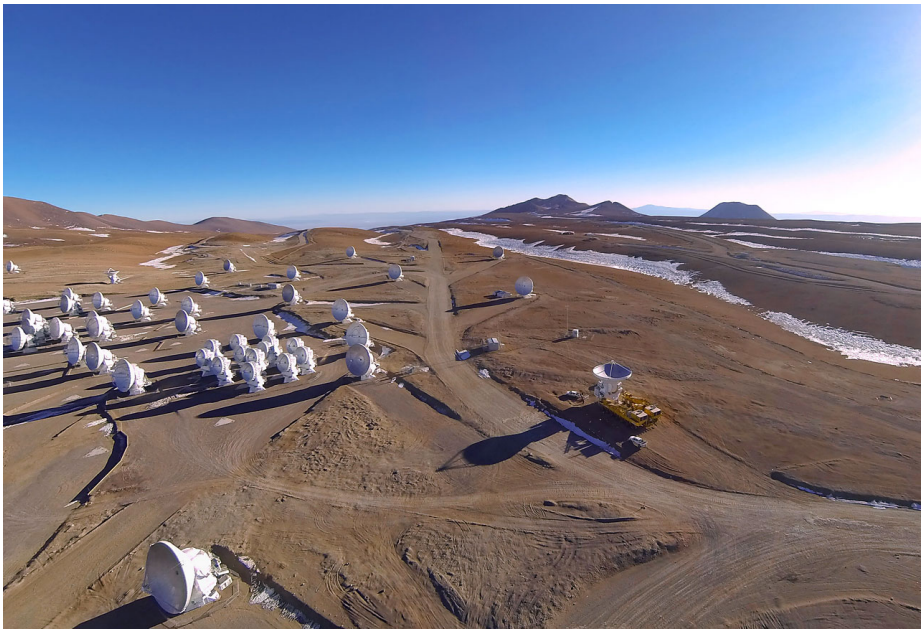

Figure 3.2: A view of a part of ALMA. The densely populated Atacama Compact Array with twelve 7-m antennas are seen in the centre, surrounded by the four total power antennas and a number of antennas from the main array, which extends several km, outside the limits of the photograph. Credit: A. Marinkovic/X-Cam/ALMA (ESO/NAOJ/NRAO)

For the current research, the Atacama Large Millimeter/sub-millimeter Array (ALMA)[1], located at the Chajnantor plateau in Chile, is used. ALMA consists of a total of 66 antennas with fifty antennas of 12-m diameter forming the main interferometric array. Twelve antennas of 7-m together with an additional four antennas of 12-m make up the Atacama Compact Array (ACA; Iguchi et al. 2009). The ACA and part of the main array is shown in Figure 3.2. The objective of the main interferometer is to perform measurements at small angular scales with baselines of up to $\sim$ 16 km, while the ACA measures large scales. The four 12 m antennas in the ACA, referred to as the total-power (TP) antennas, are used for single-dish measurements and thus measure the largest scales. The antennas of ALMA are mobile and can be moved to accommodate different baseline-configurations. The process of moving the heavy antennas is not an easy

[1] https://www.almaobservatory.org

task, as visible in Figure 3.3, where the action of moving one of the 12 m antenna is shown. The configuration of ACA is so-far kept constant, with baselines between 9–45 m, but the 12-m array is reconfigured throughout each observing cycle. There are 10 configurations, from the most compact configuration C1 with a maximum baseline of about 0.16 km to the most extended configuration C10 with a maximum baseline of about 16.0 km (Braatz et al. 2021). With a minimum baseline of the 12 m array of 15 m, the combination of the 12 m array, the 7 m array and the TP antennas thus offers measurements at all lengths of baselines between 0 m and 16 km.

Figure 3.3: The process of moving an ALMA antenna. Seen in the photographs are the specially designed, large, high-power vehicles required to be able to move the about 100 tonnes heavy 12-m antennas at the 5 km high altitude of the ALMA site at the Chajnantor plateau. Credit: ESO/T. van Kempen (left) and AUI/NRAO, Carlos Padilla (right).

All the antennas of ALMA are foreseen to be equipped with receivers that can measure ten frequency bands ranging between 35–950 GHz, but observations are currently only offered for bands 3–10 between 84–950 GHz (0.32–3.6 mm; Braatz et al. 2021). The receiver bands have a bandwidth of 8 GHz and measurements can only be performed for one receiver band at a time. The spectral resolution of the measurements varies (depending on the correlator mode), between 0.0305 MHz and 31.2 MHz (Remijan et al. 2020).

The combination of the 12-m array and ACA, with a total of 62 antennas, amounts to a total number of 1891 baselines. The locations of the antennas in the different configurations are well considered to create an even nearly Gaussian-shaped distribution of sampling in the uv-space. In Figure 3.4, the positions of the ALMA antennas with the 12 m array in configuration C4 is shown with the corresponding sampling in uv-space for a snapshot measurement of only 1 s integration at ALMA receiver band 3 ($\lambda = 3$ mm), with the bandwidth of 2 GHz. The Fourier space is very well sampled in comparison to other interferometers with fewer antennas, such as the example with 10 antennas in Section 3.1 (third row in Figure 3.1), where the first nine correspond to a part of the 7 m array and

the tenth represents one antenna in the 12 m array. The resulting PSF for the full ALMA array shows a clear main lobe and only a very weak side-lobe pattern, which allows for very precise measurements. The sensitivity is proportional to the total surface area, that consequently depends on the number of antennas and their individual sizes. With a relatively high angular resolution and sensitivity, ALMA provides a very good tool to study the chromosphere of the Sun.

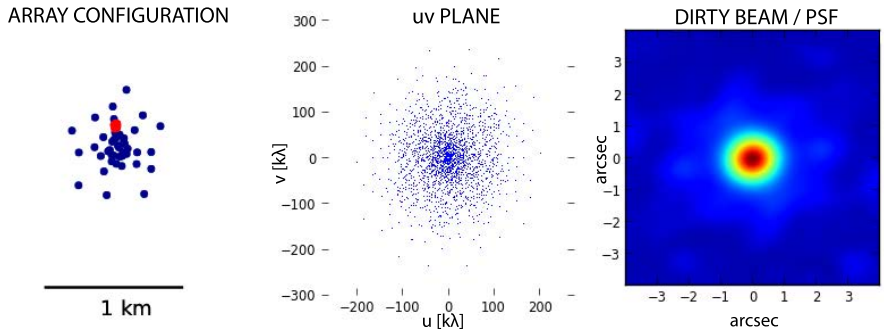

Figure 3.4: Example of array configuration of ALMA with the corresponding *uv*-sampling and PSF. Left panel: The physical distribution of the antennas of the 7 m array (red markers) and the 12 m array in array configuration C4 (blue markers). Middle panel: The sampling in the *uv*-plane for a 1 s measurement in band 3, with 2 GHz bandwidth. Right panel: The resulting PSF of the measurement. The image is partly produced with output from the CASA task simalma[2].

The field of view (FOV) of the resulting measurement is directly related to the primary beam response of the individual antennas (equivalent to the PSF of a single antenna) and the wavelength of the radiation. Longer wavelengths result in larger FOV according to the relation (Remijan et al. 2020; Wedemeyer, Bastian, et al. 2016):

$$\theta_{\mathrm{FOV}} \approx 1.13 \frac{\lambda}{D} \approx 19 \left. \frac{\lambda}{\mathrm{mm}} \right|_{\mathrm{D=12\ m}} \mathrm{arsec} \tag{3.3}$$

This corresponds to $\theta_{\mathrm{FOV}} \approx 19$ arcsec for measurements at 1 mm and $\theta_{\mathrm{FOV}} \approx 57$ arcsec at 3 mm. The primary beam response can be approximated by a Gaussian distribution and the sensitivity is thus maximal in the center and declining towards the edges. It therefore makes sense to limit the observations to the area with decently large sensitivity. Most common is to limit the primary beam response to around 0.5 or 0.3 of the full width at half maximum (FWHM). The lower values, providing slightly larger FOV have been found useful especially in co-alignment of co-observations with other instruments (Section 5.4).

3.2 Solar ALMA observations and post-processing imaging techniques to produce science ready data

3.2.1 Observing the Sun with ALMA

The first regular observations of the Sun with ALMA were conducted in 2016 (cycle 4). At the time of starting the work of this thesis in 2017, there were still almost no publications reporting results from the analysis of solar ALMA data.

The scope was therefore to first develop and refine the methods of handling the solar ALMA data so that meaningful scientific interpretations could be made and then when applying the resulting methods to the observational data, report what features are seen and to what degree the interpretation makes sense. This was thus the primary scope of paper I in this thesis (Eklund, Wedemeyer, Szydlarski, Jafarzadeh, and Guevara Gómez 2020).

Since then there have been several reports on solar ALMA data with various scientific goals, reporting observations of various phenomena, including sunspots (Jafarzadeh, Wedemeyer, Szydlarski, et al. 2019; Rodger et al. 2019), chromospheric plages (Chintzoglou et al. 2021b), type II spicules (Chintzoglou et al. 2021a), on-limb spicules (Shimojo, Kawate, et al. 2020), oscillations (Guevara Gómez et al. 2021; Jafarzadeh, Wedemeyer, Fleck, et al. 2021; Patsourakos et al. 2020) and transient brightening events (da Silva Santos et al. 2020; Eklund, Wedemeyer, Szydlarski, Jafarzadeh, and Guevara Gómez 2020; Molnar et al. 2019; Nindos, Alissandrakis, et al. 2020; Nindos, Patsourakos, et al. 2021; Shimojo, Hudson, et al. 2017).

Solar observations with ALMA are still offered only as a non-standard mode and there are certain restrictions in place. These restrictions are always carefully described in the proposer's guide for ALMA observations (Braatz et al. 2021). As of observation cycle 8 (2021), observations are still limited to linearly polarized (XX and YY) continuum measurements in bands 3,5,6 and 7. The range of wavelengths and frequency for the receiver band setups for the solar observing mode are given in Table 3.1. Each receiver band has four sub-bands (SB), each with a bandwidth of 2 GHz, containing 128 spectral channels, each with a width of 15.6 Mhz. The SB's are here numbered from 1 to 4, preceded by the receiver band number for clarity (e.g., first sub-band of band 3 is noted as SB3.1). Solar observations are performed with a combination of both the 12-m array and ACA, with the 12 m array constrained to the more compact configurations. As mentioned in Section. 3.1.1, the ACA antennas are standing physically close together, so that they are likely to shadow each other for targets closer to the horizon. Shadowing is when one antenna is physically blocking the incoming radiation from reaching another antenna. For that reason, solar observations are restricted to be performed during the hours of the day when the Sun stands high on the sky. However, antennas that happen to be shadowed are removed from the measurement set during the pre-calibration. The altitude of the target on the sky is in addition important because of the resulting shape of the PSF. The closer the target is to the horizon, the resulting PSF is increasingly eccentric, which introduces quite severe uncertainties to in particularly analysis of small-scale

structures. This issue is discussed in paper III presented in this thesis.

Apart from the restrictions mentioned above, there are certain requirements specific for observing the Sun. As a consequence of the heavily dynamic nature of the chromosphere with small-scale phenomena evolving at short time-scales, a high cadence is necessary to be able to properly resolve them. In the first observational cycles, a cadence of 2 s were offered. Please note that the data used in paper I (Eklund, Wedemeyer, Szydlarski, Jafarzadeh, and Guevara Gómez 2020) have a cadence of 2 s. As for now, a higher cadence of 1 s is offered.

The interferometric measurements probe relative differences in intensity or brightness temperature (following the Rayleigh-Jeans approximation; 2.1). In addition to the relative interferometric intensity measurements, the total-power antennas, probing the short spacing baselines up to 12 m, are used to measure the average temperature of the Sun. The measurements are performed by a repetitive cyclic motion over the entire solar disc, during the time of the interferometric observations. These measurements are then used to scale the interferometric measurements to absolute temperatures.

Finally, it should be pointed out that the very high intensity of the Sun consequently saturates the Water Vapor Radiometer (WVR) receivers and simultaneous measurements can not be done for solar measurements (Braatz et al. 2021). The measurements can therefore not be corrected for the phase shifts coming from the atmospheric water vapor above the telescopes.

3.2.2 Image reconstruction of high cadence time-series

Because of the necessity of high-cadence time-series for solar ALMA data, challenges are encountered that typically do not arise for radio-observations of other more static targets. In particular, there are two main issues. (i) The high cadence time-series require correction of the *seeing* effects. (ii) The contribution that the side-lobes of the PSF bring to the data should be removed.

In order to make it easy for the general solar physics community to make use of and analyze solar ALMA data, the Solar ALMA Pipeline (SoAP) has been developed by the solar ALMA group in Oslo[3]. In particular, SoAP is tailored to take care of these issues through (i) self-calibration of phase variations and (ii) deconvolution of the measured data, further described below. SoAP is a python based code, calling on necessary tools in CASA (Common Astronomy Software Applications package[4]) for performing post-processing of the observational data to construct high-cadence time series ready for scientific analysis. We also put efforts into implementing the compatibility of performing image reconstruction of synthetic measurement sets, constructed by simulated observations corresponding to that of the different ALMA bands towards numerical models. Detailed specifics on the functionality of SoAP and a guide on how to use it will be summarized in a future publication. Figure 3.5 shows an example image of the resulting output

[3]SoAP has been developed under the SolarALMA project which has received funding from the European Research Council (ERC) under the European Union's Horizon 2020 research and innovation programme (grant agreement No. 682462)

[4]https://casa.nrao.edu

Receiver band	Sub-band	Wavelength [mm] min	mid	max	Frequency [GHz] min	mid	max
B3	SB3.1	3.1893	3.2236	3.2586	92.0	93.0	94.0
	SB3.2	3.1228	3.1557	3.1893	94.0	95.0	96.0
	SB3.3	2.8282	2.8552	2.8826	104.0	105.0	106.0
	SB3.4	2.7759	2.8018	2.8282	106.0	107.0	108.0
B5	SB5.1	1.5614	1.5696	1.5779	190.0	191.0	192.0
	SB5.2	1.5453	1.5533	1.5614	192.0	193.0	194.0
	SB5.3	1.4696	1.4768	1.4841	202.0	203.0	204.0
	SB5.4	1.4553	1.4624	1.4696	204.0	205.0	206.0
B6	SB6.1	1.2978	1.3034	1.3091	229.0	230.0	231.0
	SB6.2	1.2867	1.2922	1.2978	231.0	232.0	233.0
	SB6.3	1.2137	1.2187	1.2236	245.0	246.0	247.0
	SB6.4	1.2040	1.2088	1.2137	247.0	248.0	249.0
B7	SB7.1	0.8802	0.8828	0.8854	338.6	339.6	340.6
	SB7.2	0.8751	0.8776	0.8802	340.6	341.6	342.6
	SB7.3	0.8502	0.8527	0.8551	350.6	351.6	352.6
	SB7.4	0.8454	0.8478	0.8502	352.6	353.6	354.6

Table 3.1: Wavelengths and frequencies of the receiver bands currently offered for solar observations.

from the high cadence time series (2 s) at band 3 data. The image comes from the same data set that is used in paper I and Wedemeyer, Szydlarski, et al. 2020.

There are variations in the column mass in the Earth's atmosphere above the telescopes, due to changes in temperature, pressure, density or interfering particles, that cause variations of the diffraction index. This is referred to as *seeing*. The varying seeing conditions manifest themselves as fluctuations in phase measured across antenna baselines. The timescale of the phase fluctuations depends on the current atmospheric conditions, but is most often present on timescales as low as on the order of 1 s. This causes a certain feature, e.g., a point source, to move around in the FOV, often to a significant degree that the interpretation of the data is influenced. Observations of other celestial targets, for instance a star-forming cloud or an unresolved stellar point-source, allow and often require integration and averages of the intensities over a long period of time. This partly averaging out the phase fluctuations, but corrections based on measurements of the water vapor can also be made. However, for observations of the bright Sun, a short integration of 1 s, or even less is enough and the resulting spatial smearing is minimal. But as a result, the FOV is somewhat warped and the location of certain features varies slightly from one time-step to the next. Since measurements of the density fluctuations from the water vapor above the telescopes can not be performed during solar observations, a

self-calibrated phase-correlation technique is performed in order to stabilize the time-series.

In addition, gridding of the measured data is performed and a deconcolver technique is applied to take care of the side-lobe pattern. One of the most widely used deconvolver techniques in radio interferometry, is the CLEAN algorithm (Högbom 1974). Such an algorithm aims to remove the impact of the side-lobes of the PSF from the data and only leave the contribution from the main-lobe. The main lobe of the PSF is referred to as the *clean beam*.

The CLEAN algorithm is an iterative procedure, stepping through the data many times. In each iteration it finds the brightest point in the data (the "dirty image"), subtracting a fraction of this point (referred to as the gain-factor), convolved with the PSF. The point source convolved with the clean beam is saved to the resulting model image ("clean image"). The process is continued until the brightest point in the data lies under a pre-defined threshold level. It is optimal for targets consisting of a small number of well-separated point-like sources and is sub-optimal for extended targets with non Gaussian structures. As the chromosphere inherently has a very complex structure, it is expected to introduce a certain amount of noise to the data. For that reason the analysis of the resulting data should be conducted in a conservative manner, also taking this into account to the total uncertainty.

Implemented in SoAP is the Multi-scale CLEAN algorithm (Cornwell 2008), which is an extension of the classical CLEAN method, where components at a pre-defined range of different spatial scales are considered simultaneously.

Other approaches could potentially be used, such as the maximum entropy method (MEM; Cornwell and Evans 1985) or methods based on statistical grounds from synthetic measurements towards numerical simulation, with potential implementation through machine learning techniques. However, until such methods are well implemented and carefully tested, the CLEAN algorithm provides a very good first step to deconvolve the data, enabling to perform meaningful scientific analysis.

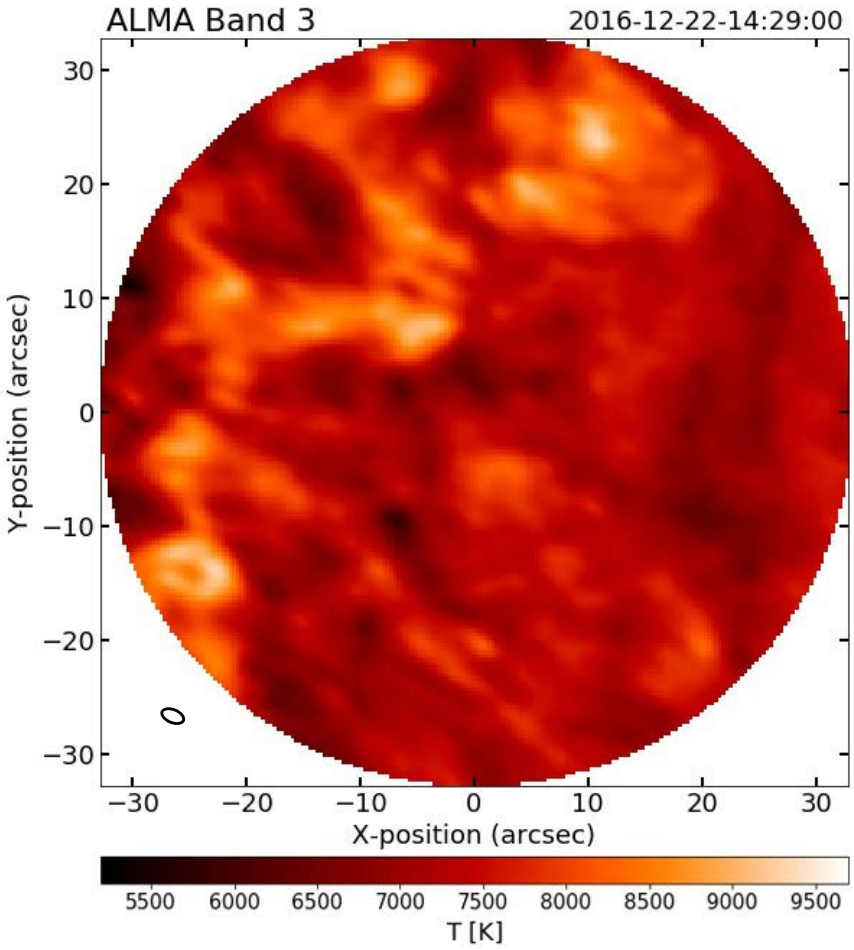

Figure 3.5: Illustration of resulting image from observational data at receiver band 3 ($\lambda \approx 3$ mm), reconstructed with the Solar ALMA pipeline. The data set has an integration time of 2 s for each frame and is the same as what is used in paper I and Wedemeyer, Szydlarski, et al. 2020. The resolution element, FWHM of the clean beam (main lobe of the PSF), is shown in the lower left corner.

Chapter 4

Numerical modelling

4.1 MHD-models

In order to understand the complex dynamical processes taking place in the solar atmosphere, numerical modelling provides an invaluable tool. Computational technology and resources have increased drastically during the recent years, which allows to perform increasingly heavier calculations. Numerical codes that produce state-of-the-art simulations of the solar atmosphere continue to reach new boundaries in terms of resolution and inclusion of relevant physics.

As a first step to estimate the observables at mm-wavelengths of the dynamic chromosphere, 1D models are constructed with the radiation-magnetohydrodynamical (MHD) code RADYN (Carlsson and Stein 2002; Carlsson and Stein 1992; Carlsson and Stein 1997). The RADYN code solves the equation of radiative transfer in non-LTE, the equations of conservation of mass, momentum and energy and the rate equations of atomic level populations on an adaptive mesh (Dorfi and Drury 1987) to allow resolving small-scale variations arising with propagating shock waves. The input model is set by a VAL atmosphere (Vernazza, Avrett, and Loeser 1981), with the addition of transition region and corona (Carlsson and Stein 2002). Waves are excited in the lower boundary of the model, with a broad span of initial amplitudes and periodicity. As the waves propagates upwardly, the steepen into shock waves.

As a result of the heavily dynamic nature of the chromosphere (see Section 1.2), which includes wave propagation in a non-isotropic 3D environment, a complex wave-pattern arises and the resulting profiles of the 3D shock wave signatures can differ significantly from that displayed in the 1D simulations (I). To properly estimate the observable signatures from dynamic small-scale structures, it is therefore concluded that we should resort to studying models in 3D. Therefore, in the current work, a 3D radiation-MHD model (Carlsson, Hansteen, et al. 2016) produced with the state-of-the-art code Bifrost (Gudiksen et al. 2011) is used in all papers (I, II and III).

The model that is used has the same setup as the publicly available *enhanced network* model[1], but is re-run with a higher cadence with output every 1 s instead of every 10 s. Snapshot number 400 ($t = 4000$ s) of the public version is used as initial input ($t = 0$ s) for the high cadence simulation. Though after that point, the two simulations are potentially diverging, which is necessary to be aware of when performing eventual comparisons. The model takes into account essential physical processes that have a large impact on the formation of mm-wavelength radiation, including non-LTE and non-equilibrium hydrogen ionisation.

[1] http://sdc.uio.no/search/simulations

An illustrative view of the simulation is displayed in Figure 4.1. The gas temperature is given on a logarithmic scale to accommodate for the large span in temperature between the different atmospheric layers. The temperature as a function of height is in general agreement with what is indicated in the 1D VAL model (Figure 1.1), although displaying a more complex structure, originating from the dynamic 3D structures. This model shows a relatively large span in magnetic field strength and topology, which seems to cover the parameter space that agrees well with typical conditions seen in observational quiet Sun data such as the resemblance to the magnetic field loops in Wedemeyer, Szydlarski, et al. 2020, global oscillatory behaviour reported by Jafarzadeh, Wedemeyer, Fleck, et al. 2021 and occurrence of small-scale brightening events in Eklund, Wedemeyer, Szydlarski, Jafarzadeh, and Guevara Gómez 2020 (paper I).

The simulation box spans 24 Mm with a total of 504 cells in each of the horizontal directions (x, y), thus with a constant horizontal grid spacing of 48 km. At the distance of 1 AU, this corresponds to approximately 0.066 arcsec, well below the resolution of currently offered solar ALMA observations (Section 3.2). The extent of the horizontal plane thus corresponds to approximately 33×33 arcsec, similar to the resulting FOV of ALMA observations at band 6 (Section 3.1.1). The horizontal boundary conditions are periodic. This makes it convenient in particular when degrading the resulting mm-maps to the angular resolution corresponding to ALMA observations, as the size of the FOV is preserved in the convolution by the 2D kernel (see Section 5.1; papers I and III), which allows looking in-depth at particular events also close to the boundaries. The simulation spans 17 Mm with 496 cells in the vertical direction (z; notice the start at negative values of -2.5 Mm in Figure 4.1, with $z = 0$ being aligned at the base of the photosphere where $\tau_{500} = 1.0$). The grid spacing in the vertical direction varies from 19 km in the bottom layer to 100 km in the top, with 20 km at chromospheric heights, which is the region of most focus in the current work.

The higher cadence of the simulation is necessary in order to track the evolution of dynamic small-scale phenomena. In particular, acoustic waves that steepen into shock waves are detected and studied. In the example of propagating shock waves, vertical velocities are commonly on the order of 10 km s^{-1}*. Such a wave front thus propagate about 5 grid cells between consequent snapshots with a cadence of 10 s of the publicly available model. With the cadence of 1 s, the temporal resolution does not set the limit. A larger vertical resolution would allow to more adequately track the upwardly propagating waves.

4.2 Radiative transfer modeling

The radiative transfer is calculated through the numerical MHD models in order to estimate the observables at mm- and sub-mm wavelengths. For the current work two different codes have been used for solving the equation of radiative transfer.

The Advanced Radiative Transfer (ART) code (de la Cruz Rodríguez,

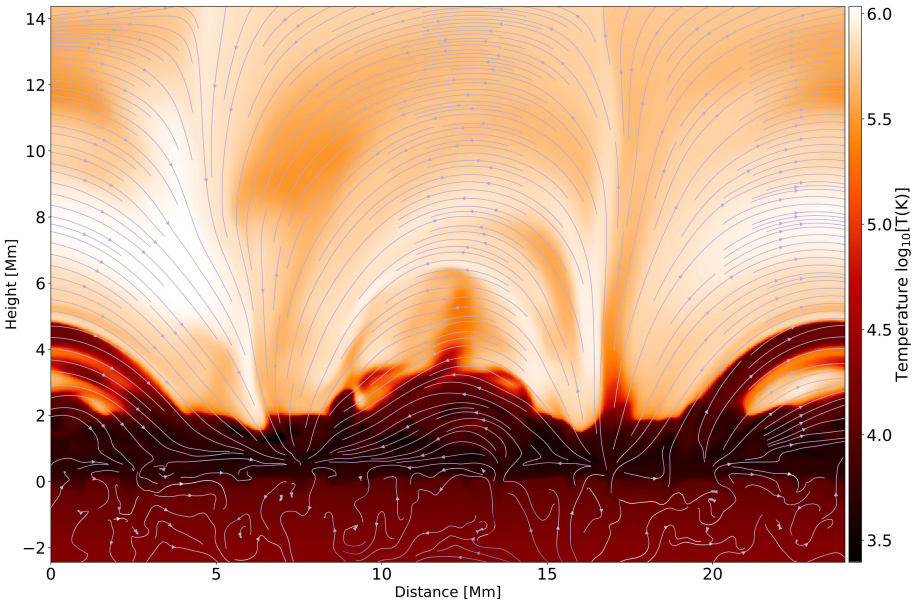

Figure 4.1: Illustrative view of a vertical slice through the Bifrost MHD model, with $y = 12$ Mm. The color-scale shows the logarithmic gas temperature and the magnetic field topology is shown by the overlaying blue arrows.

Szydlarski, and Wedemeyer 2021) is used for calculating the intensity of the continuum radiation. The output intensities are transformed to brightness temperatures using the Rayleigh-Jeans approximation as described above in Section 2.1. The calculations are monochromatic, performed for a specific frequency at a time. In order to facilitate the same bandwidth in the synthetic observables as in the observational data, the calculations are performed for three frequencies of each ALMA receiver sub-band (See Table 3.1). One sampling is done at the respective minimum and maximum frequencies and one in the centre of the sub-bands. The resulting brightness temperatures of the sub-bands are then represented by average values of the brightness temperatures over the three frequencies and the full-bands by averages over the ten frequency points (resulting in only ten and not twelve frequencies as the sub-bands comes in adjacent pairs and each pair thus shares one frequency point). Certainly, for larger accuracy, the calculations could be performed for more frequencies within the receiver bands. But as the calculations are only considering the continuum, the expectations would be that the gradient of the brightness temperatures within a sub-band are well approximated by a linear function. This is confirmed by the results and average values over the three frequencies respectively for each band is determined to be a valid approximation, which ultimately also allows for limiting the computational resources and memory usage. The code assumes formation of radiation in LTE, but considers relevant sources of opacity, such

as the electron densities in non-LTE, taken from the atmospheric model. Each vertical column of cells from the input model is calculated separately in 1D and put them together to a 2D map in the end. The final time-series of brightness temperature maps are used in the analysis of paper I, paper II and III.

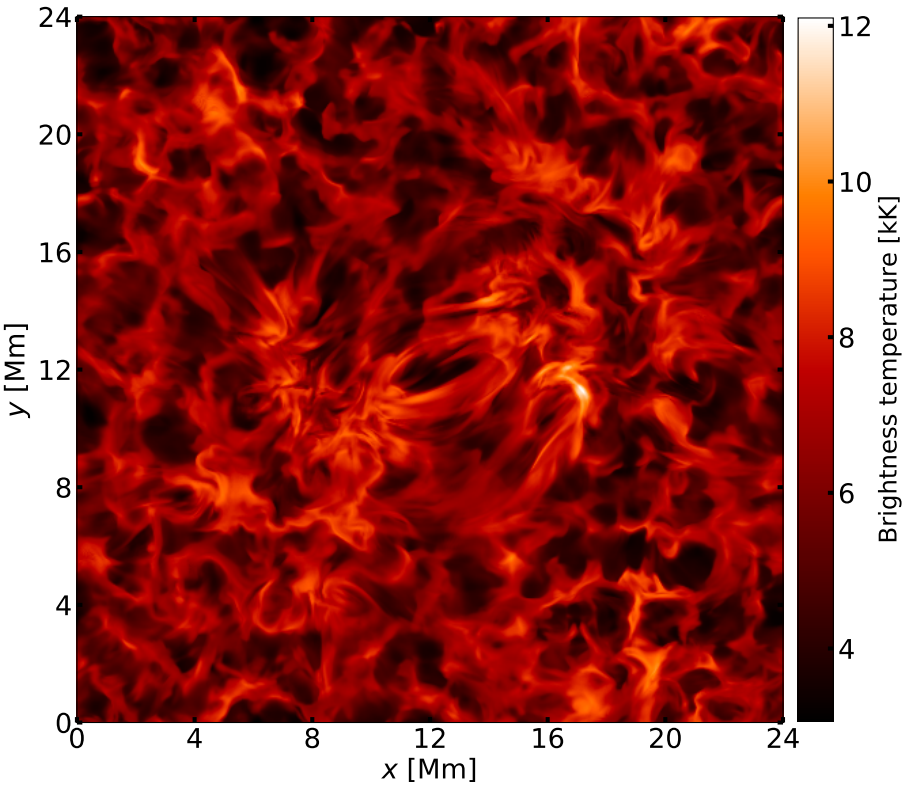

Figure 4.2: Synthetic observables at wavelengths corresponding to ALMA receiver band 6, over the entire FOV of the Bifrost model, calculated with the ART code. The brightness temperatures are averaged over the bandwidth of ALMA band 6 ($\lambda = 1.20 - 1.31$ mm).

The RH 1.5D code (Uitenbroek 2001; Pereira and Uitenbroek 2015) was also used for calculations of the radiative transfer in the current work. In particular, it was used for the 1D atmospheric RADYN models (Section 4.1), presented in paper I. The RH 1.5D code is a non-LTE radiative transfer solver, handling the non-equilibrium hydrogen ionization and the densities at the different atomic energy levels are taken care of. As implied by the name, RH 1.5D, works in a similar way as the ART code, in the sense that it calculates the radiative transfer plane-parallel in 1D at one column at a time. We need to stitch together the output afterwards, to create 2D maps. This process is referred to as 1.5D. The RH 1.5D code allows for more refined calculations in comparison to ART, for

instance with inclusion of spectral lines on-top of the continuum.

However, for the current work, the oscillator strength of the transition lines are set to zero and we focus on modelling of the brightness temperatures at the continuum level. The radiative transfer is calculated monochromatically at certain frequencies. For the extraction of the continuum temperatures corresponding to the receiver bands of ALMA, the calculations are conducted at equidistant frequencies across the bandwidth of the ALMA receiver sub-bands (Table 3.1). The results are then averaged to accommodate comparisons to ALMA observations, depending on the science case for anything between a single spectral channel of 15.6 MHz, a receiver sub-band of 2 GHz or the full-receiver band of $4 \times 2 = 8$ GHz.

Treating the radiative transfer in 1D, as done in both codes, results in a huge reduction of computational costs in comparison to performing radiative transfer calculations in full 3D and taking into account scattering of photons. In the case of synthetic observables at mm-wavelengths, this is a good approximation. As a result of the much lower density at chromospheric heights than in the photosphere (Figure 1.1) the mean-free path is much longer and scattering is not a major factor for the radiation of mm-wavelengths (Wedemeyer, Bastian, et al. 2016).

Comparisons of the outputs of the codes revealed only negligible differences. The resulting temporal profiles of the brightness temperature maps show the same features and would lead to the same conclusions of the results in the current studies.

Chapter 5

Analysis and results

In the papers included in this thesis, we make use of observational solar ALMA data, in receiver band 3 ($\lambda \approx 3$ mm; see Table 3.1) towards a quiet Sun area with a few network patches. A systematic search for detecting small-scale brightening events is conducted, where several hundred events (552) are detected and tracked in time, using the k-means statistical method (Everitt 1972; see details in paper I). Their properties are studied, such as their spatial size, apparent speed, lifetime and magnitude of brightness temperature excess (paper I). The characteristics and distribution of the events and the timing of recurrence go in line with what is expected of propagating shock waves in quiet Sun regions, based on numerical simulations (paper II). The brightness temperature excess of the events is lower than indicated by simulations of shock waves. The reason for this lies in the limited angular resolution of 1.4–2.1 arcsec (FWHM of the clean beam) of the observations. To establish the expected appearance of brightening events in observational quiet Sun data, brightening events are detected in the synthetic radiation maps at mm-wavelengths of the Bifrost model and compared to the corresponding signatures at degraded angular resolutions corresponding to observational data (paper III). The results of the simulations at degraded resolution agree well with what is seen in the observational data, which further validate the use of the Bifrost 3D model for these applications.

5.1 Synthetic observations

The Sun is very close compared to most other celestial objects and has an angular diameter of about 32 arcmin or 1920 arcsec, at the 1 AU distance, which is much larger than the effective FOV of the ALMA observations (see Eq. 3.1). In the solar atmosphere, there is consequently a combination of extended structures, filling the entire FOV and small-scale structures at scales down to and even below the resolution limit of the ALMA observations.

It is helpful to perform simulated observations in order to estimate to what degree a certain target or dynamic phenomenon is observable. Synthetic observations are performed with the *simalma*[1] task in CASA. This task allows to perform combined observations with the 12 m and 7 m arrays, where details such as the frequency range, antenna configuration and integration time can be specified. The synthetic measurements are calculated towards a model target, which here is the radiative mm-maps from the Bifrost model (Section 4.1). In paper III, we isolate and study how the angular resolution achievable with the different combinations of frequencies and ALMA array configurations affects the ability to observe the small-scale dynamics of the solar chromosphere.

[1] https://casaguides.nrao.edu/index.php/Simalma_(CASA_5.1)

In addition to this, the uncertainties that enter from antenna noise, atmospheric disturbances and the image reconstructing process could be included in the simulation process. The impact of this would be on-top of the limitations presented in paper III, and the magnitude of the uncertainties would be very dependent on the observational conditions and choice of reconstruction techniques. For establishing recommendations on optimal ways to reconstruct the interferometric data depending on the current conditions, a development study with the European Organisation for Astronomical Research in the Southern Hemisphere (ESO), *Advanced Study for Upgrades of the Atacama Large Millimeter/submillimeter Array (ALMA) – High-cadence Imaging of the Sun* is conducted, for which the results will be concluded in a final report in the end of 2021.

5.2 Beam filling factor

When studying small-scale structures, the beam filling factor becomes important. The beam filling factor is a measurement of the fraction of the main lobe of the PSF (the clean beam) that is 'filled' by the target. Comparisons of the distributions of mm-wavelength brightness temperatures at different spatial resolutions were previously studied by e.g., Wedemeyer-Böhm, Ludwig, et al. 2007 and Loukitcheva, Solanki, Carlsson, and White 2015 , who concluded that the distribution of the resulting brightness temperatures show a reduced range at reduced spatial resolution than what is seen at higher resolution. The resulting brightness temperature at a location is dependent on the surrounding structures and the size and shape of the resolution element. The simplest case is that of an isolated point source. The total intensity would be preserved, but distributed over the PSF. Thus, for small-scale structures in the chromosphere, the situation becomes more complex, as different features can be sampled simultaneously in the same PSF. In paper III (and paper I), the beam filling factor of the typical shapes and contrasts of the small-scale structures in the chromospheric quiet Sun is considered, for different combinations of antenna configurations and frequencies.

In general, locations with high temperature will appear less bright and points with low temperature will appear brighter, at lower spatial resolution. The most reliable temperatures are thus measured in the mid-ranges, close to the average value of the surrounding FOV. This becomes most important to consider in the vicinity of complicated structures with high brightness contrast.

5.3 Mapping the slope of the gas temperatures

As a consequence of the formation of the mm-wavelength radiation in LTE, the measured intensities show a linear relation to the plasma temperature and the opacity is wavelength dependent. The increasing opacity with wavelength is significant also within the receiver bands of ALMA. For instance, SB6.1 (sub-band 1 in receiver band 6; see Table 3.1), at $\lambda \approx 1.3$ mm becomes optically thick

at larger heights than SB6.4 at $\lambda \approx 1.2$ mm. This is the case at all locations in the Bifrost model, for all receiver bands offered for solar observations. It follows that the slope of the brightness temperature within a receiver band corresponds to the (local) plasma temperature gradient at the sampled layers.

An example of this is displayed in Eklund, Wedemeyer, Snow, et al. 2021 (paper II), which is reproduced here in Figure 5.1. This data is calculated with the ART code (see Section 4.2), and Figure 5.1 show a time-series of a single column (see Eklund, Wedemeyer, Snow, et al. 2021 for further specifics). For example, at $t = 120$ s in Figure 5.1d, the slope of the brightness temperature continuum at band 6 $\Delta T_{\mathrm{b}}^{B6}$ between the sub-bands SB6.1 and SB6.4,

$$\Delta T_{\mathrm{b}}^{B6} = T_{\mathrm{b}}^{\mathrm{SB6.1}} - T_{\mathrm{b}}^{\mathrm{SB6.4}}, \tag{5.1}$$

shows a negative value, indicating decreasing temperature with height, which agrees well with what is seen in the plot of the gas temperature, at the heights of where the radiation of band 6 is sampling ($z \approx 0.7$ Mm).

Figure 5.1 shows two major components in the contribution function of Band 3, around $t = 120$ s, one lower around $z \approx 1.0$ Mm and one upper around $z \approx 2.4$ Mm. The height of the upper component is well represented by the height where the contribution function integrated from the top have a cumulative sum of 0.2 times the total contribution (marked with dashed line in Figure 5.1b). At the heights of the upper component ($z \approx 2.4$ Mm), the gas temperature is much larger than at the heights of the lower component. The resulting brightness temperature is therefore significantly affected by the upper component in band 3. At $t = 120$ s, the equivalent slope of the brightness temperature continuum at band 3 $\Delta T_{\mathrm{b}}^{B3}$, shows positive values (Figure 5.1d), indicating an increasing temperature with increasing height, which is indicated in the gas temperature in Figure 5.1c, at the heights of the upper component of the contribution function. Further, the absolute magnitude of the sub-band difference in band 3 is larger than in band 6 (at the example of $t = 120$ s), indicating a steeper gradient in the gas temperature, as can be seen in Figure 5.1c.

Reconstructing the data for parts of the receiver band (e.g., for each sub-bands) and comparing the resulting continuum brightness temperatures could reveal information of variations of the gas temperature along the line-of-sight at the sampled layers. The sub-band differences thus provide further information in addition to the full-band average continuum temperature, that can increase our overall understanding of the complex dynamics of the chromosphere. Nonetheless, it remains to determine to what degree it is feasible to split up the measurements into sub-bands, while achieving a high signal-to-noise ratio.

5.4 Co-observations

Co-observations with other instruments provide complementary information to the acquired data and are very important in order to strengthen the interpretation of the observational data. In the current work, co-observations with the Solar Dynamics Observatory (SDO; Pesnell, Thompson, and Chamberlin 2012) were

used. The SDO telescope is a space-borne observatory launched in 2010, equipped with several instruments and is very useful because of its continuous observations of the whole solar disc at all times.

The Atmospheric Imaging Assembly (AIA; Lemen et al. 2012) observes in a number of wavelengths between 9.4 nm and 450 nm, at the cadence of 12 s and at a resolution of about 1 arcsec. The different wavelength filters map at different layers in the atmosphere. The 30.4 nm and 170 nm filters are in particular useful for cross-correlation with the ALMA data for co-alignment (see e.g., Wedemeyer, Szydlarski, et al. 2020).

The Helioseismic and Magnetic Imager (HMI; Schou et al. 2012) provides line-of-sight magnetograms of the photosphere calculated from the Zeeman line-shifts of the Fe I line at 6173 Å. Even though being measured at photospheric heights, the line-of-sight magnetograms provide invaluable information in the analysis of the ALMA data. The magnetic field lines extending from the photospheric footpoints to chromospheric heights can have significant inclination and extend over large distances. Depending on the local atmospheric conditions and the height of formation of the ALMA continuum at a particular wavelength, there can even be largely horizontal magnetic field lines, overlying an area with seemingly low magnetic field strength as indicated by the photospheric magnetograms. Nonetheless, initial results show that there is a correlation between the ALMA brightness temperatures and the line-of-sight magnetograms. The latter thus gives at the very least a first approximation, despite the differences in formation height. Refined techniques with extrapolation of the magnetic field lines from photospheric to chromospheric heights have been performed (Wiegelmann 2004; Wiegelmann et al. 2005; Zhu, Wiegelmann, and Solanki 2020; Zhu and Wiegelmann 2018), which have been used to study the influence of the chromospheric magnetic field lines on the ALMA data (Jafarzadeh, Wedemeyer, Fleck, et al. 2021).

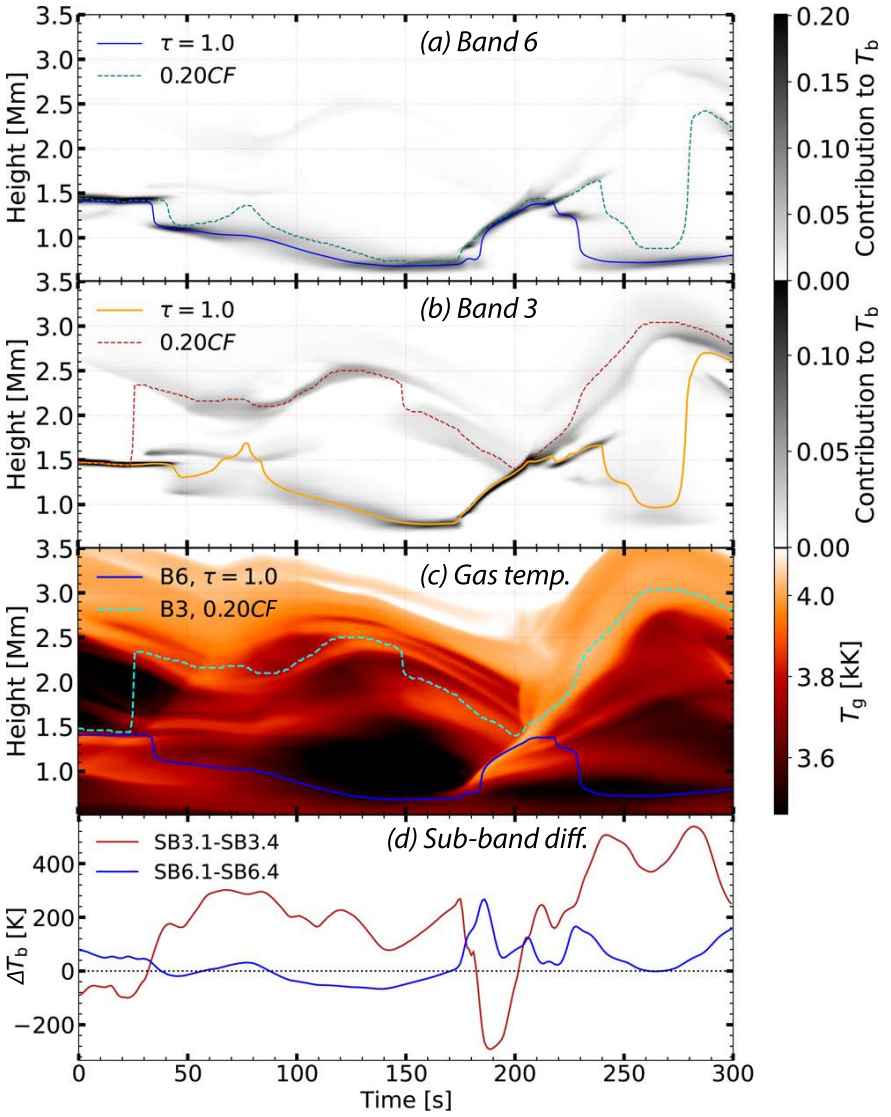

Figure 5.1: Time evolution at a single column in the Bifrost model, (same position as in Figure 4 in paper II; Eklund, Wedemeyer, Snow, et al. 2021). (a) Contribution function with height for band 6. The height of optical depth unity is marked by the solid blue line and a fraction of 0.2 times the contribution function integrated from above with a dashed line. (b) Contribution function with height for band 3. The height of optical depth unity is marked by the solid orange line and a fraction of 0.2 times the contribution function integrated from above with a dashed line. (c) Gas temperature as a function of height, with the respective effective formation height for the dominating component of ALMA band 3 (0.2×CF) and band 6 ($\tau = 1.0$). (d) The brightness temperature differences between the outermost sub-bands of bands 3 and 6 (SB3.1-SB3.4 and SB6.1-SB6.4).

Chapter 6

Contextual description and summary of papers

Paper I The first paper in this thesis takes part in the paper series *The Sun at millimeter wavelengths*, which aims towards collecting the initial results from the solar ALMA group in Oslo. This paper, *Small-scale dynamic events in ALMA Band 3*, is the second in the series. The scope was to establish for the first time the detection of small-scale dynamic events in solar ALMA data, in particular from a statistical approach instead of only a single or a handful of examples. At the time when this paper was initiated, it still remained unclear to what degree small-scale structures could be detected in the solar ALMA data, specifically in terms of the temporal evolution of such features. This work is based on a dataset that is one of the first to be successfully reconstructed resulting in high cadence time series, stable enough to track dynamic features in time. The observational target is a quiet Sun region with network patches and overlying magnetic field lines originating from nearby locations. Several hundred (552) dynamic events, showing a significant enhancement in brightness temperature ($\Delta T_\mathrm{b} > 400$ K) were detected and tracked through time using a statistical approach. The limit of 400 K was established to be on the conservative side in regards to noise in the data. The physical properties of all the events were studied, such as their angular size, magnitude of brightening enhancement, lifetime, apparent speed and the influence by line-of-sight magnetic field strength. It is, with the aid of numerical simulations, shown that a majority of the detected events are probably the observational signatures of propagating shock waves at millimetre wavelengths. In conclusion, this paper shows novel results pointing towards the great capabilities to observe chromospheric small-scale dynamics with ALMA.

Paper II The second paper presented in this thesis focuses on detecting shock waves in the 3D numerical models of the solar atmosphere and on characterising the observable shock wave signatures at millimetre wavelengths (corresponding to the range covered by ALMA band 6; $\lambda = 1.2 - 1.3$ mm; see Table 3.1). The time-evolution of the local MHD-parameters, gas temperature, vertical velocity and electron density of the atmospheric model is studied. It is shown that there is an excess in brightness temperature of several thousand degrees in connection to a propagating shock wave. Further, it is shown that the difference in brightness temperature between the receiver sub-bands can be utilized to

extract further information of the local conditions in the sampled layers of the atmosphere. This study serves as an initial step towards deploying a statistical approach detecting many shock waves and correlating their individual variations of the observable mm-wavelength signatures with the local MHD-conditions. The approach could be applied to ALMA observations in order to determine the (approximate) physical conditions in the chromosphere during the passage of shock waves, as discussed in paper I, contributing to a better understanding of the transport of energy in the solar atmosphere.

Paper III The focus of the third paper is the effect of spatial resolution on solar ALMA observations. In particular, when observing the small-scale dynamics such as brightening events in connection to, for instance, propagating shock fronts, the resulting brightness temperature excess is heavily dependent on the angular resolution. Radiative transfer calculations at millimetre wavelengths are performed on the state-of-the-art Bifrost 3D model (Section 4.1). The resulting brightness temperature maps are degraded to the angular resolutions corresponding to observations with ALMA in different array configurations (C3–C7) and at different receiver bands (3–10). The configurations and receiver bands that are considered also cover cases that are currently not (yet) offered for solar observations, in order to provide estimations on observations with future capabilities. The study is concentrated to three different regions in the FOV of the model, displaying characteristically different magnetic field topology. The distributions of the brightness temperatures at different receiver bands and at the different angular resolutions are presented for each region. In addition the average formation heights are provided, showing the correlation with the magnetic field topology. The amplitude of the signatures of brightening events detected at original resolution of the numerical model are compared to the corresponding signatures at degraded resolution. The resulting signatures at degraded resolution in the different characteristic regions agree well with what is seen in the observational data (presented in paper I).

Bibliography

Avrett, E. H. (Jan. 2003). "The Solar Temperature Minimum and Chromosphere". In: *Current Theoretical Models and Future High Resolution Solar Observations: Preparing for ATST*. Ed. by Pevtsov, A. A. and Uitenbroek, H. Vol. 286. Astronomical Society of the Pacific Conference Series, p. 419.

Berger, P. S. and Simon, M. (Feb. 1972). "Solar Radio Recombination Lines". In: *The Astrophysical Journal* vol. 171, p. 191.

Bogdan, T. J. et al. (Dec. 2003). "Waves in the Magnetized Solar Atmosphere. II. Waves from Localized Sources in Magnetic Flux Concentrations". In: *The Astrophysical Journal* vol. 599, no. 1, pp. 626–660.

Braatz, J. et al. (Jan. 2021). "ALMA Cycle 8 2021 Proposer's Guide". In: *ALMA Doc.* vol. 8.2, no. v1.0.

Carlsson, M., De Pontieu, B., and Hansteen, V. H. (Aug. 2019). "New View of the Solar Chromosphere". In: vol. 57, pp. 189–226.

Carlsson, M., Hansteen, V. H., et al. (Jan. 2016). "A publicly available simulation of an enhanced network region of the Sun". In: *Astronomy & Astrophysics* vol. 585, A4, A4. arXiv: 1510.07581 [astro-ph.SR].

Carlsson, M. and Stein, R. F. (June 2002). "Dynamic Hydrogen Ionization". In: *The Astrophysical Journal* vol. 572, no. 1, pp. 626–635. arXiv: astro-ph/0202313 [astro-ph].

Carlsson, M. and Stein, R. F. (Sept. 1992). "Non-LTE Radiating Acoustic Shocks and CA II K2V Bright Points". In: *The Astrophysical Journal Letters* vol. 397, p. L59.

— (May 1997). "Formation of Solar Calcium H and K Bright Grains". In: *The Astrophysical Journal* vol. 481, no. 1, pp. 500–514.

Chintzoglou, G. et al. (Jan. 2021a). "ALMA and IRIS Observations of the Solar Chromosphere. I. An On-disk Type II Spicule". In: *The Astrophysical Journal* vol. 906, no. 2, 82, p. 82. arXiv: 2005.12717 [astro-ph.SR].

— (Jan. 2021b). "ALMA and IRIS Observations of the Solar Chromosphere. II. Structure and Dynamics of Chromospheric Plages". In: *The Astrophysical Journal* vol. 906, no. 2, 83, p. 83. arXiv: 2012.05970 [astro-ph.SR].

Clark, T. A., Naylor, D. A., and Davis, G. R. (May 2000a). "Detection and limb brightening of the H bt I n=20-19 Rydberg line in the submillimetre spectrum of the Sun". In: *Astronomy & Astrophysics* vol. 357, pp. 757–762.

Clark, T. A., Naylor, D. A., and Davis, G. R. (Sept. 2000b). “Detection of the H I n=22-21 Rydberg line in emission at the solar submillimetre limb”. In: *Astronomy & Astrophysics* vol. 361, pp. L60–L62.

Cornwell, T. J. (Nov. 2008). “Multiscale CLEAN Deconvolution of Radio Synthesis Images”. In: *IEEE Journal of Selected Topics in Signal Processing* vol. 2, no. 5, pp. 793–801.

Cornwell, T. J. and Evans, K. F. (Feb. 1985). “A simple maximum entropy deconvolution algorithm”. In: *Astronomy & Astrophysics* vol. 143, no. 1, pp. 77–83.

da Silva Santos, J. M. et al. (Feb. 2020). “The multi-thermal chromosphere. Inversions of ALMA and IRIS data”. In: *Astronomy & Astrophysics* vol. 634, A56, A56. arXiv: 1912.09886 [astro-ph.SR].

de la Cruz Rodríguez, J., Szydlarski, M., and Wedemeyer, S. (Mar. 2021). *ART: Advanced (and fast!) Radiative Transfer code for Solar Physics*. Version v1.1.

de la Cruz Rodrıguez, J. and van Noort, M. (Sept. 2017). “Radiative Diagnostics in the Solar Photosphere and Chromosphere”. In: vol. 210, no. 1-4, pp. 109–143. arXiv: 1609.08324 [astro-ph.SR].

Dorfi, E. A. and Drury, L. O. (Mar. 1987). “Simple adaptive grids for 1-D initial value problems.” In: *Journal of Computational Physics* vol. 69, pp. 175–195.

Eklund, H., Wedemeyer, S., Snow, B., et al. (Feb. 2021). “Characterization of shock wave signatures at millimetre wavelengths from Bifrost simulations”. In: *Philosophical Transactions of the Royal Society of London Series A* vol. 379, no. 2190, 20200185, p. 20200185. arXiv: 2008.05324 [astro-ph.SR].

Eklund, H., Wedemeyer, S., Szydlarski, M., and Jafarzadeh, S. (June 2021). “The Sun at millimeter wavelengths. III. Impact of the spatial resolutionon solar ALMA observations”. In: *Astronomy & Astrophysics*.

Eklund, H., Wedemeyer, S., Szydlarski, M., Jafarzadeh, S., and Guevara Gómez, J. C. (Dec. 2020). “The Sun at millimeter wavelengths. II. Small-scale dynamic events in ALMA Band 3”. In: *Astronomy & Astrophysics* vol. 644, A152, A152. arXiv: 2010.06400 [astro-ph.SR].

Everitt, B. (1972). “Cluster Analysis: A Brief Discussion of Some of the Problems.” In: *British Journal of Psychiatry* vol. 120(555), pp. 143–145.

Fontenla, J. M., Avrett, E. H., and Loeser, R. (Mar. 1993). “Energy Balance in the Solar Transition Region. III. Helium Emission in Hydrostatic, Constant-Abundance Models with Diffusion”. In: *The Astrophysical Journal* vol. 406, p. 319.

Galloway, D. J. and Weiss, N. O. (Feb. 1981). “Convection and magnetic fields in stars”. In: *The Astrophysical Journal* vol. 243, pp. 945–953.

Gudiksen, B. V. et al. (July 2011). "The stellar atmosphere simulation code Bifrost. Code description and validation". In: *Astronomy & Astrophysics* vol. 531, A154, A154. arXiv: 1105.6306 [astro-ph.SR].

Guevara Gómez, J. C. et al. (Feb. 2021). "High-frequency oscillations in small chromospheric bright features observed with Atacama Large Millimetre/Submillimetre Array". In: *Philosophical Transactions of the Royal Society of London Series A* vol. 379, no. 2190, 20200184, p. 20200184. arXiv: 2008.04179 [astro-ph.SR].

Hasan, S. S., Steiner, O., and van Ballegooijen, A. (May 2008). "Inferring the chromospheric magnetic topology through waves". In: *Waves & Oscillations in the Solar Atmosphere: Heating and Magneto-Seismology*. Ed. by Erdélyi, R. and Mendoza-Briceno, C. A. Vol. 247, pp. 78–81.

Hoang-Binh, D. et al. (July 1987). "Ion-collision broadening of solar lines in the far-infrared and submillimeter spectrum". In: *Astronomy & Astrophysics* vol. 181, no. 1, pp. 134–137.

Hubeny, I. and Mihalas, D. (2014). *Theory of Stellar Atmospheres*.

Hyde Wollaston, W. (Jan. 1802). "A Method of Examining Refractive and Dispersive Powers, by Prismatic Reflection". In: *Philosophical Transactions of the Royal Society of London Series I* vol. 92, pp. 365–380.

Högbom, J. A. (June 1974). "Aperture Synthesis with a Non-Regular Distribution of Interferometer Baselines". In: vol. 15, p. 417.

Iguchi, S. et al. (Feb. 2009). "The Atacama Compact Array (ACA)". In: *Publications of the Astronomical Society of Japan* vol. 61, no. 1, pp. 1–12.

Jafarzadeh, S., Wedemeyer, S., Fleck, B., et al. (Feb. 2021). "An overall view of temperature oscillations in the solar chromosphere with ALMA". In: *Philosophical Transactions of the Royal Society of London Series A* vol. 379, no. 2190, 20200174, p. 20200174. arXiv: 2010.01918 [astro-ph.SR].

Jafarzadeh, S., Wedemeyer, S., Szydlarski, M., et al. (Feb. 2019). "The solar chromosphere at millimetre and ultraviolet wavelengths. I. Radiation temperatures and a detailed comparison". In: *Astronomy & Astrophysics* vol. 622, A150, A150. arXiv: 1901.05763 [astro-ph.SR].

Khersonskii, V. K. and Varshalovich, D. A. (June 1980). "The Possibility of Observing Recombination Lines in Solar Radiation". In: *Sov. Astron. AJ (Engl. Transl.);(United States)* vol. 24, p. 359.

Lemen, J. R. et al. (Jan. 2012). "The Atmospheric Imaging Assembly (AIA) on the Solar Dynamics Observatory (SDO)". In: vol. 275, no. 1-2, pp. 17–40.

Loukitcheva, M., Solanki, S. K., Carlsson, M., and Stein, R. F. (May 2004). "Millimeter observations and chromospheric dynamics". In: *Astronomy & Astrophysics* vol. 419, pp. 747–756.

Loukitcheva, M., Solanki, S. K., Carlsson, M., and White, S. M. (Mar. 2015). "Millimeter radiation from a 3D model of the solar atmosphere. I. Diagnosing chromospheric thermal structure". In: *Astronomy & Astrophysics* vol. 575, A15, A15. arXiv: 1501.02898 [astro-ph.SR].

Marti-Vidal, I. (June 2017). "APSYNSIM: An Interactive Tool To Learn Interferometry". In: *arXiv e-prints*, arXiv:1706.00936, arXiv:1706.00936. arXiv: 1706.00936 [astro-ph.IM].

Martınez-Sykora, J. et al. (Mar. 2020). "The Formation Height of Millimeter-wavelength Emission in the Solar Chromosphere". In: *The Astrophysical Journal Letters* vol. 891, no. 1, L8, p. L8. arXiv: 2001.10645 [astro-ph.SR].

Mitalas, R. and Sills, K. (1992). "On the photon diffusion time scale for the sun". In: *The Astrophysical Journal* vol. 401, p. 759.

Molnar, M. E. et al. (Aug. 2019). "Solar Chromospheric Temperature Diagnostics: A Joint ALMA-Hα Analysis". In: *The Astrophysical Journal* vol. 881, no. 2, 99, p. 99. arXiv: 1906.08896 [astro-ph.SR].

Nindos, A., Alissandrakis, C. E., et al. (June 2020). "Transient brightenings in the quiet Sun detected by ALMA at 3 mm". In: *Astronomy & Astrophysics* vol. 638, A62, A62. arXiv: 2004.07591 [astro-ph.SR].

Nindos, A., Patsourakos, S., et al. (June 2021). "ALMA observations of the variability of the quiet Sun at millimeter wavelengths". In: *arXiv e-prints*, arXiv:2106.04220, arXiv:2106.04220. arXiv: 2106.04220 [astro-ph.SR].

Patsourakos, S. et al. (Feb. 2020). "Observations of solar chromospheric oscillations at 3 mm with ALMA". In: *Astronomy & Astrophysics* vol. 634, A86, A86. arXiv: 1912.03480 [astro-ph.SR].

Pesnell, W. D., Thompson, B. J., and Chamberlin, P. C. (Jan. 2012). "The Solar Dynamics Observatory (SDO)". In: vol. 275, no. 1-2, pp. 3–15.

Remijan, A. et al. (2020). "ALMA Technical Handbook". In: *ALMA Doc. 8.3, ver. 1.0* vol. 8.3.

Rieutord, M. and Rincon, F. (Dec. 2010). "The Sun's Supergranulation". In: *Living Reviews in Solar Physics* vol. 7, no. 1, 2, p. 2. arXiv: 1005.5376 [astro-ph.SR].

Rodger, A. S. et al. (Apr. 2019). "First Spectral Analysis of a Solar Plasma Eruption Using ALMA". In: *The Astrophysical Journal* vol. 875, no. 2, 163, p. 163. arXiv: 1902.01319 [astro-ph.SR].

Rosenthal, C. S. et al. (Jan. 2002). "Waves in the Magnetized Solar Atmosphere. I. Basic Processes and Internetwork Oscillations". In: *The Astrophysical Journal* vol. 564, no. 1, pp. 508–524.

Schmidt, W. et al. (Nov. 2012). "The 1.5 meter solar telescope GREGOR". In: *Astronomische Nachrichten* vol. 333, no. 9, p. 796.

Schou, J. et al. (Jan. 2012). “Design and Ground Calibration of the Helioseismic and Magnetic Imager (HMI) Instrument on the Solar Dynamics Observatory (SDO)”. In: vol. 275, no. 1-2, pp. 229–259.

Shimabukuro, F. I. and Wilson, W. J. (Aug. 1973). “Search for Solar Recombination Lines in the Frequency Range 11 0-1 15 GHZ”. In: *The Astrophysical Journal* vol. 183, pp. 1025–1028.

Shimojo, M., Hudson, H. S., et al. (May 2017). “The First ALMA Observation of a Solar Plasmoid Ejection from an X-Ray Bright Point”. In: *The Astrophysical Journal Letters* vol. 841, no. 1, L5, p. L5. arXiv: 1704.04881 [astro-ph.SR].

Shimojo, M., Kawate, T., et al. (Jan. 2020). “Estimating the Temperature and Density of a Spicule from 100 GHz Data Obtained with ALMA”. In: *The Astrophysical Journal Letters* vol. 888, no. 2, L28, p. L28. arXiv: 1912.05714 [astro-ph.SR].

Spiegel, E. A. and Zahn, J. .-P. (Nov. 1992). “The solar tachocline.” In: *Astronomy & Astrophysics* vol. 265, pp. 106–114.

Steiner, O. et al. (June 2008). “The Horizontal Internetwork Magnetic Field: Numerical Simulations in Comparison to Observations with Hinode”. In: *The Astrophysical Journal Letters* vol. 680, no. 1, p. L85. arXiv: 0801.4915 [astro-ph].

Vernazza, J. E., Avrett, E. H., and Loeser, R. (Apr. 1981). “Structure of the solar chromosphere. III. Models of the EUV brightness components of the quiet sun.” In: *The Astrophysical Journal Supplement Series* vol. 45, pp. 635–725.

Wedemeyer, S., Bastian, T., et al. (Apr. 2016). “Solar Science with the Atacama Large Millimeter/Submillimeter Array—A New View of Our Sun”. In: *Space Science Reviews* vol. 200, no. 1-4, pp. 1–73. arXiv: 1504.06887 [astro-ph.SR].

Wedemeyer, S., Szydlarski, M., et al. (Mar. 2020). “The Sun at millimeter wavelengths. I. Introduction to ALMA Band 3 observations”. In: *Astronomy & Astrophysics* vol. 635, A71, A71. arXiv: 2001.02185 [astro-ph.SR].

Wedemeyer-Böhm, S., Lagg, A., and Nordlund, Å. (Apr. 2009). “Coupling from the Photosphere to the Chromosphere and the Corona”. In: *Space Science Reviews* vol. 144, no. 1-4, pp. 317–350. arXiv: 0809.0987 [astro-ph].

Wedemeyer-Böhm, S., Ludwig, H. G., et al. (Sept. 2007). “Inter-network regions of the Sun at millimetre wavelengths”. In: *Astronomy & Astrophysics* vol. 471, no. 3, pp. 977–991. arXiv: 0705.2304 [astro-ph].

Wiegelmann, T. (Jan. 2004). “Optimization code with weighting function for the reconstruction of coronal magnetic fields”. In: *The solar dynamics observatory* vol. 219, no. 1, pp. 87–108. arXiv: 0802.0124 [astro-ph].

Wiegelmann, T. et al. (Apr. 2005). “Comparing magnetic field extrapolations with measurements of magnetic loops”. In: *Astronomy & Astrophysics* vol. 433, no. 2, pp. 701–705. arXiv: 0801.4519 [astro-ph].

Zhu, X., Wiegelmann, T., and Solanki, S. K. (Aug. 2020). “Magnetohydrostatic modeling of AR11768 based on a SUNRISE/IMaX vector magnetogram”. In: *Astronomy & Astrophysics* vol. 640, A103, A103. arXiv: 2005.14332 [astro-ph.SR].

Zhu, X. and Wiegelmann, T. (Oct. 2018). “On the Extrapolation of Magnetohydrostatic Equilibria on the Sun”. In: *The Astrophysical Journal* vol. 866, no. 2, 130, p. 130. arXiv: 1809.02168 [astro-ph.SR].

Papers

Paper I

The Sun at millimeter wavelengths II. Small-scale dynamic events in ALMA Band 3

Henrik Eklund, Sven Wedemeyer, Mikolaj Szydłarski, Shahin Jafarzadeh, Juan Camilo Guevara Gómez

Published in *Astronomy & Astrophysics*, December 2020, volume 644, issue A152, DOI: 10.1051/0004-6361/202038250.

A&A 644, A152 (2020)
https://doi.org/10.1051/0004-6361/202038250

Astronomy & Astrophysics

The Sun at millimeter wavelengths

II. Small-scale dynamic events in ALMA Band 3

Henrik Eklund[1,2], Sven Wedemeyer[1,2], Mikolaj Szydlarski[1,2], Shahin Jafarzadeh[1,2], and Juan Camilo Guevara Gómez[1,2]

[1] Rosseland Centre for Solar Physics, University of Oslo, Postboks 1029 Blindern, 0315 Oslo, Norway
e-mail: henrik.eklund@astro.uio.no
[2] Institute of Theoretical Astrophysics, University of Oslo, Postboks 1029 Blindern, 0315 Oslo, Norway

Received 23 April 2020 / Accepted 9 October 2020

ABSTRACT

Context. Solar observations with the Atacama Large Millimeter/sub-millimeter Array (ALMA) facilitate studies of the atmosphere of the Sun at chromospheric heights at high spatial and temporal resolution at millimeter wavelengths.
Aims. ALMA intensity data at millimeter(mm)-wavelengths are used for a first detailed systematic assessment of the occurrence and properties of small-scale dynamical features in the quiet Sun.
Methods. We analyzed ALMA Band 3 data (∼3 mm/100 GHz) with a spatial resolution of ∼1.4–2.1 arcsec and a duration of ∼40 min together with SDO/HMI magnetograms. The temporal evolution of the mm maps is studied to detect pronounced dynamical features, which then are connected to dynamical events via a *k*-means clustering algorithm. We studied the physical properties of the resulting events and explored whether or not they show properties consistent with propagating shock waves. For this purpose, we calculated observable shock wave signatures at mm wavelengths from one- and three-dimensional model atmospheres.
Results. We detect 552 dynamical events with an excess in brightness temperature (ΔT_b) of at least ≥400 K. The events show a large variety in size up to ∼9″, amplitude ΔT_b up to ∼1200 K with typical values in the range ∼450–750 K, and lifetime at full width at half maximum of ΔT_b of between ∼43 and 360 s, with typical values between ∼55 and 125 s. Furthermore, many of the events show signature properties suggesting that they are likely produced by propagating shock waves.
Conclusions. There are a lot of small-scale dynamic structures detected in the Band 3 data, even though the spatial resolution sets limitations on the size of events that can be detected. The number of dynamic signatures in the ALMA mm data is very low in areas with photospheric footpoints with stronger magnetic fields, which is consistent with the expectation for propagating shock waves.

Key words. Sun: chromosphere – Sun: radio radiation – Sun: atmosphere – Sun: magnetic fields – shock waves – techniques: interferometric

1. Introduction

The Atacama Large Millimeter/sub-millimeter Array (ALMA) provides new diagnostic possibilities for studying the dynamical nature of the solar chromosphere at millimeter (mm) wavelengths thanks to its high spatial and temporal resolution. The mm-wavelength radiation observable with ALMA originates at chromospheric heights (Wedemeyer et al. 2016, and references therein) from free-free continua emission under conditions of local thermodynamic equilibrium (LTE). The measured continuum intensities (and equivalently the continuum brightness temperatures) are therefore expected to depend linearly on the local thermal gas temperature, or more precisely, the electron temperature.

The solar chromosphere is a highly dynamic and structured region of the Sun's atmosphere that features a variety of phenomena on different spatial scales. In particular, small-scale structures have been shown to evolve often on short timescales on the order of a few seconds or less (Okamoto & De Pontieu 2011; Morton 2012; Gafeira et al. 2017; Jafarzadeh et al. 2017a,b). Therefore, both high spatial and temporal resolution are needed to fully understand this dynamic region. It is also worth nothing that most of the commonly employed chromospheric diagnostics (at ultraviolet, optical, and infrared wavelengths) are formed under non-LTE conditions (de la Cruz Rodríguez & van Noort 2017; Carlsson et al. 2019), which as a result, renders the meaningful interpretation of such observations challenging. Thus, by promising to provide direct measurements of temperatures under LTE conditions at high temporal resolution, ALMA is an excellent tool for studying dynamic small-scale structures in the solar chromosphere (see, e.g., Guevara Gómez et al. 2020).

Observations of the quiet-Sun internetwork chromosphere in the Ca II K line revealed a bright mesh-like pattern of elongated structures with fainter intermediate areas outside strong magnetic field concentrations (Wöger et al. 2006). The typical mesh size of the observed pattern, which is produced by the interaction of propagating shock waves, was determined to be on the order of 1″.95. Numerical simulations of the solar atmosphere predict that a corresponding pattern should be observable with ALMA (Wedemeyer-Böhm et al. 2007; Loukitcheva et al. 2015; Wedemeyer et al. 2016, and references therein).

The corresponding shock wave signatures at mm wavelengths as observable with ALMA have been predicted by Loukitcheva et al. (2004, 2006) using one-dimensional models and by Eklund et al. (2020) using a three-dimensional model (cf. Wedemeyer-Böhm et al. 2007). These latter authors found large brightness temperature variations with amplitudes of thousands of Kelvin. Studies of observational ALMA data on the other hand indicate smaller temperature variations on the order of several hundred Kelvin (see, e.g. Patsourakos et al. 2020;

Nindos et al. 2018; Alissandrakis et al. 2017; Wedemeyer et al. 2020; Loukitcheva et al. 2019).

We note that the spatial resolution of available ALMA band 3 data used in publications is around 2″ or below (e.g., Loukitcheva et al. 2019) with the minor beam axis down to 1.4″ (see Wedemeyer et al. 2020, and references therein) and is therefore on the same order as the aforementioned typical spatial scale of the shock-wave-induced mesh-like pattern. The visibility of this pattern and with it the amplitude of observed brightness temperature variations therefore critically depend on the angular resolution achieved with ALMA. At the same time, ALMA provides a very useful tool to study and understand shock waves and the general dynamics of the chromosphere given that the measured brightness temperatures are expected to be closely related to the local electron temperature in the probed layer (Wedemeyer et al. 2016, and references therein). Accurate statistics of the spatial and temporal scales as well as the amplitudes of the brightness temperature variations can also be used as feedback to numerical models of the solar atmosphere in order to refine simulations, making them even more accurate and realistic.

Here, we analyze one of the first regular Band 3 (~3 mm/100 GHz) observations of the Sun with ALMA (Cycle 4), which has been described in Wedemeyer et al. (2020). This high cadence (2 s) time series is used for a statistical study of detected brightness temperature signatures of small-scale dynamic events. An important question in this regard pertains to whether or not the detected signatures are caused by propagating shock waves in the solar chromosphere. This paper is structured in the following way: in Sect. 2, the properties and the processing of the observational data are described. In Sect. 3, the statistics of the detected dynamical features are presented. In Sect. 4 we further discuss the results and, with the support of numerical simulations, investigate the possibility that the detected events are signatures of propagating shock waves. In that respect, the limitations of the observational data are addressed. In Sect. 5, we summarize and conclude the results and offer a brief outlook on future work.

2. Methods

2.1. Observational data

The observational data studied in this paper were obtained with ALMA in receiver band 3 on December 22, 2016 (project ID: 2016.1.00423.S), targeting a quiet Sun region with a few magnetic network elements close to solar disk center. Observations were made between 14:19 UT and 15:07 UT separated into four time scans in blocks of 10 min each, separated by calibration gaps of ~2.5 min. The data set was processed using the Solar Alma Pipeline (SoAP). The specifics of SoAP will be explained in detail in a forthcoming paper (Szydlarski et al., in prep., see also Wedemeyer et al. 2020). In summary, the data set was calibrated (with a script delivered together with the data from the ALMA Science Archive) followed by deconvolution using the Multiscale CLEAN algorithm (Cornwell 2008) and primary beam correction, which results in interferometric intensity maps. These are combined ("feathered") with single-dish total power measurements. The intensities were transformed into brightness temperatures under the assumption of the Rayleigh-Jeans law and formation in LTE (see, e.g., Wilson et al. 2013) through the relation

$$T_\mathrm{b} = \frac{c^2 I_\nu}{2 k_\mathrm{B} \nu^2}, \tag{1}$$

Table 1. Span of wavelength and frequency of the sub-bands of ALMA spectral band 3.

	Band 3					
	Wavelength [mm]			Frequency [GHz]		
Sub-band	Min	Mid	Max	Min	Mid	Max
SB1	3.189	3.224	3.259	92.0	93.0	94.0
SB2	3.123	3.156	3.189	94.0	95.0	96.0
SB3	2.828	2.856	2.883	104.0	105.0	106.0
SB4	2.776	2.802	2.828	106.0	107.0	108.0

where c is the speed of light and k_B is the Boltzmann constant. The images were then combined into a time series. The final dataset has a cadence of 2 s, with a total of 1200 time-steps. For an in-depth analysis and details on this specific dataset, see Wedemeyer et al. (2020), where the quality and limitations of the data are evaluated. The same dataset is analyzed in Jafarzadeh et al. (2020), where global oscillations in the time-series of images (along with other ALMA datasets) are studied.

For solar observations, ALMA receiver band 3 is currently set up with four spectral sub-bands as indicated in Table 1. The formation height of the mm-wavelength radiation is wavelength dependent. ALMA band 3 is thought to be formed in the upper chromosphere (Wedemeyer et al. 2020; White et al. 2017, and references therein). The sub-bands are grouped pairwise where SB1 is adjacent to SB2, and SB3 is adjacent to SB4. Differences between the sub-bands can in principle be used to study the small-scale structure along the line of sight (see e.g., Jafarzadeh et al. 2019; Rodger et al. 2019) although simulations imply that the differences are typically small (see, e.g., Eklund et al. 2020). However, in the present work, we choose to combine all spectral channels of all four sub-bands in the deconvolution process when producing the intensity maps as this results in better sampling of the Fourier space and thus a higher signal-to-noise ratio, which is advantageous for the detection and analysis of small-scale dynamic features.

The output of the image reconstruction is cut off at a radius of 32.8″ from the center field of view (FOV). The cut-off point corresponds to 0.3 times the main beam power response. The pixel size of the final images is 0.32″. The "clean" beam, that is, a Gaussian fit to the main lobe of the point spread function (PSF) of the interferometric array constitutes the resolution element. The full width at half maximum (FWHM) of the clean beam varies slightly over time but has a mean value of about 1.4″ and 2.1″ along the minor and major axis, respectively, with a beam position angle of 68°.

Magnetic-field measurements are taken with the Helioseismic Magnetic Imager (HMI; Schou et al. 2012) on board the Solar Dynamics Observatory (SDO; Pesnell et al. 2012). The magnetograms, measuring the Fe I line (6173 Å) at photospheric heights, have a cadence of 36 s and are co-aligned with the ALMA observations. The SDO images are re-sampled to a pixel size of 0.32″ to match the ALMA data. For the spatial co-alignment, the ALMA images were cross-correlated with a combination of the 170 nm and 30.4 nm channels of the SDO's Atmospheric Imaging Assembly (AIA; Lemen et al. 2012).

2.2. Event definition and selection

The observational data are searched for signatures of small-scale dynamic events. For that purpose, the brightness temperature

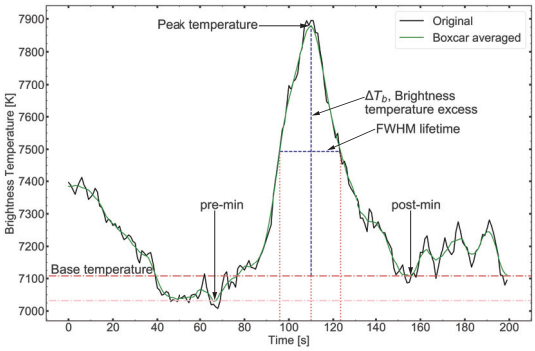

Fig. 1. Definition and selection criteria for a dynamic event. Temporal evolution of the brightness temperature at a selected pixel exhibits a peak enclosed by two minima (pre-min. and post-min.). The green graph shows the box-car average of the original data (black graph). The blue dashed lines mark the peak amplitude and FWHM lifetime. The horizontal red dashed-dotted line marks the temperature of the local minima with highest temperature; in this case the post-peak minima, which is the base brightness temperature considered for the specific event. The pink dashed-dotted line shows the temperature of the other minima; in this case the pre-peak minima. The red dotted lines mark the times where the temperature is at FWHM and peak.

The observational data are time evolution ($T_b(t)$) of each pixel is studied. To remove high-frequency noise, the data are box-car averaged in time with a size of seven time steps (14 s). The resulting smoothed data are then searched for peaks in brightness temperature at every pixel, comprising an increase followed by a decrease in brightness temperature (cf. Fig. 1), with an amplitude of at least 400 K. The amplitude of the peak in brightness temperature excess is measured as the difference from the base temperature level as determined by the closest significant local minima of $T_b(t)$ at a given spatial position. To remain conservative, the minimum with the smallest T_b difference from the peak is chosen. The lifetime of an event is then determined as the FWHM of the brightness temperature excess peak (see Fig. 1).

The pixels showing such a temporary rise in brightness temperature are grouped together using the *k*-means clustering method (Everitt 1972). Each resulting cluster represents an individual event. The *k*-means clustering method sorts multidimensional data into a predefined number of clusters and then assigns the pixels to clusters depending on the euclidean distance in spatial and temporal coordinates with respect to the mean value for each cluster. The suitable number of clusters is determined by a combination of the following two methods:

(i) Start with a small number of clusters and perform the *k*-means clustering, calculate the entropy (i.e., the mean of the spread within the clusters), and then iteratively repeat the process with an increasing number of clusters. At last, pinpoint the number of clusters where the entropy does not drop significantly compared to previous steps with a smaller number of clusters. This method is commonly referred to as the "elbow method".

(ii) Compare each data point to its own cluster and to the closest neighboring cluster to see which cluster it is most closely related to. This method is commonly referred to as the "silhouette method".

In the central parts of the FOV, the events are more easily separated than when going towards the outer parts of the FOV. We conclude that this effect is caused by the radial increase of T_b uncertainties resulting from the image reconstruction process of the interferometric measurements. The uncertainties becomes very pronounced in the outer parts of the FOV. Because of the lower reliability of the data in these parts, the *k*-means clustering is only applied to the innermost parts within a radius of 15″.

In that inner region, all events are taken into account that (*i*) show clear peaks with a brightness temperature excess of more than 400 K and (*ii*) are fully represented in a single time scan. Thus, the length of the time scans (10 min) restricts the amount of events detected. Since the imaging procedures of solar ALMA data are still in an early stage, the criteria are defined more conservatively for this initial study in order to minimize the number of false detections.

3. Results

3.1. Events with peaks in the temporal evolution of the brightness temperature

A total number of 552 events are found within the inner parts of the FOV with a radius of 15″(see Sect. 2.2 for the selection criteria). The individual events are well distributed over almost the entire selected part of the FOV and all four time scans as can be seen from the spatial and temporal coordinates of the individual events in Fig. 2.

There are some parts, dominated by the top part as well as smaller segments in the bottom of the inner region, that do not show any events with brightness temperature variations of more than 400 K (Fig. 2d). This is because of the presence of strong magnetic fields and is studied further in Sect. 3.2.

The events have spatial sizes up to about 9″ which corresponds to ∼4.3–6.4 times the clean beam. The spatial size of an event is indicated by the maximum euclidean distance between the pixels within the event. However, the majority of events are smaller than ∼2.5″, which can be seen in Fig. 3 where the distribution of spatial sizes is presented. From the peak value at 2.5″, there is a steady decrease in the number of events towards larger sizes. Events smaller than the clean beam axes cannot be spatially resolved, resulting in a decrease in the occurrence rate towards smaller sizes. Pronounced events might be detected despite being not spatially resolved but a larger number of events with smaller sizes is expected.

For a specific event, each pixel has a well-defined time for the maximum peak brightness temperature which is plotted in panels b and c of Fig. 2. The lifetime and magnitude of the peak brightness temperature (ΔT_b) vary between the pixels within a single event. These variations are caused by a combination of the inherent properties of the evolution of different parts of the events and the limited spatial resolution, which effectively smooths out the signatures. A more detailed discussion of these issues is provided in Sect. 4. For this study, the overall lifetime of the event is determined as the FWHM of the peak within the event with the largest T_b excess (cf. Fig. 1). The resulting values of lifetime and excess in T_b vary significantly among the individual events. The lifetimes range between ∼43 and 360 s and the brightness temperature excess ΔT_b between the cut-off limit of 400 K up to ∼1200 K. A statistical analysis of these results is presented in Sect. 3.3.

3.2. Magnetic field strength and network/internetwork mask of the entire FOV

The observed quiet Sun region is composed of magnetic network (NW) and interwork (IN) regions (Wedemeyer et al. 2020).

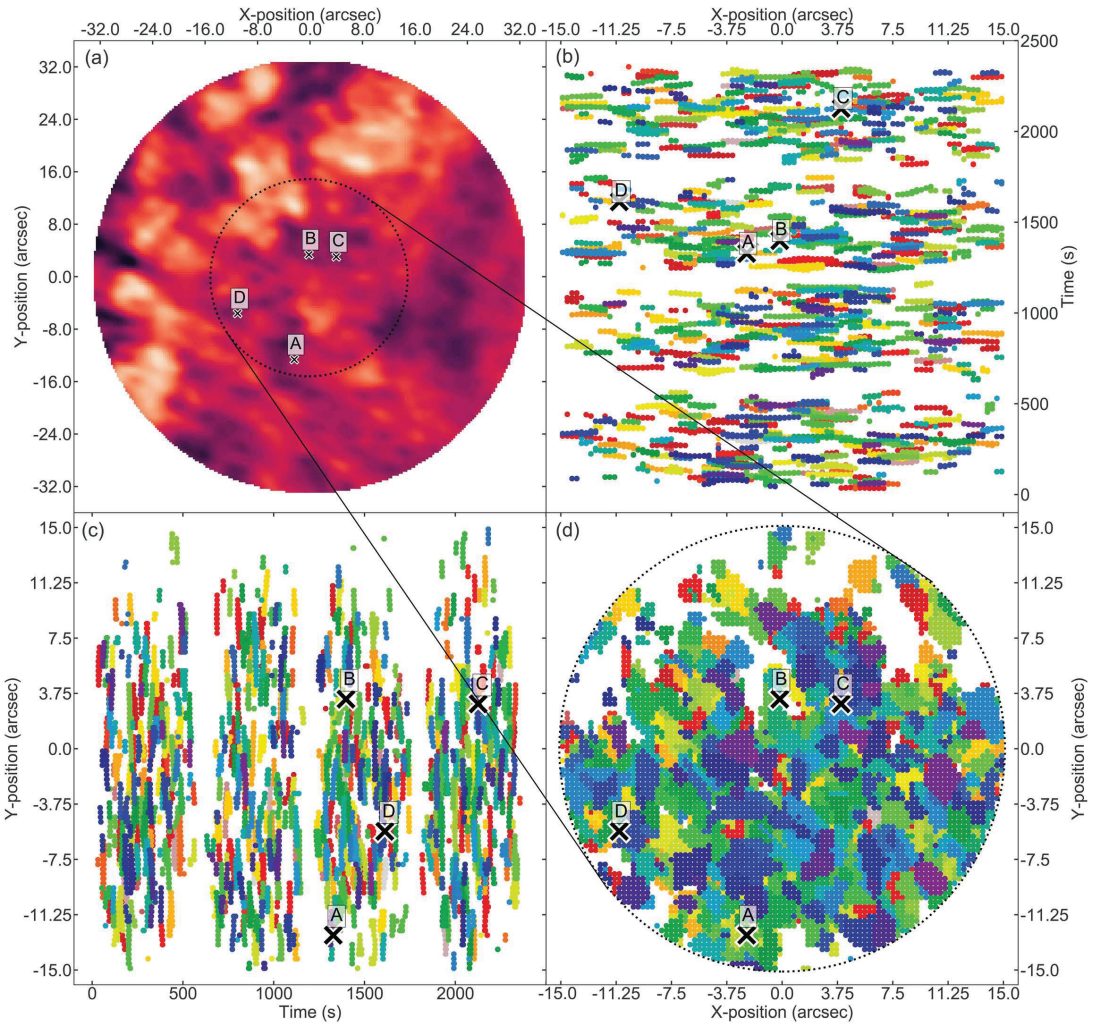

Fig. 2. Spatial and temporal position of all 552 detected temperature peak events within 15 arcseconds from the center of the FOV and with a magnitude of at least 400 K. (*a*) Brightness temperature map of the first frame of the dataset (2 s integration). The black dotted circle marks a radial distance of 15″ from the center of the FOV. (*b*) The *x*-axis position and (*c*) the *y*-axis position of all brightness temperature peaks plotted against time, respectively. The events are all colored individually, showing the same color for the same event in all panels. (*d*) The *x*-axis and *y*-axis positions of all temperature peaks. The locations of a few selected events (A, B, C and D) that are studied in detail in Sect. 3.4 are marked with crosses in all panels.

The magnetic field strength of the entire FOV, averaged in time over the ALMA observation period, is shown in the SDO/HMI magnetogram in Fig. 4a and ranges from −160 to 230 G. The strongest magnetic fields are present in the top parts of the FOV as well in the lower left corner. In the top right, there are two nearby locations with concentrations of opposite polarity. Between these locations, there are magnetic loop structures observable in many of the SDO-AIA channels. This group of compact loops is also seen in the ALMA Band 3 maps (Wedemeyer et al. 2020). The NW/IN mask by Wedemeyer et al. (2020) is overplotted in Fig. 4. This mask was composed based on time-averaged observational maps from SDO-AIA in 160 and 170 nm and saturated SDO/HMI magnetograms in combination with the ALMA maps. The locations of the stronger magnetic fields and their polarities are roughly stationary during the time period of the ALMA observations and therefore an average over the whole observational period is used when defining the different areas.

Using a NW/IN mask is a commonly used method for distinguishing between different types of regions, but as such represents a compromise across the considered observation period and different imprints of the network in the considered atmospheric

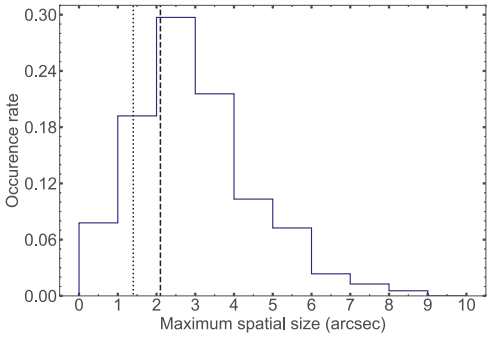

Fig. 3. Spatial size distribution of the 552 detected events, represented in bins with width of 1.0″. The vertical dotted and dashed lines mark the sizes of the clean beam minor and major axis, respectively.

layers. Consequently, such a mask does not always adequately represent the conditions at the exact time and location of a specific dynamical event, such as those discussed here. The mask is shown nonetheless in order to facilitate comparisons with other studies using NW/IN masks (e.g. Loukitcheva et al. 2009) and with our previous paper (Wedemeyer et al. 2020).

In Fig. 4b, all pixels that show a peak with brightness temperature excess with a minimum amplitude of 400 K and a lifetime shorter than 200 s in the entire FOV and in all of the four time scans are marked. The contours of the time-averaged magnetic field strength and the NW/IN mask are overplotted for direct comparison. The occurrence of T_b peak signatures is much lower in the upper and left parts of the FOV, where the magnetic field strength is stronger on average, as well in a few patches at a radial distance of ∼15″ towards the bottom. It should be emphasised that the magnetic field structure varies significantly over time on small spatial scales with nonaveraged line-of-sight (LOS) magnetic field strength spanning between [−260, 300] G. As a result, some T_b peaks appear to occur at locations with stronger time-averaged LOS magnetic field strength (Fig. 4b), while the actual magnetic field strength at the exact time of (and before) the occurrence of the peak is typically much lower. For this reason, a histogram for the LOS magnetic field strength at the exact location and the time of each T_b peak is shown in Fig. 4c in comparison to the distribution of all magnetic field strength values in the data set. The ratio of the two distributions seems to remain more or less constant for LOS magnetic field strengths below ∼180 G but decreases with increasing magnetic field strengths beyond that point. This finding implies that the occurrence of brightness temperature peaks is reduced at locations with a LOS magnetic field strength of ≳180 G but the number of detections on which this conclusion is based is rather low. Furthermore, while the degree to which one can relate the SDO/HMI magnetograms measured at photospheric levels to the ALMA maps originating at larger heights is uncertain, it is valuable to point out that there are no T_b peaks at locations with absolute LOS magnetic field strengths greater than ∼250 G, which suggests that the presence of magnetic fields impacts the occurrence of the analyzed dynamic small-scale events.

3.3. Statistical study of detected events

For each of the 552 events (described in Sect. 3.1) the maximum T_b excess, lifetime, and base brightness temperature (cf. Fig. 1)

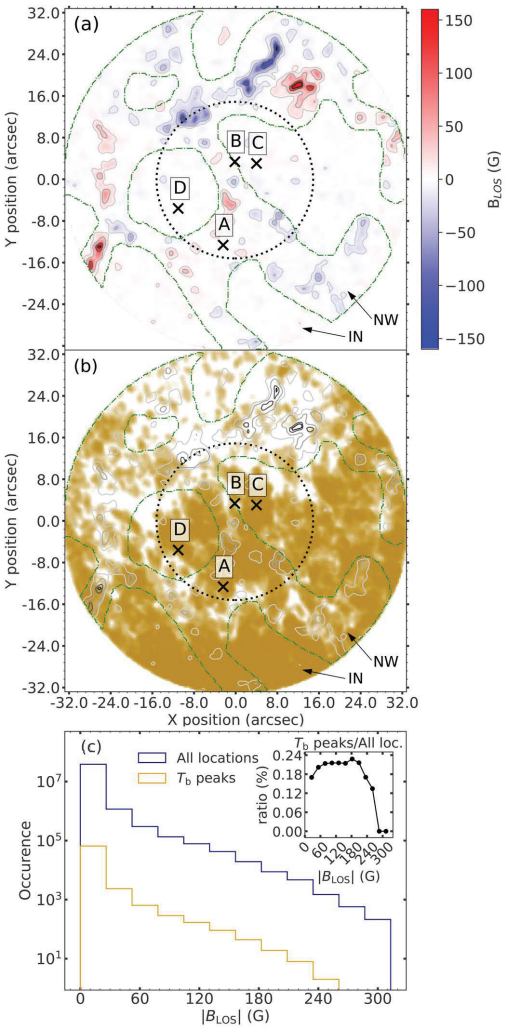

Fig. 4. Spatial comparison between brightness temperature dynamics in ALMA and SDO/HMI magnetogram. (*a*) The time-averaged SDO/HMI magnetogram for the whole ALMA FOV is presented as blue, white, and red shades with the value range saturated at [−160, 160] G. The absolute LOS magnetic field strength is outlined with gray contour lines with the levels 10, 30, 80, and 120 G. The green dotted-dashed lines mark the mask defining the borders between network and internetwork regions. The dotted ring marks the radial distance of 15″ from the center of the FOV. The spatial positions of the selected events A–D (Sect. 3.4 and Appendix B) are marked for reference. (*b*) The spatial position of all instances in the entire FOV with a T_b excess of more than 400 K and a lifetime shorter than 200 s, at any time in the data, are marked with orange-brown dots. The white spaces are therefore locations without any events and a single pixel can show several T_b instances. The gray contour outlines the SDO/HMI magnetogram, whereas the green dotted-dashed contours, the dotted ring, and the crosses A–D mark the same as in *panel a*. (*c*) Histograms of the absolute LOS magnetic field strength at the locations and times of the T_b peaks marked in *panel b* (orange-brown) and for the entire HMI data set (blue). The inset plot shows the ratio of the two histograms.

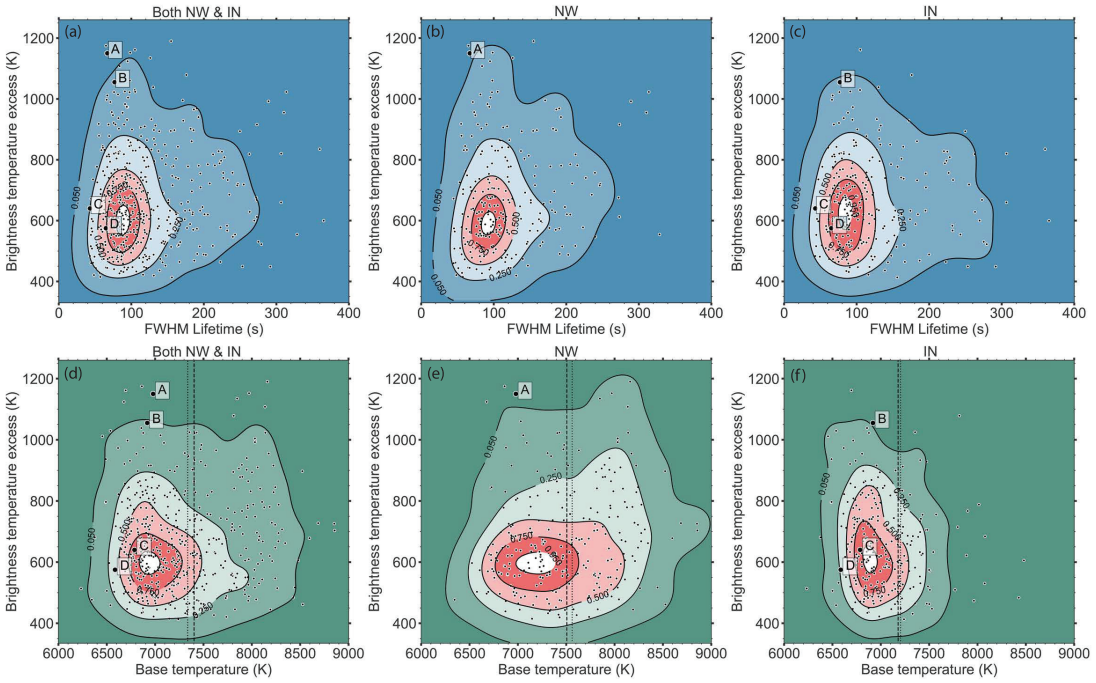

Fig. 5. Statistical study of all the events, with comparison between the regions defined by the NW/IN mask. The first column (*panels a and d*) shows all the events, the second column (*panels b and e*) shows the events within the NW mask, and the third column (*panels c and f*) shows the events within the INmask. For each event, the *first row* shows the brightness temperature excess plotted against the lifetime and the *second row* shows the brightness temperature excess plotted against the base brightness temperature. The distributions are represented as density maps and the contour lines mark the levels of 0.05, 0.25, 0.5, 0.75, and 0.95. The dotted and dashed lines in *panels d, e, and f* show the median and mean value, respectively, of the brightness temperature of all pixels within 15″ during the entire dataset. The selected events A–D (Sect. 3.4) are marked in all panels for reference.

are given in Fig. 5. As mentioned in Sect. 2.2, the T_b values in the outskirts of the FOV are less certain and events detected there are therefore not considered further for the detailed analysis of event properties. In the panels of the first column, all the events are plotted while the events are split up according to the NW/IN mask in the second (NW) and third (IN) columns. In all panels, the selected examples A–D are marked, which are described in detail in Sect. 3.4. In the first row, the lifetime of the events is plotted against their maximum brightness temperature excess (ΔT_b). While the distribution in both lifetime and ΔT_b appears to be continuous for all the events (Fig. 5a), there are a couple of noteworthy trends: (*i*) The density distribution of the scatter plot indicates the most frequent events have a typical brightness temperature excess of $\Delta T_b \sim 600$ K and a lifetime of ~90 s, with values in the ranges of ~450–750 K and ~55–125 s, respectively, for 50% of the distribution. (*ii*) There are no events with a lifetime below 43 s that also have a brightness temperature excess above 400 K. This finding is discussed in connection with the effects of limited angular resolution in Sect. 4.2. The events that fall within the NW and IN areas of the mask shown in Figs. 5b and 5c, respectively. The distributions of lifetime and brightness temperature excess for the NW and the IN areas are qualitatively similar but differ in a few aspects. Most of the relatively few events with larger T_b excess (above ~1050 K) are detected in the NW regions. However, this does not imply that stronger magnetic field gives rise to larger T_b excess, as we see in Fig. 6. Similarly, the events with low T_b excess and long lifetime (up to ~300 s) tend to lie within the IN regions but this affects only a small number of events.

The base temperature (cf. Fig. 1) could potentially affect the T_b excess amplitude of an event. The brightness temperature excess is plotted against the base brightness temperature for all events in Fig. 5d. There is a continuous distribution of events with base brightness temperatures in the range of ~6400–8300 K for all brightness temperature excess values ΔT_b between ~400 and 1000 K. The density plot in Fig. 5d indicates that most events exhibit a base brightness temperature of around 6600–7500 K. The mean and median brightness temperatures of all pixels within the same area as the considered events (15″ radius and NW/IN respectively) for the entire time of the dataset are marked as references in Figs. 5d–f. The mean and median temperatures of the whole area are $\langle T_b \rangle_{x,y,t} = 7402$ K and 7336 K, respectively, which corresponds to the upper segment of the base temperatures shown for the events. This is naturally a cause of the base temperatures being defined at local minima of the T_b evolution. The separation of the events in NW and IN areas shows that there are more events with higher base temperature in the NW areas than in the IN areas (Figs. 5e–f. In accordance with higher (average) temperatures in the NW regions, the majority of events in the NW areas exhibit base

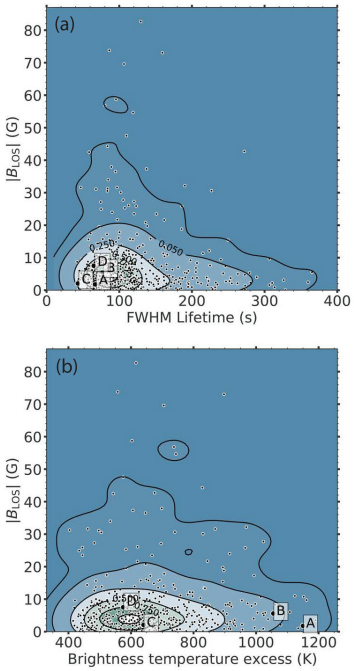

Fig. 6. Statistical study of all the events within 15″ radius from the center FOV. (*a*) The absolute LOS magnetic field strength plotted against the lifetime for each event. (*b*) The absolute LOS magnetic field strength plotted against the T_b excess. The scatter plots are represented as colored density maps with the contour lines marking the levels of 0.01, 0.05, 0.25, 0.5, 0.75, and 0.95 of the total distribution. The selected events A–D (Sect. 3.4) are marked in all panels for reference.

temperatures of up to ~8100 K, whereas there only a few events in the IN areas with such high values. The lower limit is however almost the same for the two masked areas, which comes naturally as the NW mask contains very quiet patches as well at some locations and times. For the NW regions alone, the mean and median values are 7561 K and 7506 K, and for IN alone the values are smaller, 7204 K and 7179 K, respectively. The mean of the brightness temperature is slightly higher than the median and is most pronounced in the NW areas, but is also evident in the IN areas, which suggests that there are only a few features but that these are very bright. Even though there is a significant shift towards larger base brightness temperature for the NW regions, the distribution of magnitude of the T_b excess is similar and there is only a mean brightness temperature difference of about 360 K between NW and IN areas. These results imply that the physical conditions behind the occurrence of the registered dynamical T_b excess events are not very dependent on base temperatures in the analyzed quiet Sun region.

As expected from the studies of other chromospheric diagnostics (see, e.g., de Wijn et al. 2009; Loukitcheva et al. 2009, and references therein), the (base) brightness temperature in ALMA Band 3 correlates with the (time-averaged) magnetic field strength in the photosphere (see Wedemeyer et al. 2020, for the analyzed data set). In Fig. 6, for each of the 552 events, the relations between the magnitude of the maximum brightness temperature excess ΔT_b, the lifetime, and the SDO/HMI

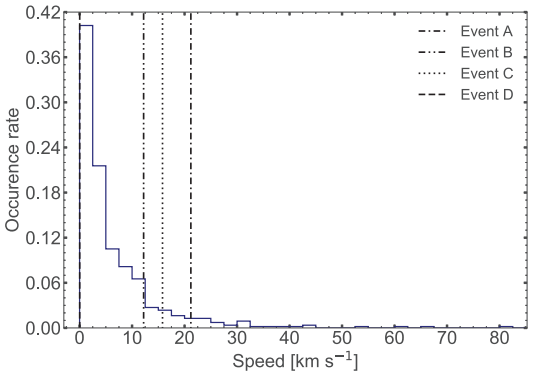

Fig. 7. Distribution of the speed of apparent motion of the 552 events. The speeds of events A–D (Sect. 3.4) are marked for reference.

LOS magnetic field strength are shown. The absolute LOS magnetic field strength is given at the spatial location and the time of the maximum excess T_b peak for each event. The absolute magnetic field strength at the locations of the detected events ranges up to ~80 G. The majority of the events occur at locations with very low magnetic field strength below 10 G and as many as 95% of the events are found at locations with an absolute magnitude of ≤20 G. There are some events with higher absolute magnetic field strength which are primarily occurring in the NW areas. However, even in the NW areas, the locations of the majority of the events show a low magnetic field strength similar to the events in the IN areas. This is because of the small-scale structure of the magnetic field unaccounted for by the time-averaged NW/IN mask. The NW regions therefore still contain many areas with low average magnetic field strength, as can be seen in Fig. 4a, where there are many white patches also in the NW area. The events associated with larger absolute LOS magnetic field strength have shorter lifetimes, centered around 100 s, similar to the majority of events. The events with longer lifetimes tend to occur at locations with a weak magnetic field. A similar but less clear trend can be seen in the brightness temperature excess with a larger spread of values for the events with larger magnetic field strength, similar to the distribution of the events with weak magnetic fields. These results may suggest that a strong LOS magnetic field disturbs the generation of events with long lifetime or higher amplitude (ΔT_b). Even though the statistical sample is rather large with 552 events, a larger number of events with higher magnetic field strength is required in order to draw firm conclusions.

Apparent motion. In addition, the apparent motion is estimated for each event. This is done by looking at the change of position of the brightest point within the spatial extension of the event between the points in time at FWHM of the peak with largest T_b. The individual velocity components in *x*- and *y*-axis are found to be normally distributed around zero, which insinuates that there is no preferred direction of the apparent motion of the events. The probability density function of the total absolute apparent velocity is given in Fig. 7. Approximately 80% of the events show low speeds below 10 km s^{-1} and the rest show speeds between 10 and 30 km s^{-1}, except for a handful of events with indications of high speeds of several tens of kilometres per second.

Repetitiveness of events. Some of the events occur at similar locations but with a delay in time, which can be inferred from comparing and tracing individual events between the panels in Fig. 2. An estimation of the repetitiveness of events is made by taking the spatial and temporal locations of the points with largest magnitude of T_b excess in each event and calculating how many of these are within a certain spatial distance from each other. Approximately 22% of the events occur within a spatial distance of 1″ and within the same time scan (of ∼10 min; Sect. 2.1) as another event. For these events occurring at close-by locations, the delay between the occurrence of the brightness temperature peaks of two events is typically $\Delta t_{peaks} = 200$ s, although a continuous distribution of delays of up to approximately $\Delta t_{peaks} = 320$ s and in a few cases even up to $\Delta t_{peaks} = 430$ s is found. It should be noted that the statistical significance of the derived delays is limited by the duration of the observational time scans and the spatial threshold (here set to 1″) in relation to the angular resolution. The complexity of the 3D structure of the solar chromosphere on small spatial scales in combination with the limited angular resolution can significantly affect the observable signatures of dynamic events at mm wavelengths (see the discussion in Sects. 4.2 and 4.3). Consequently, propagating shock waves that are excited at photospheric heights can appear very different even if they were excited at the same location. Indications of the repetitiveness of events can be seen in the time evolution graphs of the selected examples in Figs. 8–9 and B.1–B.2.

3.4. In-depth study of selected events in the observational data

A couple examples of dynamic events, representative for different segments of the parameter space (see Figs. 5 and 6), are illustrated in Figs. 8 and 9. Event A exhibits more pronounced brightness temperature amplitude and event C shows a weaker T_b excess, representative of the most frequently detected events (as seen in Fig. 5a). An additional two examples (events B and D), showing similar signatures yet with different details, are presented in Appendix B. All four events are marked in Figs. 2–6 for reference.

Event A, which is located at $(x, y) = (-2.4'', -12.6'')$, is shown in Fig. 8. The lower right panel h shows the time evolution of the brightness temperature at a fixed location with a rise from $T_b = 6980$ K to 8130 K over about 53 s. After reaching the peak, the brightness temperature decreases again to 6940 K over the course of 67 s, to only slightly below the initial T_b value. Event A therefore has a temperature excess of $\Delta T_b = 1150$ K and a lifetime of 67 s. The area connected to the event, for example the area that shows a brightness temperature of at least half the maximum of the ΔT_b peak, has a round shape with a maximum diameter of roughly 4 arcsec. The upper row with five panels shows a time series of close-ups of the surroundings of the event. The event develops rapidly at one location in the FOV and expands in all directions and then decreases in brightness whilst remaining relatively (horizontally) stationary apart from a rightward motion component. Even though the limited angular resolution makes it challenging, the apparent movement through time of the brightest point, of approximately 22 km s^{-1}, can be seen in the space-time diagrams in the lower left panels (Figs. 8f-g). As indicated in Fig. 4, event A is located in the NW region, but still shows a weak absolute magnetic field strength of only ∼18 G. In the T_b time evolution (Fig. 8h), two weaker succeeding peaks can be seen approximately 4.5 min and 7 min after the strong peak of event A. Even though these specific peaks might not fulfill the $\Delta T_b > 400$ K requirement used in the selection of the events (Sect. 2.2), the time delay is in line with the numbers presented in Sect. 3.3 for the repetitiveness of events. Another strong event B showing many similarities to A is illustrated in Fig. B.1 for reference.

Event C (Fig. 9) occurs at the location $(x, y) = (4.0'', 3.0'')$ close to event B, but more than 6 minutes later in time. The brightness temperature increases from 6790 K to 7430 K, resulting in $\Delta T_b = 640$ K and a lifetime of 43 s. After reaching the T_b peak, there is a significant drop to about 6200 K. As can be seen in the space-time diagrams in the lower left panels, the temperature in the area drops to about 6000 K. We conclude that this more pronounced contrast is likely caused by the formation of a slightly larger-than-average post-shock region. In the ALMA data presented here, such regions are typically seen as round shapes with diameters on the order of up to a few arcsec. However, most of these regions have typical diameters of 1−2″, which is at or below the resolution limit in the ALMA Band 3 data used here. The post-shock region occurring in connection to event C is slightly larger and therefore better resolved, revealing a larger T_b contrast. See Sects. 4.2 and 4.3 (and in addition, e.g., Wedemeyer-Böhm et al. 2007; Loukitcheva et al. 2015) for a discussion on the impact of low spatial resolution on observations of propagating shock wave patterns. The bright feature appears stable in the horizontal plane with just a subtle movement towards higher values on the x-axis (Fig. 9). The speed of the apparent motion is ∼15 km s^{-1} at FWHM. Event D, which is similar to event C but supposedly even more on the limit of being resolved, is presented in Fig. B.2.

As we discuss in Sect. 4.3, the angular resolution achieved for the analyzed ALMA Band 3 observations is at the limit for resolving the chromospheric shock-wave-induced pattern. In areas with short distances between neighbouring shock waves, most of the resulting mesh-like pattern remains unresolved. There, the shock peaks do not stand out from the surroundings, but instead the observed dynamical structure is dominated by the darker (post-shock) regions. The latter example, event C, indeed shows less clearly isolated features (similar to event D in Fig. B.2). This could contribute to the apparent lower values of the most represented ΔT_b amplitudes than what would be seen with higher angular resolution.

4. Discussion

4.1. One-dimensional numerical simulations of propagating shock waves

In order to check whether or not propagating shock waves could be producing the observed brightness temperature events, we study numerical simulations and calculate the radiative transfer in mm wavelengths. The hydrodynamic code RADYN (Carlsson & Stein 1992, 1997, 2002, 1994) produces one-dimensional dynamical model atmospheres where a moving piston in the lower boundary excites waves. RADYN solves the equations of conservation of energy, momentum, and mass, the radiative transfer equations in nonLTE, and the rate equations of atomic level populations. Loukitcheva et al. (2004, 2006) present T_b signatures at mm wavelengths resulting from RADYN runs for which the waves are excited by the driving piston with velocities set to match photospheric Doppler velocities obtained from observations in the Fe I line at $\lambda = 396.68$ nm (Carlsson & Stein 2002). In the time series, with lengths of ∼1 h, waves with varying strength and speed are excited, allowing some of them to interact. The resulting shock wave signatures at

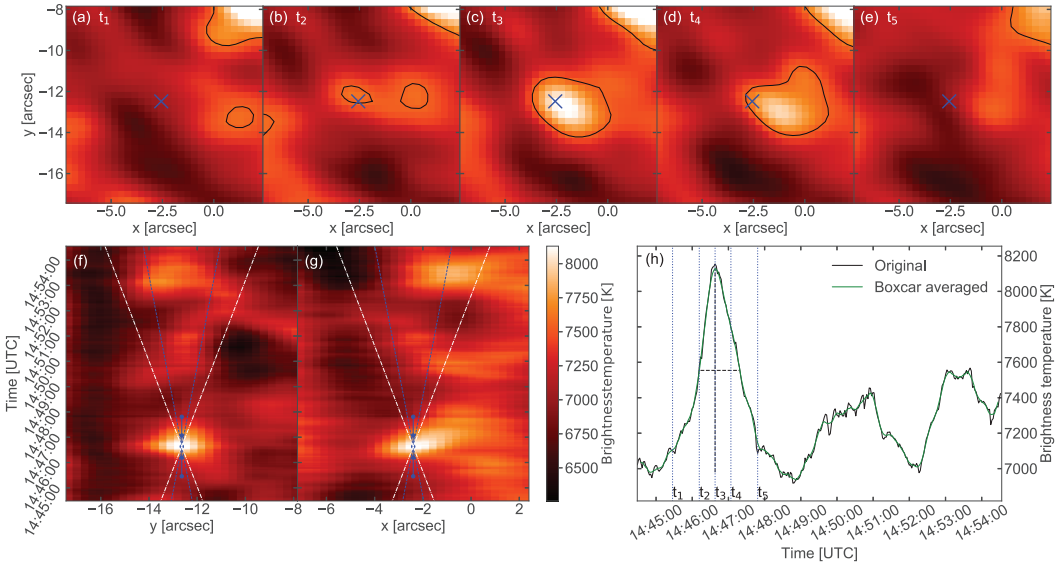

Fig. 8. Detailed study of event A. (*a*)–(*e*) The *top panels* show a close up of the surroundings at different time steps, t_1 to t_5 *from left to right*, through the shock wave event. The time of the T_b peak is marked by t_3 = 14:46:38. Here, t_1 and t_2 mark 70 s and 26 s prior the peak and t_4 and t_5 mark 26 s and 70 s after the peak. The center location is marked by a blue cross. The contour lines mark half of the maximum ΔT_b peak. (*f*)–(*g*) Space-time diagrams for a vertical and horizontal slit across the FOV at the center location, which is marked with blue dots for the time steps t_1 to t_5. Velocity slopes for 10 and 20 km s^{-1} are indicated by blue dotted and white dashed lines, respectively. The color code is the same in all panels. (*h*) The time evolution of the brightness temperature of the center location, where the time steps t_1 to t_5 are indicated by blue dotted vertical lines. Both the original data (black) and the averaged data (green) are shown. The horizontal and vertical black dashed lines mark the event lifetime and brightness temperature excess.

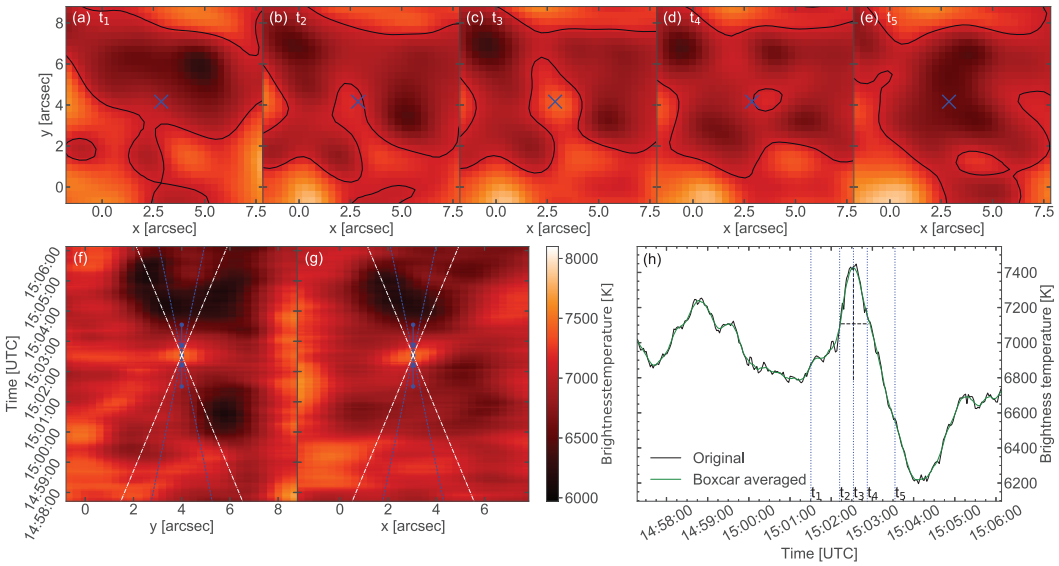

Fig. 9. Detailed study of event C, as provided for event A in Fig. 8. The time of the T_b peak is marked by t_3 = 15:02:32. Here, t_1, t_2, t_4 and t_5 mark −60, −20, 20, and 60 s from the peak, respectively.

a wavelength of 3.4 mm (see Fig. 1c in Loukitcheva et al. 2006), which is close to the wavelengths currently offered for solar observing with ALMA in Band 3, show ΔT_b amplitudes of between a few hundred K to ~4000 K and lifetimes in the range of approximately 15−50 s. Some events are double-peaked, showing a long lifetime, which seems to be the result of interacting waves. Wave interference can therefore significantly contribute to extending the apparent lifetime of an event. In order to mitigate any input bias of the observational Doppler velocities, we perform a parameter exploration with a series of monochromatic waves covering large parameter ranges. This allows us to see under which circumstances shock waves can give rise to T_b signatures that are in line with the observed signatures described in Sect. 3.3. The RADYN code is used and the initial conditions are set by a VAL model atmosphere (Vernazza et al. 1981) with the addition of a transition region and corona (Carlsson & Stein 2002). The lower boundary is set to 100 km below where the optical depth is unity at a wavelength of 500 nm. The upper boundary is at a height of 10^4 km, where the temperature is set to 10^6 K. To resolve small-scale variations arising from the propagation of shock waves, an adaptive mesh is used (Dorfi & Drury 1987). The duration of the simulations is 1500 s and thus long enough for the relaxation phase of the atmospheres to pass and for several shock waves to propagate through. The cadence of the output is 1 s. The piston at the lower boundary excites sinusoidal acoustic waves where the initial amplitude and the periodicity are varied independently.

The amplitude is varied between 0.001 and 0.15 of the local sound speed, v_0, at the lower boundary, and the periodicity is varied between a few seconds up to several minutes. Distinct shock waves are excited with an initial amplitude of between $0.005v_0$ and $0.05v_0$ and wave periodicity between P = 90 and 210 s. The waves steepen into shock waves around 1 Mm and propagate through the chromosphere with a speed of approximately 9.4 km s^{-1}. The radiative transfer through the dynamical atmosphere models is calculated using the RH 1.5D code (Uitenbroek 2001; Pereira & Uitenbroek 2015). The output continuum intensities (I_ν) are converted to brightness temperatures through relation (1).

For each time-step, the mean value of the brightness temperatures of all four sub-bands of ALMA band 3 (see Table 1) is calculated to match the spectral setup of the full band integrations in the ALMA observations, which makes a one-to-one comparison possible. The temporal evolution of the simulated Band 3 brightness temperature is shown for the different simulation runs in Fig. 10. Each shock wave signature consists of a rapid increase in brightness temperature, reaching a peak, and followed by a post-shock drop in brightness temperature. The case of a static unperturbed atmosphere is given as a reference.

We note that, when going towards lower initial wave amplitudes, a preceding temperature peak is growing stronger and partly merges with main peak. The presence of a preceding peak is most prominent in the case of $A_i = 0.005v_0$, where the minimum brightness temperature is significantly enhanced in connection with the main peak for more than 60 s, as well as throughout the entire cycle. Such double-peaked temporal profiles are also seen in the series with different wave modes (Loukitcheva et al. 2004, 2006), as a result of interference between waves. We also note that some of the observational examples, specifically event C (Fig. 9), exhibit a very subtle increase in T_b preceding the main peak, which might be consistent with the small preceding secondary peaks seen in the simulations for certain parameters.

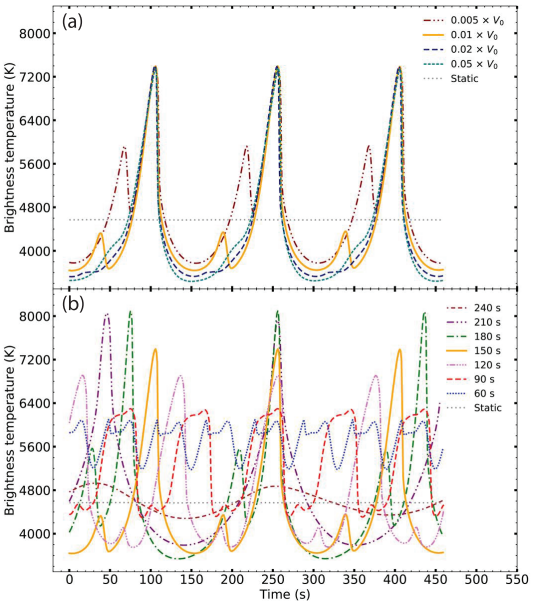

Fig. 10. Evolution of brightness temperature with propagating shock waves. (*a*) Variation of the initial wave amplitude A_i between 0.5% and 5% times the local sound speed at the lower boundary (v_0). The periodicity is kept at 150 s. (*b*) Variation of the wave periodicity between 60 and 240 s, where A_i is kept at 0.01 v_0. The orange graph in *panels a and b* represents the same run; in both panels, the case of a static atmosphere without any disturbances is plotted as reference with a gray dotted line. The runs are shifted in time to align the time of their peaks.

Figure 11 shows the brightness temperature excesses and the lifetimes of the shock wave signatures. The parameter exploration reveals that the variations of the initial amplitude only have a small impact on both the brightness temperature excess ΔT_b, which is found to be on the order of 3500–3900 K and on the lifetimes, with values of between 21 and 25 s. In contrast, the wave periodicity has a large impact on the brightness temperature excess and signature lifetime (Fig. 11, panels a and c). In the case of long periodicity of P = 240 s, the T_b signature shows a low brightness temperature excess of only about ~550 K with a corresponding long lifetime of ~100 s. This agrees with the results of Loukitcheva et al. (2006), where they show that at wavelengths of ALMA band 3, the intensity in the power spectrum at 240 s (4.2 mHz) is very low whilst the peak is found at a period of 175 s (5.75 mHz), which agrees well with Fig. 11a. A short periodicity of P = 60 s gives rise to ΔT_b = 900 K and a lifetime of 40 s. However the bulk shift towards higher temperatures (Fig. 10b) indicates that the atmosphere is not allowed to relax between the passages of waves. For the cases between P = 90 s and 210 s, with clear T_b shock wave signatures, values of the brightness temperature excess of between ~2000 K and 4450 K are seen, together with lifetimes of between 16 s and 45 s. This is consistent with the results from the series of waves derived from photospheric Doppler velocity measurements (Loukitcheva et al. 2006).

In conclusion, shock waves with reasonable wave parameters in agreement with observational constrained values give rise

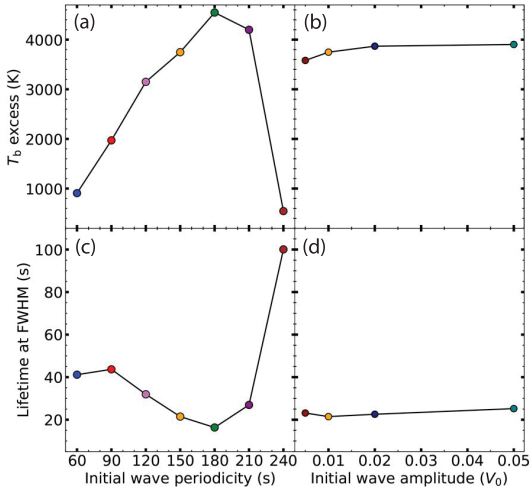

Fig. 11. Change of temperature and lifetime of shock wave signature with varying wave parameters. (*a*) Change of temperature as a function of initial wave frequency. (*b*) Change of temperature as a function of initial wave amplitude. (*c*) Lifetime at FWHM of the brightness temperature excess peak as a function of initial wave frequency. (*d*) T_b peak lifetime as a function of initial wave amplitude. The color scheme is the same as in Fig. 10.

to signatures with brightness temperature excess ΔT_b from a few hundred Kelvin up to approximately 4500 K (at wavelengths of ALMA band 3). ΔT_b of 4500 K are about three to four times larger than what is seen in the observational ALMA data. In the following section we explore a possible explanation for this.

4.2. Shock wave propagation in a 3D environment

The one-dimensional simulations are only an idealized first approximation, whereas for shock wave signatures in the observational data the following two factors have to be considered: (*i*) Many of the shock wave signatures are not fully resolved and there is spatial smearing with the surroundings that comes from sampling with the relatively large clean beam. Wöger et al. (2006) demonstrated that the dynamical timescale of the chromospheric small-scale internetwork structure does indeed increase when lowering the spatial resolution. (*ii*) The shock waves propagate through an inhomogeneous three-dimensional medium that is shaped by previous waves and magnetic fields. The shock waves can also interfere with each other and a fully isolated shock wave event as in the one-dimensional simulations might be difficult to observe. Both constructive and destructive interference could change the observed brightness temperature.

Propagation of shock waves in a more realistic 3D environment is demonstrated here by means of numerical simulations with the Bifrost code (Gudiksen et al. 2011; Carlsson et al. 2016); see also Eklund et al. (2020) for a detailed analysis of an exemplary shock wave event. Here, we study the observational imprint of shock wave propagation in brightness temperature maps calculated with the Advanced Radiative Transfer (ART) code (de la Cruz Rodriguez et al., in prep.) at wavelengths corresponding to ALMA band 3 (cf. Table 1). The ART code assumes LTE but takes into account relevant sources of continuum opacity in detail.

To estimate the magnitude of the degradation that comes with limited spatial resolution, the maps are degraded to the resolution of the ALMA band 3 observations by convolution with the clean beam (Sect. 2.1). An original T_b map for a selected time step is compared to the corresponding spatially degraded map in Figs. 12a–b). As expected, the fine structure on spatial scales smaller than the resolution limit is lost in the spatially degraded map. The location of an example of a propagating shock wave is marked in the respective mm maps. The evolution of the gas temperature surrounding the shock front is given in Fig. A.1 for reference. The time evolution of the brightness temperature at that location is shown in Fig. 12c for both the original map and the spatially degraded map. The propagating shock wave gives rise to a signature with a magnitude of $\Delta T_b = 3600$ K in the map with original resolution. In the map with degraded spatial resolution, the shock wave shows a signature with a substantially reduced magnitude of $\Delta T_b = 640$ K. The limited spatial resolution of the ALMA band 3 observations therefore results in an observable signature of this shock wave example, which has ∼0.18 times the original ΔT_b magnitude. Applying this conversion factor to the temperature excess seen in the 1D simulations with values between ∼2000 K and 4450 K would result in reduced values of ∼360 K–800 K. These values agree very well with what is seen in the observational data (Fig. 5), therefore implying that the observed signatures could be caused by propagating shock waves.

This is also in line with what Wedemeyer et al. (2020) demonstrated using the same Bifrost model. These latter authors find that applying the Band 3 synthetic beam reduces the brightness temperature standard deviation T_b^{rms} from 1794 K to 1254 K for NW pixels and from 1304 K to 693 K for IN pixels, respectively, which is a factor of 0.70 for NW and 0.53 for IN. Applying these factors to the range of 900 K to 4600 K found with the 1D RADYN/RH simulations in Sect. 4.1 reduces the expected range of brightness temperature amplitudes in shock waves to 630 K–3220 K for NW pixels and to 480 K–2440 K for IN pixels. We note that interpolating the resolution-dependent T_b^{rms} values by Loukitcheva et al. (2015) to the resolution of the Band 3 data (here 1.4″–2.1″) also results in a reduction by a factor ∼0.7 with respect to the original resolution. Wedemeyer-Böhm et al. (2007) also investigated the impact of the spatial resolution on their simulated brightness temperature maps showing a small-scale shock wave pattern, although for a shorter wavelength of 1 mm. Using their Eq. (9) with a characteristic length scale of $D = 1000$ km and the angular resolution of the Band 3 data used here (2.1″–1.4″) results in a reduction by a factor 0.22–0.36. The expected range of shock wave brightness temperature amplitudes based on the RADYN/RH results presented here would then be reduced to a lower limit of 200 K–330 K and an upper limit of 1000 K–1700 K, which is much more in line with the range of values found in the observations in Sect. 3.3 (see Fig. 5).

The lifetime of the shock wave example is 70 s in its original resolution, and 61 s in the degraded resolution (Fig. 12c). The cooler pre-shock period around $t = 1000$ s is not apparent in the ALMA band 3 resolution which contributes to a shorter apparent lifetime. This example illustrates the fact that the lifetime of an event is heavily dependent on the surrounding dynamical structure and the extent (and orientation) of spatial smearing due to limited angular resolution. The resulting longer lifetimes seen in the 3D model and the observations as compared to the shorter lifetimes in the 1D simulations (Figs. 10 and 11) emphasises the

shortcomings of the 1D approach in this particular aspect and the need for a systematic study based on 3D simulations.

The 1D RADYN simulations predict lifetimes for shock wave signatures in the range from 15 s to 50 s (see Sect. 4.1). The simulations also show that it is possible that hydrodynamical wave motions, although not steepening into shock waves, could show longer lifetimes on the order of ∼100 s with a brightness temperature excess of at least 400 K (Fig. 10). The simulations indicate short-lived signatures well under one minute for shock waves. However, with a potential broadening of the temporal profiles, longer lifetimes are expected. The extent of this broadening is strictly dependent on the spatial smearing of the radiative maps, that is, the evolution of the surroundings of the signatures and the size of the clean beam.

While it is evident that the observable signatures in Band 3 brightness temperatures are highly dependent on resolution, it is also clear that a detailed comparison of simulated and observed signatures and a possible identification of shock waves as their source require a more direct approach using detailed 3D simulations (see Sect. 4.6).

4.3. Detection of events with limited spatial resolution

Even though many dynamical events with brightness temperature amplitudes of at least 400 K are detected, the distribution of the spatial sizes of the events (see Fig. 3) is most likely cut off at spatial scales corresponding to the size of the clean beam. It is plausible that the distribution can be extrapolated towards smaller sizes and that smaller events thus remain unresolved.

This assumption is supported by our study of the Bifrost simulation (Fig. 12), observations in other chromospheric diagnostics, for example in the Ca II K line at a spatial resolution of 0.7″ (Wöger et al. 2006), and other numerical simulations (e.g., Wedemeyer et al. 2004) that clearly show small-scale features beyond the resolution of the ALMA Band 3 data analyzed here. Similar studies to that presented here, using measurements with higher spatial resolution, would provide further insight. A higher spatial resolution with the same wavelengths could be achieved by making measurements with a more extended antenna array configuration.

As mentioned in Sect. 1, the typical spatial scale of the mesh-like pattern in the chromosphere originating from propagating shock waves is of the same order as the angular resolution of the ALMA data used here (Wedemeyer et al. 2004; Wöger et al. 2006; Wedemeyer-Böhm et al. 2007; Loukitcheva et al. 2015). Consequently, the limited spatial resolution of this dataset (1.4–2.1 arcsec) does not allow us to fully resolve the (sub)structure of the detected events, and potentially fails to detect small and weak events. Using the above-mentioned clustering technique, the 552 detected dynamical events in this dataset (within 15″ radius) must therefore be considered to represent a lower limit only. Rather, only the strongest events and events with strong contrast with respect to their surroundings are detected. The effect of low angular resolution on the visibility of the chromospheric small-scale pattern is demonstrated by Wedemeyer-Böhm et al. (2007), Loukitcheva et al. (2015), and Wedemeyer et al. (2020).

The spatial resolution of interferometric data is often improved by the *Earth-rotation aperture synthesis* technique (Ryle 1975). Although this is an ingenious technique, it is inherently limited to a temporal span below that of the typical dynamical timescale of the target, as otherwise information is lost. In the case of the highly dynamical chromosphere, the dynamical timescale is on the order of seconds. To properly resolve dynamical events we therefore require a cadence of a couple of seconds at the most.

4.4. Dependence on magnetic fields

The results of this work show that the dynamical brightness temperature signatures are not evenly distributed in the FOV but that strong magnetic fields coincide with a lower occurrence of T_b signatures (see Fig. 4). Despite the difference in formation heights between the (chromospheric) T_b signatures in the ALMA band 3 data and the (photospheric) LOS magnetic field strength given by the SDO/HMI magnetograms, a lack of T_b signatures is seen, specifically at the footpoints of stronger magnetic field structures. It should be emphasized again that it is important to specifically refer to the magnetic field strength at the exact time and location of the event, whereas the NW/IN mask shown in Sect. 3.2 (cf. Wedemeyer et al. 2020) is only providing a first reference for the overall properties of the magnetic environment. In summary, the lowered occurrence of events at times and locations of high magnetic field strength is in line with the observed signatures likely being caused by propagating shock waves.

4.5. Identification of shock waves.

Based on the analysis of the mm-wavelength observables from the 1D numerical models (Sect. 4.1), we adopt here the following criteria for shock wave signatures.

(i) A brightness temperature excess, ΔT_b, on order of a few hundred to thousands of Kelvin.
(ii) Lifetime on the order of tens of seconds.
(iii) Small lateral motion with speeds of less than a few tens of kilometres per second.
(iv) Low magnetic field strength.

Taking a closer look at the selected events A–D in Sect. 3.4 reveals that they fulfill all of the conditions in the list above. The events show significantly large brightness temperature excess (575–1150 K) as well as satisfying lifetimes (43–77 s) (Figs. 8–B.2). As indicated in Sect. 4.1, a shock wave propagates through the chromosphere with typical vertical speed on the order of $\sim$10 km s^{-1} and only a relatively small apparent motion within a few tens of kilometres per second is therefore expected. Events A–C show apparent speeds of between ∼12 and 22 km s^{-1}, while event D appears horizontally stationary (Figs. 7 and 8–B.2). All of the events (A–D) show velocities that lie within the regime expected for shock waves. Finally, all of the locations of the events only show a very small absolute magnetic field strength (Fig. 4). The fulfillment of the above criteria by the events in the ALMA observations do suggest that their signatures could originate from shock wave events.

The evolution of the surroundings of an event can provide clues as to the local atmospheric structure. At the position of event A, the brightness temperature increases and decreases repetitively independent of the surroundings (Fig. 8), which could be interpreted as a case of a wave train with multiple shock waves being excited at the same location in the photosphere below (see, e.g., Wedemeyer et al. 2004). In event D, it is possible to see the indications of a repetitive shock wave pattern at the center location (Fig. B.2h). Although, the previous T_b peaks are relatively weak.

The low spatial resolution makes it challenging to estimate motions on the short timescales of the lifetimes of the events. Further, the apparent motion of an event might be difficult to estimate if the event not well isolated. The low apparent motion

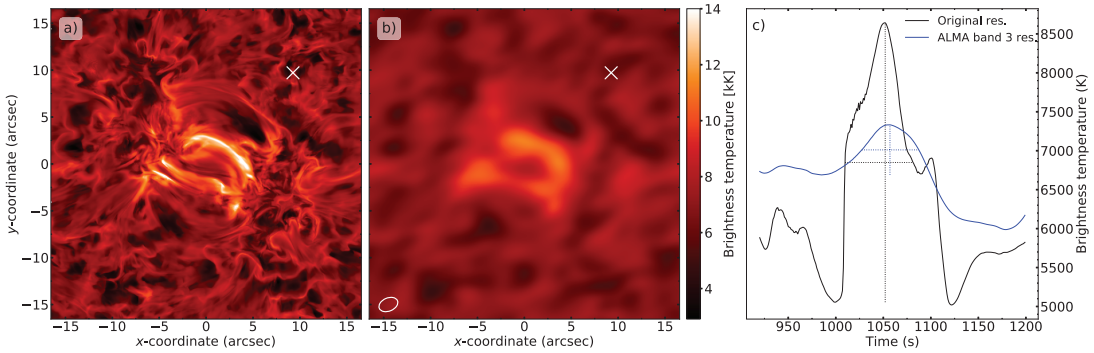

Fig. 12. Example of degradation with lower spatial resolution of shock wave T_b signature from the 3D Bifrost numerical model. (*a*) Synthetic brightness temperature map with a cell size of ∼0.066″ averaged over the frequencies of ALMA band 3 at $t = 1052$ s. The white cross marks the location of the selected event, $(x, y) = (9.26, 9.72)$ Mm. (*b*) The synthetic brightness temperature map degraded to the spatial resolution of the ALMA band 3 observations by convolution with the clean beam of observational data. The FWHM of the clean beam is marked by the white ellipse for reference. (*c*) Time evolution of the brightness temperature of the original and convolved maps at the selected location between $t = 920$ s and 1200 s. The vertical and horizontal dotted lines mark the T_b excess amplitude and lifetime of the shock wave signature in the respective resolution.

of event D could possibly be explained by the fact that it is unresolved. Nevertheless, the significant apparent motion spanning several pixels of the brightest points in examples A–C over their lifetimes brings reliability to the speed estimates.

The approach of looking for variations in the brightness temperature at a fixed location (time evolution for each pixel) gives, in principle, indications of all kinds of dynamical small-scale features. Out of the 552 registered events, it seems that most of the events exhibit an increase and decrease in brightness temperature at a more or less fixed (horizontal) location (see Figs. 2 and 7), as expected for a mostly vertically propagating shock wave. The peaks in the pixels associated with an individual event occur very close in time, separated by no more than a few seconds, indicating that the peaks are caused by the same underlying physical event. The majority of events show a speed of apparent motion very close to zero which could probably be a result of low spatial resolution with under-resolved events and a slight shift towards higher velocities could be expected with an increase in spatial resolution.

Many of the 552 detected events (Figs. 5–7) fulfill the aforementioned criteria which might suggest they do originate from shock waves. As a direct result of the selection process of the events, all of them show a high variation in brightness temperature. Approximately 95% of the events show an absolute LOS magnetic field strength lower than 20 G and an apparent speed of less than 30 km s^{-1}. Further, as discussed in Sect. 4.3, it is very plausible that the lifetimes indicated by the 1D simulations (Sect. 4.1) are underestimated and that longer lifetimes would be expected in the observations. Assuming that lifetimes could be as long as 100 s would result in more than half of all detected events potentially being produced by shock waves. However, further studies are required using more realistic numerical models to determine to what degree the lifetimes are underestimated.

4.6. Numerical simulations: 1D versus 3D

The shape of the temporal T_b profile of a shock wave signature in a 3D atmosphere often deviates significantly from the characteristic shape that is indicated in the 1D simulations. The shock wave is propagating through an inhomogenous 3D atmosphere, where disturbances from previous dynamics have made an imprint or the shock wave might be interfered by other simultaneous dynamics. Spatial smearing, as well as severely changing the amplitude of the T_b peak, might also considerably deform the temporal profile (see Fig. 12). The temporal profile is therefore highly dependent on the surrounding structure but can at least be used to validate clear cases. The numerical RADYN simulations in this study provide important insight into the expected signatures of shock waves as observed at mm wavelengths with ALMA. On the other hand, the restriction to one spatial dimension is detrimental to investigations in view of the complex three-dimensional structure of the solar atmosphere. The one-dimensional numerical models therefore only provide a first approximation of the radiative signatures of a propagating shock wave.

A more extensive study of 2D brightness temperature maps from numerical 3D simulations would provide a more realistic estimate and indication of the appearance of shock wave signatures at mm wavelengths as seen by ALMA. With these, the complexity of the 3D atmosphere would be accounted for. Also, the degree of degradation of dynamical fine structure that comes with limited spatial resolution can be determined, which by nature is not possible with a one-dimensional approach.

5. Conclusions and outlook

Analyzing an ALMA Band 3 (∼3 mm) observation of a disk-center quiet Sun region, we detected 552 small-scale dynamic events. An extensive study of the physical parameters of all events was carried out in order to characterise the events and reveal statistical trends. The possibility that the detected signatures come from shock wave events was examined. For that purpose, we used predictions of observable shock waves signatures at mm wavelengths from one-dimensional atmospheric models. The detected events show a large spread in brightness temperature excess (ΔT_b) reaching up to ∼1200 K for some very strong events and lifetimes of between ∼43 and 360 s. The typical values, represented by approximately half of the events, are ∼450–750 K and ∼55–125 s, respectively. However, most of the

events show a T_b excess that is smaller than predicted by the 1D simulations.

We conclude that the restriction to one spatial dimension is a severe limitation that cannot properly account for the small-scale chromospheric pattern as a product of complex 3D wave propagation. Observations with the limited spatial resolution of ALMA Band 3 are therefore subject to spatial smearing of the pattern, resulting in a strong reduction of the observable brightness temperature excess (ΔT_b).

Simulations of 3D shock wave propagation shown here and in previous studies (Wedemeyer-Böhm et al. 2007; Loukitcheva et al. 2015; Wedemeyer et al. 2020) demonstrate that the brightness temperature variations at mm wavelengths are strongly reduced as a result of limited spatial resolution as currently achieved with ALMA in Band 3. The magnitude of the dynamic T_b events seen in the observations could be considered as a lower limit. Based on these results, it is likely that the observed parameters are in line with the values predicted by the simulations when properly accounting for the dynamic 3D structure of the solar chromosphere and the effect of limited spatial resolution during the observation. Taking this into consideration, it seems plausible that many of the detected events have signatures originating in propagating shock waves. A more detailed study based on 3D numerical simulations is needed and will be presented in a forthcoming paper.

Acknowledgements. This work is supported by the SolarALMA project, which has received funding from the European Research Council (ERC) under the European Union's Horizon 2020 research and innovation programme (grant agreement No. 682462) and by the Research Council of Norway through its Centres of Excellence scheme, project number 262622. This paper makes use of the following ALMA data: ADS/JAO.ALMA#2016.1.00423.S. ALMA is a partnership of ESO (representing its member states), NSF (USA) and NINS (Japan), together with NRC(Canada), MOST and ASIAA (Taiwan), and KASI (Republic of Korea), in co-operation with the Republic of Chile. The Joint ALMA Observatory is operated by ESO, AUI/NRAO and NAOJ. We are grateful to the many colleagues who contributed to developing the solar observing modes for ALMA and for support from the ALMA Regional Centres. We also acknowledge collaboration with the Solar Simulations for the Atacama Large Millimeter Observatory Network (SSALMON, http://www.ssalmon.uio.no).

References

Alissandrakis, C. E., Patsourakos, S., Nindos, A., & Bastian, T. S. 2017, A&A, 605, A78
Carlsson, M., & Stein, R. F. 1992, ApJ, 397, L59
Carlsson, M., & Stein, R. F. 1994, in Chromospheric Dynamics, ed. M. Carlsson, 47
Carlsson, M., & Stein, R. F. 1997, ApJ, 481, 500
Carlsson, M., & Stein, R. F. 2002, ApJ, 572, 626
Carlsson, M., Hansteen, V. H., Gudiksen, B. V., Leenaarts, J., & De Pontieu, B. 2016, A&A, 585, A4
Carlsson, M., De Pontieu, B., & Hansteen, V. H. 2019, ARA&A, 57, 189
Cornwell, T. J. 2008, IEEE J. Sel. Top. Sign. Process., 2, 793
de la Cruz Rodríguez, J., & van Noort, M. 2017, Space Sci. Rev., 210, 109
de Wijn, A. G., Stenflo, J. O., Solanki, S. K., & Tsuneta, S. 2009, Space Sci. Rev., 144, 275
Dorfi, E. A., & Drury, L. O. 1987, J. Comput. Phys., 69, 175
Eklund, H., Wedemeyer, S., Snow, B., et al. 2020, Phil. Trans. A R. Soc., 379, 20200185
Everitt, B. 1972, Br. J. Psychiatry, 120, 143
Gafeira, R., Jafarzadeh, S., Solanki, S. K., et al. 2017, ApJS, 229, 7
Gudiksen, B. V., Carlsson, M., Hansteen, V. H., et al. 2011, A&A, 531, A154
Guevara Gómez, J. C., Jafarzadeh, S., Wedemeyer, S., et al. 2020, Phil. Trans. R. Soc. A., 379, 20200184
Jafarzadeh, S., Solanki, S. K., Gafeira, R., et al. 2017a, ApJS, 229, 9
Jafarzadeh, S., Solanki, S. K., Stangalini, M., et al. 2017b, ApJS, 229, 10
Jafarzadeh, S., Wedemeyer, S., Szydlarski, M., et al. 2019, A&A, 622, A150
Jafarzadeh, S., Wedemeyer, S., Fleck, B., et al. 2020, Phil. Trans. R. Soc. A, in press [arXiv:2010.01918]
Lemen, J. R., Title, A. M., Akin, D. J., et al. 2012, Sol. Phys., 275, 17
Loukitcheva, M., Solanki, S. K., Carlsson, M., & Stein, R. F. 2004, A&A, 419, 747
Loukitcheva, M., Solanki, S. K., & White, S. 2006, A&A, 456, 713
Loukitcheva, M., Solanki, S. K., & White, S. M. 2009, A&A, 497, 273
Loukitcheva, M., Solanki, S. K., Carlsson, M., & White, S. M. 2015, A&A, 575, A15
Loukitcheva, M. A., White, S. M., & Solanki, S. K. 2019, ApJ, 877, L26
Morton, R. J. 2012, A&A, 543, A6
Nindos, A., Alissandrakis, C. E., Bastian, T. S., et al. 2018, A&A, 619, L6
Okamoto, T. J., & De Pontieu, B. 2011, ApJ, 736, L24
Patsourakos, S., Alissandrakis, C. E., Nindos, A., & Bastian, T. S. 2020, A&A, 634, A86
Pereira, T. M. D., & Uitenbroek, H. 2015, A&A, 574, A3
Pesnell, W. D., Thompson, B. J., & Chamberlin, P. C. 2012, Sol. Phys., 275, 3
Rodger, A. S., Labrosse, N., Wedemeyer, S., et al. 2019, ApJ, 875, 163
Ryle, M. 1975, Science, 188, 1071
Schou, J., Scherrer, P. H., Bush, R. I., et al. 2012, Sol. Phys., 275, 229
Uitenbroek, H. 2001, ApJ, 557, 389
Vernazza, J. E., Avrett, E. H., & Loeser, R. 1981, ApJS, 45, 635
Wedemeyer, S., Freytag, B., Steffen, M., Ludwig, H. G., & Holweger, H. 2004, A&A, 414, 1121
Wedemeyer, S., Bastian, T., Brajša, R., et al. 2016, Space Sci. Rev., 200, 1
Wedemeyer, S., Szydlarski, M., Jafarzadeh, S., et al. 2020, A&A, 635, A71
Wedemeyer-Böhm, S., Ludwig, H. G., Steffen, M., Leenaarts, J., & Freytag, B. 2007, A&A, 471, 977
White, S. M., Iwai, K., Phillips, N. M., et al. 2017, Sol. Phys., 292, 88
Wilson, T. L., Rohlfs, K., & Hüttemeister, S. 2013, Tools of Radio Astronomy, Astron. Astrophys. Lib. (Springer-Verlag Berlin Heidelberg)
Wöger, F., Wedemeyer-Böhm, S., Schmidt, W., & von der Lühe, O. 2006, A&A, 459, L9

Appendix A: Example of a shock wave in a Bifrost 3D simulation

Figure A.1 shows the evolution of the gas temperature in a small region of the solar atmosphere as part of a 3D magneto-hydrodynamical simulation with the Bifrost code (Gudiksen et al. 2011; Carlsson et al. 2016). The displayed data exhibit an example of shock wave propagation. This example is used to illustrate the connection between the atmospheric thermal structure and the observable brightness temperature in mm-wavelength radiation maps as discussed in Sect. 4.2.

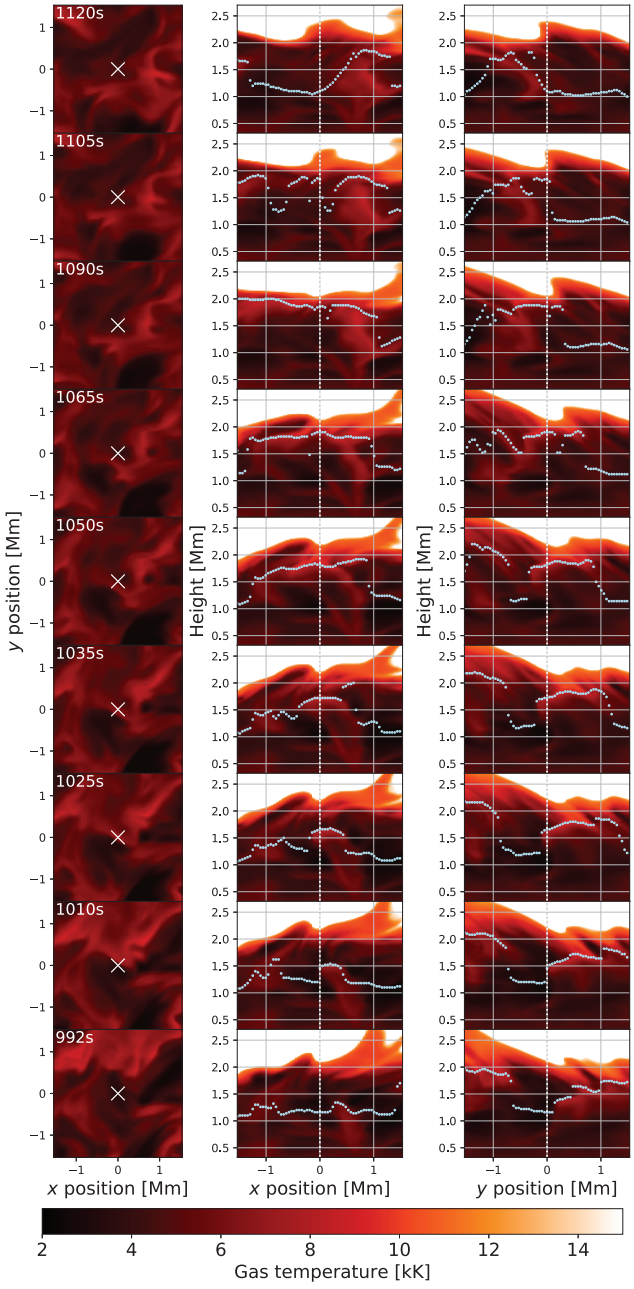

Fig. A.1. Illustration of a propagating shock wave in the Bifrost 3D simulation. Gas temperature surrounding the shock wave example is shown at nine time steps between $t = 992$ s and $t = 1120$ s of the simulation run. The *leftmost column* shows horizontal cuts (top-view) at a height of $z = 1.5$ Mm, and the *middle and rightmost columns* show vertical cuts with the height versus the x- and y-coordinates, respectively. The blue markers show the formation height of unity optical depth $\tau = 1.0$ for the mm wavelenghts of ALMA band 3 (2.78−3.26 mm). The white crosses and the vertical white dashed line at $(x, y) = (0, 0)$ mark the location of the sampled T_b signature in Fig. 12c. At $t = 992$ s the shock front is visible and the mm-wavelength intensities at $\tau = 1.0$ are coupled with it at $(x, y, z) = (0.3, 0.3, 1.2)$ Mm. The front is propagating mostly upwards and inwards towards $(x, y, z) = (0, 0, 1.6)$ Mm at $t = 1025$ s. The T_b signature is peaking in magnitude at this location around $t = 1050$ s, when a cooler post-shock region is visible where the front has passed. The mm-wavelength intensities are tracking the shock front upwards to $z \approx 2.0$ Mm around $t = 1090$ s and thereafter decouple and sample the post-shock region ($t = 1120$ s). See Eklund et al. (2020) for a more detailed analysis of propagating shock waves in the Bifrost simulation.

Appendix B: Detailed study of additional examples of brightness temperature events in the ALMA data

An additional couple of examples of T_b events found in the observational data are shown in detail. These events are marked as "B" and "D" in the figures in the main text.

Event B (see Fig. B.1) is located slightly closer to the magnetically stronger areas in the upper FOV at $(x, y) = (-0.2'', 3.4'')$, precisely on the border of the NW mask, though the absolute magnetic field strength is low at about 56 G. Event B shows a similar evolution in brightness temperature to event A. There is a rise in T_b from about 6890 K to 7960 K in 90 s followed by a decrease to about 6910 K over the course of 100 s. Event B has therefore a brightness temperature excess of $\Delta T_b = 1055$ K and a lifetime of 77 s. The profile of the temporal evolution of the brightness temperature (Fig. B.1h) shows a very similar shape to the fiducial run of the one-dimensional simulations. Event B, with a size of ~3″ at the temperature of FWHM of the main peak, shows an apparent motion of approximately 12 km s^{-1}.

Event D (Fig. B.2) at a location of $(x, y) = (-11.0'', -5.6'')$ shows a rapid increase in brightness temperature from 6585 K to 7160 K followed by a decrease to 6450 K. The resulting amplitude and lifetime are $\Delta T_b = 575$ K and 65 s, respectively. The event appears horizontally stationary without any strong indications of apparent motion. At the specific location there are hints of previous peaks of brightness temperature excess (Fig. B.2h), merely 200–300 K approximately 6 min and 3.5 min before event D.

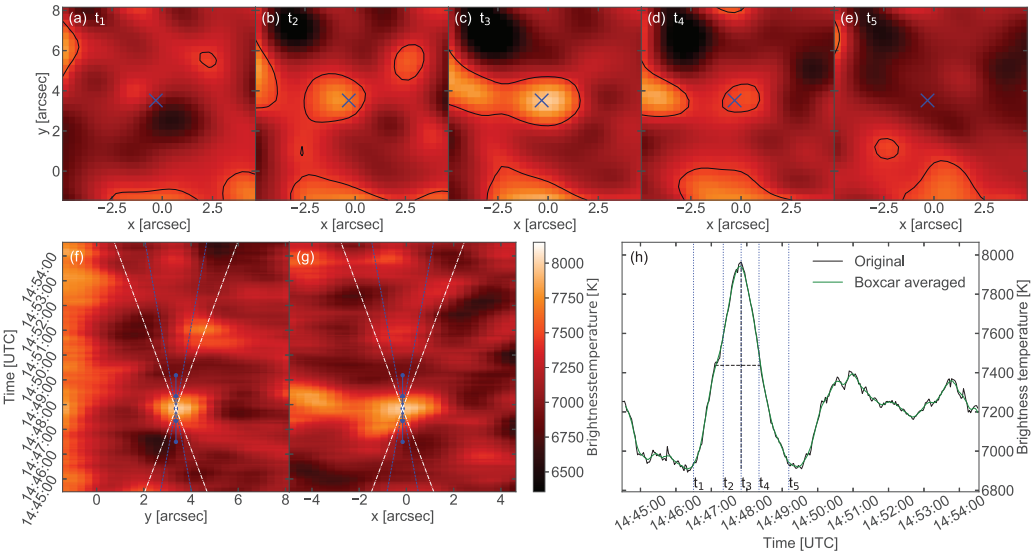

Fig. B.1. Detailed study of event B. (*a*)–(*e*) Close-ups of the surrounding brightness temperatures at different time steps, t_1 to t_5 *from left to right*, through the shock wave event. The time of the T_b peak is marked by t_3 = 14:47:50. Here, t_1, t_2, t_4 and t_5 mark −80, −30, 30, and 80 s from the peak, respectively. The contour lines mark the half maximum of the maximum ΔT_b peak and the blue crosses mark the center location. (*f*)–(*g*) Space-time diagrams for a vertical and horizontal slit across the FOV at the center location. The center location for time steps t_1 to t_5 is marked with blue dots connected with a line. Velocity slopes for 10 and 20 km s^{-1} are indicated by blue dotted and white dashed lines, respectively. (*h*) The time evolution of the brightness temperature of the center location, where the time steps t_1 to t_5 are indicated by blue dotted lines. Both the original data (black) and the averaged data (green) are shown. The horizontal and vertical dashed lines mark the event lifetime and brightness temperature excess, respectively.

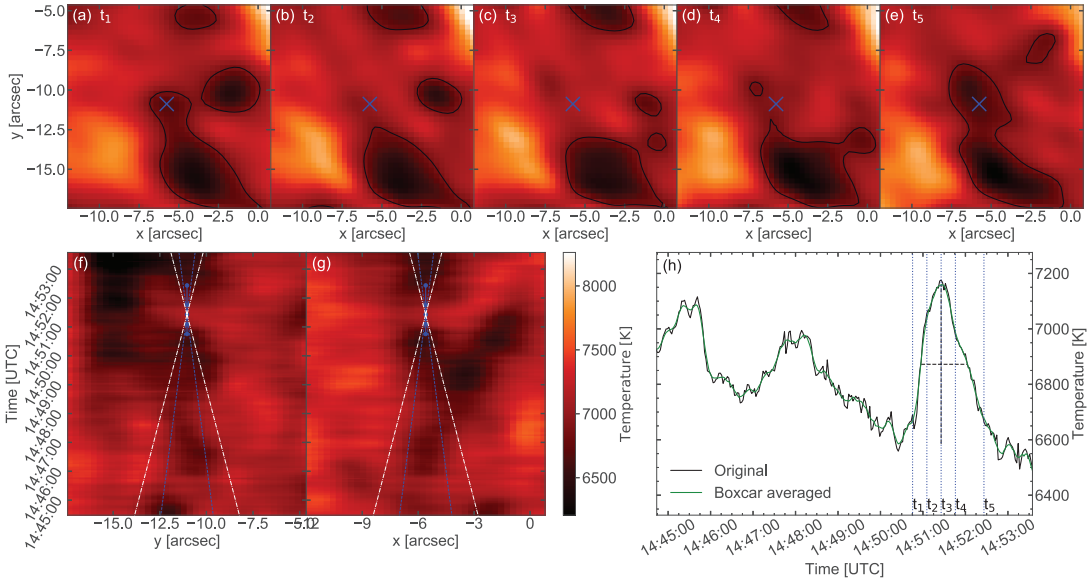

Fig. B.2. Detailed study of event D, as for event B in Fig. B.1. The time of the T_b peak is marked by t_3 = 14:51:25. t_1, t_2, t_4 and t_5 mark −40, −20, 20 and 40 s from the peak, respectively.

Paper II

Characterisation of shock wave signatures at millimetre wavelengths from Bifrost simulations

Henrik Eklund, Sven Wedemeyer, Ben Snow, David B. Jess, Shahin Jafarzadeh, Samuel D.T. Grant, Mats Carlsson, Mikołaj Szydlarski

Published in *Philosophical Transactions of the Royal Society A*, January 2021,

II

PHILOSOPHICAL TRANSACTIONS A

rsta.royalsocietypublishing.org

Research

Article submitted to journal

Subject Areas:
astrophysics, computational physics, computer modelling and simulation, solar system

Keywords:
shock waves, methods: numerical, Sun: chromosphere, Sun: photosphere, Sun: radio radiation

Author for correspondence:
Henrik Eklund
e-mail: henrik.eklund@astro.uio.no

Characterisation of shock wave signatures at millimetre wavelengths from Bifrost simulations

Henrik Eklund[1,2], Sven Wedemeyer[1,2], Ben Snow[3], David B. Jess[4,5], Shahin Jafarzadeh[1,2] , Samuel D.T. Grant[4], Mats Carlsson[1,2] and Mikołaj Szydlarski[1,2]

[1]Rosseland Centre for Solar Physics, University of Oslo, Postboks 1029 Blindern, N-0315 Oslo, Norway
[2]Institute of Theoretical Astrophysics, University of Oslo, Postboks 1029 Blindern, N-0315 Oslo, Norway
[3]Centre for Geophysical and Astrophysical Fluid Dynamics, University of Exeter, Exeter, UK
[4]Astrophysics Research Centre, School of Mathematics and Physics, Queen's University Belfast, Belfast, BT7 1NN, U.K.
[5]Department of Physics and Astronomy, California State University Northridge, Northridge, CA 91330, U.S.A.

THE ROYAL SOCIETY PUBLISHING

Observations at millimetre wavelengths provide a valuable tool to study the small scale dynamics in the solar chromosphere. We evaluate the physical conditions of the atmosphere in the presence of a propagating shock wave and link that to the observable signatures in mm-wavelength radiation, providing valuable insights into the underlying physics of mm-wavelength observations. A realistic numerical simulation from the 3D radiative Magnetohydrodynamic (MHD) code Bifrost is used to interpret changes in the atmosphere caused by shock wave propagation. High-cadence (1 s) time series of brightness temperature (T_b) maps are calculated with the Advanced Radiative Transfer (ART) code at the wavelengths 1.309 mm and 1.204 mm, which represents opposite sides of spectral band 6 of the Atacama Large Millimeter/submillimeter Array (ALMA). An example of shock wave propagation is presented. The brightness temperatures show a strong shock wave signature with large variation in formation height between ~ 0.7 to 1.4 Mm. The results demonstrate that millimetre brightness temperatures efficiently track upwardly propagating shock waves in the middle chromosphere. In addition, we show that the gradient of the brightness temperature between wavelengths within ALMA band 6 can potentially be utilised as a diagnostics tool in understanding the small-scale dynamics at the sampled layers.

1. Introduction

The solar atmosphere is highly dynamic at small scales at chromospheric heights, also under quiet-Sun conditions with low magnetic-field strength [1]. A major contribution to the small scale dynamics comes from the propagation of shock waves. Acoustic waves propagating upwards from the solar surface steepen into shock waves as a result of the decrease in gas density with height. The formation of shock waves and their propagation through the atmosphere have been studied by means of detailed one-dimensional numerical simulations, e.g., Ulmschneider [2], Stein and Schwartz [3], Kneer and Nakagawa [4], Ulmschneider et al. [5], Leibacher et al. [6], Ulmschneider et al. [7], Carlsson and Stein [8, 9, 10], Snow and Hillier [11, 12], Loukitcheva et al. [13, 14], Fleck and Schmitz [15].

Three-dimensional (3D) simulations, for instance those by [16], exhibit a dynamic mesh-like pattern of hot filaments from shock waves surrounding cooler post-shock regions. Such 3D simulations are also employed by [17] and [18] to explore the use of millimetre and submillimetre wavelengths as diagnostic tools for the chromosphere.

The complex dynamics in the chromosphere have also been reported in numerous observational studies. In particular, small-scale (on the order of 1.5 Mm and smaller) and short-lived (≈ 100 s or less) bright structures have been observed in the Ca II H and K spectral lines (the so-called H_{2V}/K_{2V} grains), in agreement with the mesh-like patterns seen in the simulations [19–22], which are often interpreted as shock signatures [23]. While [24] reported a correlation between these small-scale structures and a weak magnetic field of about 20 G, Lites et al. [25] and Cadavid et al. [26] found no clear relationship between magnetic fields and the K_{2V} grains. Other observational studies of small-scale shock signatures have also found that the magnetic field activity and orientation may play a major role in quiet Sun regions [27, 28], where shock waves propagate in both weak (or non-magnetised) and strong field-concentrated regions. Hasan and van Ballegooijen [29] showed that shock waves can produce excess temperatures of about 900 K in small magnetic concentrations in the chromosphere, which is responsible for the excess brightness observed in, e.g., small Ca II H magnetic bright points [30].

The radiation observed at millimetre wavelengths originates at chromospheric heights from free-free emission in local thermal equilibrium (LTE; see, e.g., [31] and references therein). Following the Rayleigh-Jeans law [i.e., 32], the measured intensities depend linearly on the local plasma temperature. In order to detect the small scale dynamics in observational mm-wavelength data, high spatial and temporal resolution is essential. In that regard, the Atacama Large millimetre/submillimetre Array (ALMA), which offers regular observations of the Sun

since 2016, represents a major step forward in terms of resolution, and has already provided insights into the dynamics of mm-wavelength intensities, e.g., [33–39]. Modelling has shown that propagating shock waves will cause variation in mm-wavelength observables [13, 14]. However, these studies employed 1D models, therefore it is uncertain to what degree the intensity variations are affected by more realistic interactions of shock waves in a 3D environment.

In this work, we use a 3D model that takes into account essential physical processes such as non-LTE and non-equilibrium hydrogen ionisation that have a large impact on the mm-wavelength radiation. With support from more realistic 3D simulations, it is possible to connect the mm-wavelength observables to the underlying physics and, thus, determine and characterise the observable signatures in mm-wavelengths of propagating shock waves.

The structure of the work is as follows. In Sect. 2, the setup of the simulations is explained and in Sect. 3 a representative example of a propagating shock wave with the surrounding physical conditions and the resulting signatures in brightness temperature are presented. In Sect. 4, we discuss the results and in Sect. 5 conclusions are drawn and motivation for future work is given.

2. Simulation setup

A three-dimensional numerical model of the solar atmosphere is created with the radiative magnetohydrodynamic (MHD) code Bifrost [40, 41]. The duration of the considered simulation sequence is approximately 1 hour with an output cadence of 1 s (matching the highest ALMA cadence in solar mode), so that rapid small-scale events on scales down to a few seconds can be efficiently studied. The simulation box has an extent of $24 \times 24 \times 17$ Mm in horizontal (x, y) and vertical (z) directions, respectively. The number of cells in x and y are both 504, with a constant grid spacing of 48 km (corresponding to approx. $0.066''$ at 1 AU). In the z-direction, there are 496 cells with grid spacing varying between 19 – 100 km, with a spacing of 20 km at chromospheric heights. In the horizontal directions, the boundary conditions are periodic. The bottom boundary, which is located 2.5 Mm under the photosphere, allows flows (e.g. intergranular downdrafts) through, however, the average horizontal pressure is driven towards a constant value at a characteristic time of 100 s. This gives rise to acoustic wave reflection, mimicking the refraction of waves in the solar convection zone and giving rise to p-modes in the simulation. The upper boundary condition is based on characteristic equations and allows for the transmission of magneto-acoustic waves.

The simulation takes into account non-LTE and non-equilibrium hydrogen ionisation, as Hydrogen is the major contributor to the number of free electrons. Ionisation of other elements are under the assumption of LTE and, thus, given as function of internal energy and total mass density. The simulation represents an 'enhanced network' region surrounded by quiet Sun [40]. The magnetic-field strength has an unsigned average value of 50 G (5 mT) at photospheric heights with two opposite polarity regions of magnetic field approximately 8 Mm apart.

The magnetic field was introduced into a relaxed convection simulation as two patches of opposite polarity at the lower boundary, with the rest of the simulation volume filled with a potential field extrapolation. This initial configuration is quickly modified by the convective flows that sweep the field into the intergranular lanes. The convective flows also cause foot point motions of the loops connecting the two polarities, leading to heating of the chromosphere and corona. The analysis of the simulation is restricted to later times (after 200s), when quasi-equilibrium has been established. For details of the setup and thermodynamic evolution of the simulation, see [40].

The same simulation with a cadence of 1 s has been used previously in the study by [36], to determine the diagnostic potential of solar ALMA observations. Other versions of the same simulation setup, but with lower cadence have been used in [18, 42], where the authors study chromospheric diagnostics at mm and sub-mm wavelengths with focus on the thermal structure and magnetic field.

The observable intensity at mm-wavelengths is obtained by solving the radiative transfer equation column by column. In LTE, the Rayleigh-Jeans approximation (valid for mm wavelengths) gives

$$T_{\rm B} = \int_{-\infty}^{\infty} \chi_\nu T_{\rm g} e^{-\tau_\nu} dz \,, \tag{2.1}$$

where $T_{\rm B}$ is the brightness temperature, χ_ν is the opacity, $T_{\rm g}$ is the gas temperature and τ_ν is the optical depth at height z defined from

$$\tau_\nu(z) = \int_{z}^{\infty} \chi_\nu dz \,. \tag{2.2}$$

The integrand in equation (2.1) is the contribution function, describing which regions along the line-of-sight that contribute to the observed brightness temperature. We use the Advanced Radiative Transfer (ART) code (de la Cruz Rodriguez et al., in prep.) to solve the radiative transfer equation. The code assumes LTE but includes in detail the relevant sources of continuum opacity. For ALMA wavelengths, the opacity is dominated by free-free processes of hydrogen and H^- (Loukitcheva et al 2004).

Two specific wavelengths are used in this study, located at the respective sides of the ALMA spectral band 6 in solar observing mode. The ALMA receiver band 6 is sub-divided into four sub-bands: SB1 (1.298 – 1.309 mm), SB2 (1.287 – 1.298 mm), SB3 (1.214 – 1.224 mm) and SB4 (1.204 – 1.214 mm). The wavelengths used here are 1.309 mm (229.0 GHz) and 1.204 mm (249.0 GHz), which are at the edges of SB1 and SB4, respectively. The brightness temperature, $T_b(\nu)$, is calculated from the radiative intensities, $I(\nu)$, through the Rayleigh-Jeans law approximation.

Figure 1 shows the brightness temperature for SB1 at a time of 200 s from the start of the simulation. Over the whole ~ 1 h of simulation time, there are many signatures associated with shock waves. An example of a shock wave event, further described in detail in Sect. 3, is located in the white circle marked in Fig. 1, at $(x, y) = (21.07, 0.72)$. The event is visualised in more detail in Fig. 2. This example is representative of a typical shock wave in the simulation box, whose characteristics are presented from a qualitative point of view.

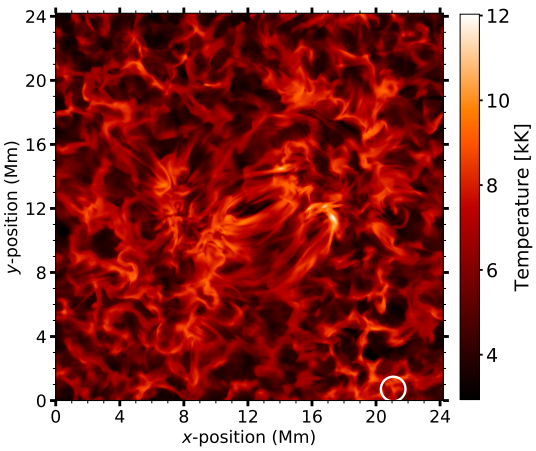

Figure 1. Brightness temperature in SB1 (1.309 mm; 229 GHz) at a time of 200 s after the beginning of the simulation. The white circle marks the location of the selected shock wave which is shown in more detail in Fig. 2

3. Example of shock wave

The regions surrounding the shock-wave event can be seen in the horizontal and vertical cuts of the gas temperature along the z-, x- and y-axis in Fig. 2. The vertical cuts are given for five time steps spread out over the time span of the shock event. The bottom row shows the pre-shock phase at $t = 150$ s, dominated by cooler down-flowing gas. In the second row from the bottom, at $t = 182$ s, the shock has formed and reached a height of ~ 1 Mm. In that moment, the brightness temperature is already at half its maximum value.

The third row shows the peak phase of brightness temperature at $t = 196$ s, where the shock front reaches a height of approximately 1.25 Mm. The fourth row from the bottom shows the time $t = 210$ s when the brightness temperature is at maximum for this location. At this time the shock wave front has reached above 1.5 Mm. Finally, in the top row at $t = 230$ s, the shock wave front has reached well above 2 Mm and the cool post-shock medium is evident at formation heights of SB1 and SB4 around ~ 0.8 Mm.

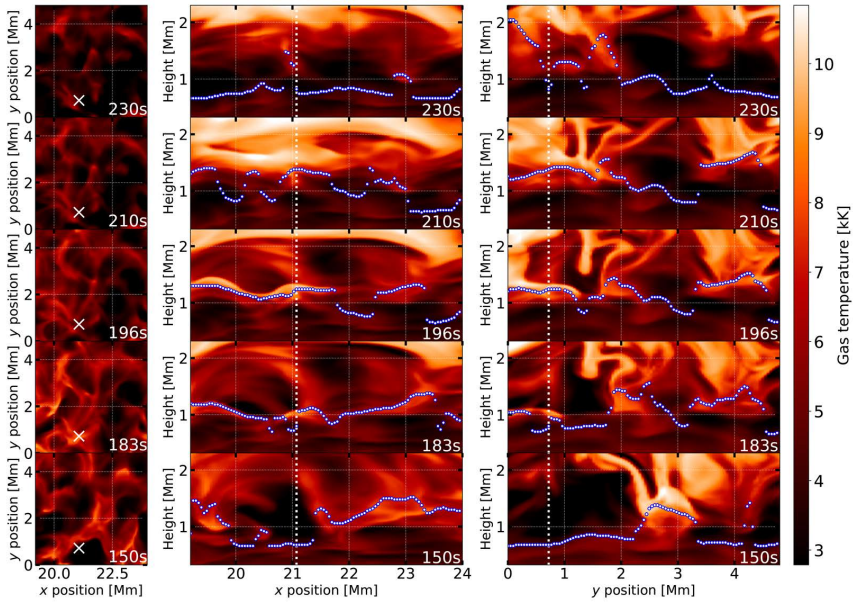

Figure 2. Gas temperature surrounding the example of shock wave formation for five different time steps, from bottom to top: $t = 150, 183, 196, 210$ and 230 s. First column: Horizontal cuts at a fixed height of 1 Mm above the photosphere. The white cross marks the coordinates of the shock wave, $(x, y) = (21.1, 0.72)$ Mm, which propagates largely in a vertical direction at these coordinates. Second and third column: Vertical cuts through this position along the x– and y–axis, respectively, showing heights between $\sim 0.4 - 2.3$ Mm. The white dotted lines marks the respective coordinate of the shock wave example. The blue dots show the height of optical depth $\tau = 1.0$ for SB1.

By comparing the cuts between the time steps, it is possible to see the propagation of the shock wave to a height of $z \approx 2.3$ Mm. The shock wave propagation is predominantly vertical along the z-axis, except for a small tilt along the y-axis that can be seen in the rightmost column of Fig. 2.

The ambient medium is highly dynamic, with a complex structure that leads to interactions between events. For instance, as the shock wave propagates through the chromosphere,

background waves and structures affect the shock front. The pre-shock medium, here seen around $t = 150\,\mathrm{s}$ (Fig. 2), is the resulting post-shock medium from preceding shock waves. Thus, the evolution of the shock wave front is dependent on how previous shock events influence the atmosphere. For this reason, it is necessary to use a realistic 3D atmospheric model in place of one-dimensional models in order to make predictions of the mm-wavelength signatures. The mm-wavelength radiation (marked in blue for $1.204\,\mathrm{mm}$ in Fig. 2) is also dependent on the local atmospheric conditions, with a range of formation heights between $\sim 0.6 - 2\,\mathrm{Mm}$.

(a) Contribution function to brightness temperature

The time-dependent contribution function of the brightness temperature of SB1 ($1.309\,\mathrm{mm}$) of the selected shock wave (see the location marked in Fig. 1) is given in Fig. 3. The corresponding contribution function for SB4 ($1.204\,\mathrm{mm}$), is similar, however, there are small differences resulting in differing heights of optical depth $\tau = 1.0$, marked by the blue and green dots in Fig. 3. A value for the optical depth of $\tau = 1.0$ is often a good one-point approximation to the full contribution function. As the shock wave front propagates upwards between the heights $z \approx 1.1 - 1.3\,\mathrm{Mm}$ (at $t \sim 190 - 210\,\mathrm{s}$), the span of the contribution function is very narrow. Here, the formation height that $\tau = 1.0$ corresponds to shows a strong correlation to, and effectively samples, the local gas temperature at a thin layer around the shock front. Immediately before $t = 190\,\mathrm{s}$, but mostly evident after $t = 210\,\mathrm{s}$, the brightness temperatures are sampled from several components at different heights. As the shock front propagates above $z \approx 1.5\,\mathrm{Mm}$, it is almost completely transparent in mm-wavelengths. There is a small fraction of the total contribution, no more than a few percent, that comes from the shock front at these heights, visible as a light grey streak in Fig 3. In the pre- and post-shock regimes, the contribution function spans a larger extent of heights.

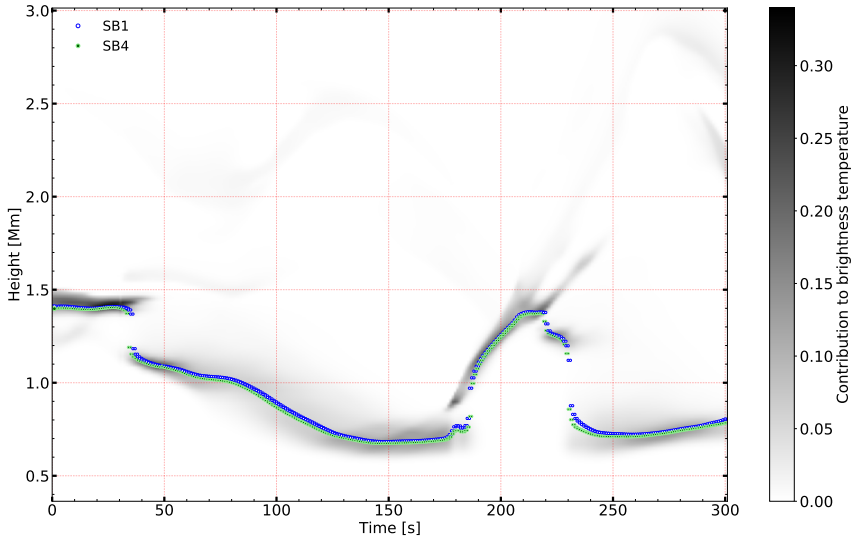

Figure 3. Time evolution of the contribution function for SB1 at $1.309\,\mathrm{mm}$. (The contribution function for SB4, at $1.204\,\mathrm{mm}$, differs slightly but looks nearly visually identical at these scales). For each time step, the heights of $\tau = 1.0$ for SB1 and SB4 are indicated by the blue and green markers, respectively. The integrated contribution function is normalised to 1.0.

(b) Gas and brightness temperature

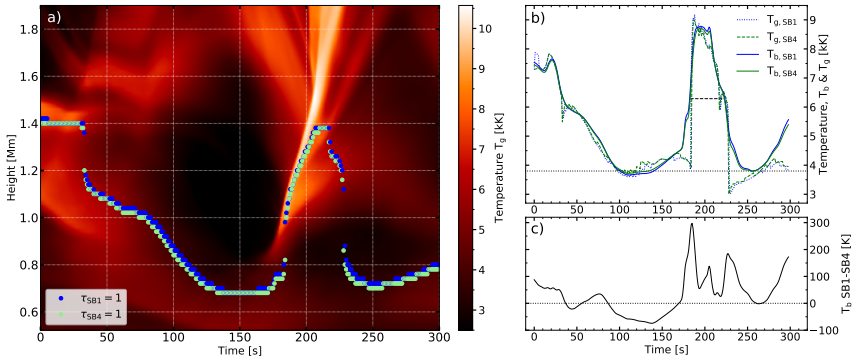

Figure 4. Time-dependent temperatures in the selected shock wave example. **a)** Evolution of gas temperature for one column at chromospheric heights between ~ 0.6 and 1.8 Mm. The blue and green dots mark the formation heights (i.e., $\tau = 1.0$) for the wavelengths 1.309 mm (SB1) and 1.204 mm (SB4), respectively. **b)** Evolution of the brightness temperatures (T_b) at wavelengths of 1.309 mm (SB1, blue solid) and 1.204 mm (SB4, green solid) and of the gas temperatures (T_g) at heights corresponding to the optical depth of unity at the respective wavelengths (blue/green dotted). The horizontal dashed black line represents the Full Width Half Maximum (FWHM) lifetime of the brightness temperature shock wave signature (with respect of the base temperature, dotted horizontal line). **c)** Evolution of the difference between the brightness temperatures of SB1 and SB4.

The time evolution of the gas temperature during the propagation of the selected shock wave is shown in Fig. 4a for heights between $z \approx 0.6 - 1.8$ Mm. In addition, the heights where the optical depth, τ, is unity at the wavelengths 1.309 mm (SB1) and 1.204 mm (SB4) are marked as a function of time. The wave steepens into a shock around t=175 s, close to a height of $z = 0.8$ Mm and thereafter shows a very rapid increase in height. This height for shock wave steepening is consistent with other studies [e.g., 16]. The formation height varies largely with time as the shock wave propagates through the chromosphere. There are small differences in the formation height between SB1 and SB4, of up to ~ 40 km with a median value of 20 km, although they follow the same trend and keep the same order. As can be seen in Fig. 4a, the height where $\tau = 1.0$ for both SB1 and SB4 increases from a pre-shock minimum of $z \approx 0.68$ Mm to a peak value of ~ 1.38 Mm during the course of 44 s with the propagation of the shock wave. The formation heights (i.e., $z(\tau = 1)$) thus increase by $\Delta z \sim 0.7$ Mm from the low to the middle chromosphere during the upward propagation of the shock wave.

From this point on, the formation heights no longer follow the upward propagating shock front. Instead, after about 10 s at the peak height, the formation heights rapidly decrease to $z = 0.72$ Mm in just 27 s and thus map the post-shock phase. The brightness temperatures map the hot propagating shock wave front up to a certain height where it decouples as a result of the lower opacity at these heights for the mm-wavelengths of SB1 and SB4.

Fig. 4b shows the corresponding evolution of the brightness temperatures of SB1 and SB4 as well as the gas temperature at the specific heights $z(\tau = 1.0)$ for SB1 and SB4, respectively. The brightness temperature of SB1 shows a total increase of ~ 4970 K in Δt=86 s, starting at a pre-shock local minimum of 3660 K at t=110 s and rising to the peak value of 8780 K at t=196 s. Thereafter, there is a rapid reduction to 3800 K at the local minimum at t=256 in the post-shock phase. The pre- and post-shock temperatures are thus comparable in this example. The local minimum with the highest temperature (here the post-shock minimum) is referred to as the

'base temperature'. The time between the two local minima is 146 s. Estimating the lifetime of the observable brightness temperature signature as the Full Width Half Maximum (FWHM) of the peak results in $t_{\mathrm{FWHM}} = 41$ s. The brightness temperature excess and lifetime shown here are in line with values derived from shock wave propagation in one-dimensional simulations ([13, 14] and Eklund et al., in prep.). The resulting strong correlation between the gas temperature at $z(\tau = 1.0)$ and the brightness temperature (Fig 4b) is expected for mm-wavelength radiation (see i.e., [18]).

Figure 4c shows the time evolution of the difference between the brightness temperatures of SB1 and SB4. In the pre-shock phase around 85 – 170 s there is a difference of down to -74 K, which corresponds to a magnitude of about 2 % of the total brightness temperature. Later during the shock phase, the difference between SB1 and SB4 increases to a total of 300 K, corresponding to 4 % of the total T_b, and finally decreases to approximately zero in the post-shock phase. The propagating shock wave and the pre-shock epoch display two different cases where the temperature gradient between the two sub-bands have a different sign. The brightness temperatures sampled at the propagation of the shock wave front show a positive gradient. That is, SB1 always forms in higher regions than SB4 and thus has a higher temperature. In contrast, during the pre-shock epoch, the gradient is negative and SB1 shows a lower temperature than SB4. The peaks in the time evolution of the brightness temperatures difference (Fig 4c) centered around ~ 185 s, 200 s and 230 s originates from the signatures of three distinct wave components with differing propagation speeds. These are seen in the $t - z$ plot of Fig. 4a as a hot, rapid component, followed by a cooler, slower component going upwards above 1.8 Mm and a third more diffuse component deflecting downwards around 1.2 Mm.

The rapid and large variations of the gas temperature at $z(\tau = 1.0)$ (Fig. 4b) are clearly connected to the large variations in formation height. The temporal profile of the brightness temperature (Fig 4b) is integrated over a span of heights along the specific column and is therefore smoother than the gas temperature, which is sampled at a single height.

(c) Vertical velocity

The evolution of the vertical velocity (v_z) at the chosen position (cf. Fig. 1) is shown in Fig. 5a. There is a bulk downflow of cooler gas (Fig. 4a) in the pre-shock region, with velocities of up to 20 km s^{-1}. The shock front is met by this downfall and, therefore, experiences a resistance to its motion as it propagates upwards. In the height range from where the mm continuum radiation in SB1 and SB4 originates, the vertical velocity only reaches a maximum velocity $v_z \sim 10$ km s^{-1}, whereas in the upper chromosphere, there are velocities of up to ~ 20 km s^{-1}. In Fig. 5a, the markings v_1, v_2, and v_3 point out the shock front at three different heights, $\sim 1.0, 1.3$ and 1.65 Mm. At these heights, the $t - z$ slope of the sharp transition of the vertical velocity (or the gas temperature in Fig. 4a) indicates a speed of the vertical propagation of the shock wave of ~ 33, 19 and 83 km s^{-1}, respectively.

The indications of differences in vertical velocity between heights of $z(\tau = 1.0)$ for SB1 and SB4 are generally small (i.e., smaller than 1 km s^{-1}). This is a due to the height difference between $z(\tau = 1.0)$ for SB1 and SB4 being of the same order as the vertical grid spacing of 20 km.

(d) Electron density

The time evolution of the electron density for the column of the shock wave is given in Fig. 6. During the pre-shock phase, the electron density is slowly decreasing in which the formation height of the brightness temperatures follows the same trend. There is a larger decrease followed by a rapid increase in the electron density around ~ 180 s as a result of the ionisation coming from the shock wave. In the post-shock regime, the electron density decreases slowly which combined with the declining gas temperature (Fig. 4) at some point (t 225 s) results in a sufficiently low opacity to initiate a sudden jump down in formation height of the mm-wave radiation. The

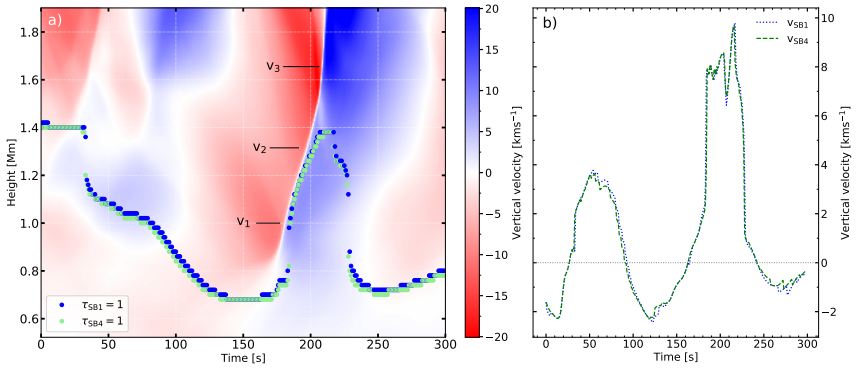

Figure 5. Time-dependent vertical velocities for the selected shock wave example. **a)** Evolution of vertical velocity for the chosen column (cf. Fig.1) at chromospheric heights between ~ 0.6 and 1.8 Mm. Positive velocity (blue color) indicates outwards motion away from the photosphere. The markings v_1, v_2 and v_3 show the vertical propagation speed of the shock front at different heights. The color scale is saturated on the positive side (from 23.7 to $20.1\,\mathrm{km\,s^{-1}}$). The blue and green dots mark the formation heights (i.e., $\tau = 1.0$) for the wavelengths 1.309 mm (SB1) and 1.204 mm (SB4), respectively. **b)** Evolution of vertical velocity at heights corresponding to the optical depth unity at the wavelengths for SB1 and SB4.

correlation of the gas temperature and electron density in shocks [43] is confirmed by the close relation of these quantities during the shock wave passage between 1.0 and 1.3 Mm.

The local atmosphere shows an increased electron density for a significant time span after the shock wave propagates through. [43] find through 1D models that the timescale of relaxation of the local atmosphere through hydrogen recombination after the shock wave has propagated through the chromosphere varies with height. They show a large span of timescales on the order of between $\sim 10^2 - 10^5$ s at chromospheric heights, with a peak value in the mid-chromosphere and rapidly decreasing towards both the photosphere and transition region. In Fig. 6c, the time evolution of the electron density at two fixed heights, 1.2 and 1.7 Mm are shown. The rate of decrease of electron density is slower at 1.7 Mm than at 1.2 Mm, for this shock wave. The relaxation times are difficult to measure due to the dynamic atmosphere with preceding, as well as succeeding, wave trains at the same position, ensuring that the electron density never reaches a steady state. Estimating the relaxation times by simply extrapolating with the same trend as for the last 30 s between 270 s and 300 s, results in ~ 200 s and ~ 430 s to reach values of previous minima at the heights 1.2 and 1.7 Mm, respectively.

The difference of the electron density between SB1 and SB4 is on the order of $\log(N_e) = 0.1\,\mathrm{cm^{-3}}$. The vertical grid spacing is in the same order as the differences in formation height $z(\tau = 1)$ of SB1 and SB4. Therefore, as with the velocities in Sect. (c), it is difficult to make use of the differences between electron density of SB1 and SB4 that are sampled at $z(\tau = 1)$.

The opacity of the mm-wavelengths is dominated by free-free processes (e.g., [44] and [13]) and is reduced by an increase in temperature coupled with a decrease in electron density. This behaviour is seen as the shock wave propagates upwards, resulting in a decrease of the opacity. At some point the opacity is reduced to the level where the brightness temperature de-couples from the shock wave front, leading to a rapid decrease in the formation height $z(\tau = 1)$.

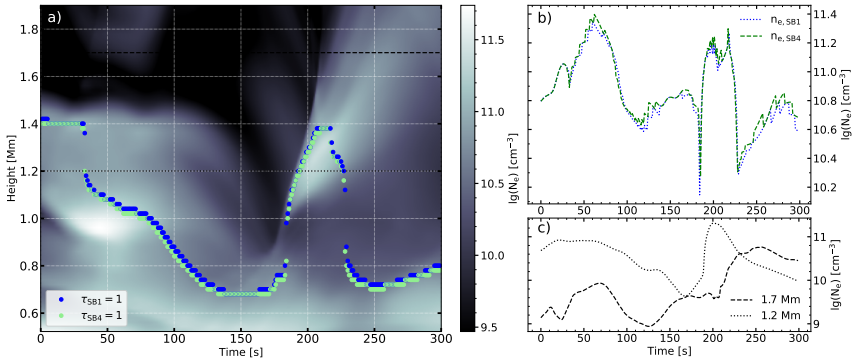

Figure 6. Time-dependent electron density for the selected shock wave example. **a)** Evolution of electron density for one column at chromospheric heights between ~ 0.6 and 1.8 Mm. The blue and green dots mark the formation heights (i.e., $\tau = 1.0$) for the wavelengths 1.309 mm (SB1) and 1.204 mm (SB4), respectively. The dotted and dashed horizontal lines marks the heights of 1.2 and 1.7 Mm. **b)** Evolution of electron density at heights corresponding to the optical depth of unity at the respective wavelengths of SB1 and SB4. **c)** Evolution of electron density at fixed heights of 1.2 and 1.7 Mm.

4. Discussion

The shock wave example illustrated in this work was found to be representative of a typical shock wave found in the simulation with respect to variations of gas temperature, vertical velocity and electron density. As a result of the complex 3D structure of the atmosphere, the propagation of the shock waves can be intricate, with differing speeds in different directions, alongside changes in the propagation angle of the wave-front. The shock wave example presented in this study exhibits a predominantly vertical propagation, which is to be expected for the region under consideration, with magnetic fields of minimal inclination. The temporal profile of a shock wave event will show deformations depending on the specific propagation properties at different locations (i.e., different columns). Thus, the vertical propagation of the shock front under consideration ensures a simple inference of the brightness temperature, absent of any large 3D components.

The formation height of mm-waves in the chromosphere is a function of wavelength, with height increasing with wavelength. Accordingly, SB1 forms slightly higher up than SB4. This is seen throughout the entire example of shock wave propagation in the chromosphere (Fig. 4a), despite the presence of small-scale dynamics in the chromosphere. The difference of 0.105 mm between SB1 and SB4 is shown to be enough to map different layers with brightness temperature differences up to ~ 300 K (Fig 4c). There are however notable variations in the differential between SB1 and SB4, sometimes to such a high degree that a reversal of the sub-bands are evident. The strongest reversal is seen in connection to the down-falling cold gas seen in the pre-shock region (~ 140 s) of the illustrated example.

With larger wavelength separation between the sampled sub-bands, larger T_b differences would be observed as the sampled layers would lie further apart. For that reason, it would be of interest in regards of the temporal domain to track a propagating shock wave from one layer to the other. Observations with ALMA with increased separation between the sub-bands would be favourable. Solar ALMA observations are currently offered in several spectral bands between $\sim 0.8 - 3.3$ mm. ALMA band 3 ($2.8 - 3.3$ mm) offers the largest default separation between the outermost sub-bands of 0.42 mm, which is ~ 4.5 times more than that of band 6 in this study. However, further consideration needs to be made, such as the change in formation height and, thus, potential change of shock wave propagation speed and contrast of the dynamic signatures.

(a) Contribution function spread over geometric height

Figure 3 reveals the important relationship between the developing shock and the associated $\tau = 1.0$ region. Importantly, it can be seen that during the initial formation of the shock (~ 180 s in Fig. 3), the plasma is both dense and bright, resulting in the observed signatures at the $\tau = 1.0$ location being dominated by the shocked plasma. Initially, this relationship continues to hold as the shock develops and propagates into higher layers of the chromosphere. However, at $t \sim 220$ s in Fig. 3, it can be seen that the contribution function defining the $\tau = 1.0$ surface begins to decouple from the upwardly propagating shock. At this point, the contribution function will be comprised of both shocked plasma expanding upwards into more diffuse and optically thin layers of the atmosphere, in addition to cooling plasma beginning to accelerate back towards the solar surface, which is visible in Figures. 4a and 5a. This results in the contribution function being spread over multiple components spanning a vast assortment of geometric heights. At this point, the signatures extracted at the $\tau = 1.0$ height no longer strictly correspond to the propagating shock, which has important implications for observational studies of such phenomena. For example, recent work surrounding shocks manifesting in sunspot umbrae [45, 46] have described the challenges faced when interpreting the spectropolarimetric fluctuations in Stokes $I/Q/U/V$ spectra over the lifetime of a shock. Hence, the opacity response of propagating shocks affects a wide range of observable signals, spanning brightness temperatures in the radio regime through polarimetric intensities across the visible and infrared spectrum. In particular, recent work by [46] interpreted reversals in the Stokes Q/U spectra as evidence for the presence of intermediate shocks, but this interpretation relied upon the observed signals being closely coupled to the developing shock front. As such, future investigations of challenging shock signatures (e.g. [47–49]) need to carefully consider the potential effects of the contribution function decoupling from the shock as it propagates into less opaque regions of the solar atmosphere.

(b) Observations compared to numerical simulations

Large advances have been made in interferometric observations of the Sun in mm-wavelengths, with ALMA. There are, however, many challenges that come with solar ALMA observations, for example, but not limited to, image reconstruction of interferometric data, limited spatial resolution, absolute temperature measurements, atmospheric noise, etc., that are out of the scope of this work.

The sophisticated 3D simulations give realistic predictions of how the shock wave signatures would look in brightness temperature as observed at mm-wavelengths. This work considers the brightness temperatures calculated at a horizontal resolution element of 48 km (~ 0.066 arcsec). Performing actual observations at these wavelengths comes with instrumental resolution limitations that need to be considered. Though further complications arise from the limited spatial resolution of observations, the results of this work point towards the optimistic capability of ALMA with highly resolved data. As a result of limited spatial resolution, the magnitude of the excess T_b of the dynamic profiles will appear less strong due to the pixel filling factor comprising of both the shocked plasma and cooler, quiescent plasma.

The estimated difference in formation height between the wavelengths 1.309 (SB1) and 1.204 mm (SB4) of up to 40 km with a median value of 20 km is on the limit of the vertical grid spacing of the simulation. The vertical resolution of 20 km in the chromosphere puts a limit on the differences of the small scale dynamics that can be handled. To study the differences between the sub-bands in more detail, a higher resolved numerical model would be necessary.

Observations also come with a certain amount of noise. The signal-to-noise ratio needs to be high enough to accurately deal with the magnitude of T_b variations of interest. A few studies of ALMA data have been made where T_b variations of small scale structures have been reported [34–36]. In these studies, the brightness temperatures of the full spectal bands (all four sub-bands combined) were used. Integration over larger spectral or temporal spans can be done in

order to increase the signal-to-noise ratio. To accurately map the T_b differences between two sub-bands introduces a larger uncertainty. There are studies where the sub-bands are successfully used separately [50, 51], which in this case acts as a proof of concept. Detection of brightness temperature variations as small as 70 K has been reported by [35], where they use ALMA observations at ~ 3 mm (band 3) with integration over the full band with a cadence of 2 s. The spatial resolution element of their band 3 data ($2.5'' \times 4.5''$), is larger than what currently can be achieved with band 6 data around 1.204–1.309 mm. This is a direct result of the Fourier sampling (fringe spacing) of the interferometric data scales with wavelength [i.e., 32]. With regards to the ability to spatially resolve small scale events, the ability to measure precise brightness temperatures should therefore be even more precise in band 6 than in band 3. However, the integration over the full band comes with the inherent loss of sampling different layers as a function of wavelength. There should be an optimal combination of improving upon the signal-to-noise ratio whilst sampling different layers within a spectral band, so that differences on the order of one hundred Kelvin can be detected, as indicated by the T_b difference between the sub-bands in the simulations (Fig. 4c).

Estimating the observable signatures of shock waves in mm-wavelengths with current and potential future modes offered for solar-ALMA observations, including the effect of limited spatial resolution of different spectral bands and the sampling of different physics between the sub-bands will be investigated in a forthcoming paper.

5. Conclusion

We use realistic numerical 3D MHD simulations from the Bifrost code, including non-LTE, non-equilibrium hydrogen ionisation, of the solar atmosphere to study small scale dynamics connected to propagating shock waves and how these are perceived in mm-wavelength radiation. An example of a shock wave with nearly vertical propagation and without much interference from neighbouring dynamical features is illustrated. The shock wave propagating upwards in the chromosphere at vertical velocities between $\sim 19 - 83$ km s^{-1}, and has an assosiated increase in the local gas temperature of the order of several thousand degrees. We conclude that the brightness temperature at mm-wavelengths corresponding to ALMA band 6 (1.204 – 1.309 mm) probes these gas temperatures accurately under the highly dynamical conditions arising from propagating shock waves. The gas temperature at a single height $z(\tau = 1.0)$ is quite close to the brightness temperature, which demonstrates the close relationship and the diagnostic potential for determining actual gas temperatures from mm-wavelength observations. The FWHM lifetime of the T_b shock wave signature is 41 s.

The formation height of the radiation at a certain wavelength is not fixed. The formation height of wavelengths 1.204 – 1.309 mm varies on the order of ~ 0.7 Mm, from ~ 0.7 to ~ 1.4 Mm in less than a minute, in the course of the shock wave propagating through the chromosphere. The brightness temperatures at wavelengths corresponding to ALMA band 6 at 1.204 – 1.309 mm efficiently maps the shock front while it is propagating from approximately 1.0 Mm up to 1.4 Mm, where the brightness temperatures start to decouple and instead starts to map the post-shock region. The shock wave front continues propagating upwards, unseen by radiation at 1.204 – 1.309 mm. In the pre and post-shock regimes, the radiative contribution function at these wavelengths is more diffuse and spread out over larger span of heights. At some instances, the brightness temperature (at one frequency) has contributions from distinct layers at different heights. This is the scenario right before and after the strong coupling of the brightness temperature with the shock front.

There is a wavelength dependency of the optical depth which has been explored for wavelengths lying in the furthest apart sub-bands of ALMA spectral band 6. The simulations indicate that the difference in formation height between wavelengths SB1 and SB4 is up to approximately 40 km with a median difference of 20 km. The order of the formation heights with SB1 forming higher up than SB4, is however constant. Because of the correlation between the formation height and the wavelength of radiation, the gradient of brightness temperatures

within the spectral band corresponds to a gradient in plasma temperature between the respective formation heights. The brightness temperatures of SB1 and SB4 show differences from about -70 K up to ~ 300 K in the shock wave example. The difference between the sub-bands comes from the local temperature gradient between the mapped layers at the formation heights of the sub-bands. As the brightness temperature is coupled to the shock wave front, SB1 (1.204 mm) has a higher temperature than SB4 (1.309 mm) and there is a positive gradient with increasing temperature with height. In the pre- or post-shock regimes dominated by sampling of cold down flowing gas, the temperature gradient tends to be negative with SB1 colder than SB4.

The presented simulation results demonstrate that brightness temperatures of wavelengths corresponding to ALMA spectral band 6 (1.204 – 1.309 mm) can be used for tracking shock waves from the middle chromosphere and that the gradient of the brightness temperature within the spectral band in principle can be utilised as a diagnostics tool for probing the small-scale structure of the chromosphere.

Data Accessibility.

The Bifrost simulation with 10 s cadence is publicly available at: http://sdc.uio.no/search/simulations

Authors' Contributions. MS and MC performed the MHD simulations and radiative transfer computations. HE performed scientific analysis, with assistance from SW, BS, DBJ, SJ, SDTG, and MC. HE drafted the manuscript. All authors read and approved the manuscript.

Competing Interests. The authors declare that they have no competing interests.

Funding. This work is supported by the SolarALMA project, which has received funding from the European Research Council (ERC) under the European Union's Horizon 2020 research and innovation programme (grant agreement No. 682462) and by the Research Council of Norway through its Centres of Excellence scheme, project number 262622 (Rosseland Centre for Solar Physics). The development of the Advanced Radiative Transfer (ART) code was supported by the PRACE Preparatory Access Type D program (proposal 2010PA3776). Grants of computing time from the Norwegian Programme for Supercomputing are acknowledged. BS is supported by STFC research grant ST/R000891/1. DBJ and SDTG are supported by an Invest NI and Randox Laboratories Ltd. Research & Development Grant (059RDEN-1).

Acknowledgements. DBJ and SDTG are grateful to Invest NI and Randox Laboratories Ltd. for the award of a Research & Development Grant (059RDEN-1). We also acknowledge collaboration with the Solar Simulations for the Atacama Large Millimeter Observatory Network (SSALMON, http://www.ssalmon.uio.no). The support by M. Krotkiewski from USIT, University of Oslo, Norway, for the technical development of ART is gratefully acknowledged. BS, DBJ, SJ, and SDTG wish to acknowledge scientific discussions with the Waves in the Lower Solar Atmosphere (WaLSA; www.WaLSA.team) team, which is supported by the Research Council of Norway (project no. 262622) and the Royal Society (award no. Hooke18b/SCTM).

References

1. Carlsson M, Judge PG, Wilhelm K. 1997, SUMER Observations Confirm the Dynamic Nature of the Quiet Solar Outer Atmosphere: The Internetwork Chromosphere. *ApJ*, 486(1):L63–L66. (doi: 10.1086/310836)
2. Ulmschneider P. 1970, On Frequency and Strength of Shock Waves in the Solar Atmosphere. *Sol. Phys.*, 12(3):403–415. (doi: 10.1007/BF00148023)
3. Stein RF, Schwartz RA. 1973, Waves in the Solar Atmosphere. III. The Propagation of Periodic Wave Trains in a Gravitational Atmosphere. *ApJ*, 186:1083–1090. (doi: 10.1086/152572)
4. Kneer F, Nakagawa Y. 1976, Radiative hydrodynamics of chromospheric transients. *A&A*, 47 (1):65–76
5. Ulmschneider R, Schmitz F, Kalkofen W, Bohn HU. 1978, Acoustic Waves in the Solar Atmosphere. V. On the Chromospheric Temperature Rise. *A&A*, 70:487
6. Leibacher J, Gouttebroze P, Stein RF. 1982, Solar atmospheric dynamics. II - Nonlinear models of the photospheric and chromospheric oscillations. *ApJ*, 258:393–403. (doi: 10.1086/160089)
7. Ulmschneider P, Priest ER, Rosner R. 1991, *Mechanisms of Chromospheric and Coronal Heating (Springer-Verlag, Berlin)*

8. Carlsson M, Stein RF. 1992, Non-LTE Radiating Acoustic Shocks and CA II K2V Bright Points. *ApJ*, 397:L59. (doi: 10.1086/186544)
9. Carlsson M, Stein RF. 1994, 47, *Chromospheric Dynamics*pages
10. Carlsson M, Stein RF. 1997, Formation of Solar Calcium H and K Bright Grains. *ApJ*, 481(1): 500–514. (doi: 10.1086/304043)
11. Snow B, Hillier A. 2019, Intermediate shock sub-structures within a slow-mode shock occurring in partially ionised plasma. *A&A*, 626:A46. (doi: 10.1051/0004-6361/201935326)
12. Snow B, Hillier A. 2020, Mode conversion of two-fluid shocks in a partially-ionised, isothermal, stratified atmosphere. *A&A*, 637:A97. (doi: 10.1051/0004-6361/202037848)
13. Loukitcheva M, Solanki SK, Carlsson M, Stein RF. 2004, Millimeter observations and chromospheric dynamics. *A&A*, 419:747–756. (doi: 10.1051/0004-6361:20034159)
14. Loukitcheva M, Solanki SK, White S. 2006, The dynamics of the solar chromosphere: comparison of model predictions with millimeter-interferometer observations. *A&A*, 456(2): 713–723. (doi: 10.1051/0004-6361:20053171)
15. Fleck B, Schmitz F. 1993, On the interactions of hydrodynamic shock waves in stellar atmospheres. *A&A*, 273:671
16. Wedemeyer S, Freytag B, Steffen M, Ludwig HG, Holweger H. 2004, Numerical simulation of the three-dimensional structure and dynamics of the non-magnetic solar chromosphere. *A&A*, 414:1121–1137. (doi: 10.1051/0004-6361:20031682)
17. Wedemeyer-Böhm S, Ludwig HG, Steffen M, Leenaarts J, Freytag B. 2007, Inter-network regions of the Sun at millimetre wavelengths. *A&A*, 471(3):977–991. (doi: 10.1051/0004-6361:20077588)
18. Loukitcheva M, Solanki SK, Carlsson M, White SM. 2015, Millimeter radiation from a 3D model of the solar atmosphere. I. Diagnosing chromospheric thermal structure. *A&A*, 575: A15. (doi: 10.1051/0004-6361/201425238)
19. Rutten RJ, Uitenbroek H. 1991, Ca uc(ii) H_{2v} and K_{2v} cell grains. *Sol. Phys.*, 134(1):15–71. (doi: 10.1007/BF00148739)
20. Kneer F, von Uexkuell M. 1993, Oscillations of the Sun's chromosphere. VI. K grains, resonances, and gravity waves. *A&A*, 274:584–594
21. Hofmann J, Steffens S, Deubner FL. 1996, K-grains as a three-dimensional phenomenon. II. Phase analysis of the spatio-temporal pattern. *A&A*, 308:192–198
22. Wöger F, Wedemeyer-Böhm S, Schmidt W, von der Lühe O. 2006, Observation of a short-lived pattern in the solar chromosphere. *A&A*, 459(1):L9–L12. (doi: 10.1051/0004-6361:20066237)
23. Beck C, Schmidt W, Rezaei R, Rammacher W. 2008, The signature of chromospheric heating in Ca II H spectra. *A&A*, 479(1):213–227. (doi: 10.1051/0004-6361:20078410)
24. Sivaraman KR, Livingston WC. 1982, Ca ii K_{2V} spectral features and their relation to small-scale photospheric magnetic fields. *Sol. Phys.*, 80(2):227–231. (doi: 10.1007/BF00147970)
25. Lites BW, Rutten RJ, Kalkofen W. 1993, Dynamics of the Solar Chromosphere. I. Long-Period Network Oscillations. *ApJ*, 414:345. (doi: 10.1086/173081)
26. Cadavid AC, Lawrence JK, Berger TE, Ruzmaikin A. 2003, Photospheric Sources and Brightening of the Internetwork Chromosphere. *ApJ*, 586(2):1409–1416. (doi: 10.1086/367833)
27. Cauzzi G, Reardon KP, Vecchio A, Janssen K, Rimmele T. 2007, , *The Physics of Chromospheric Plasmas*, 127volume 368 of *Astronomical Society of the Pacific Conference Series*pages
28. Vecchio A, Cauzzi G, Reardon KP. 2009, The solar chromosphere at high resolution with IBIS. II. Acoustic shocks in the quiet internetwork and the role of magnetic fields. *A&A*, 494(1): 269–286. (doi: 10.1051/0004-6361:200810694)
29. Hasan SS, van Ballegooijen AA. 2008, Dynamics of the Solar Magnetic Network. II. Heating the Magnetized Chromosphere. *ApJ*, 680(2):1542–1552. (doi: 10.1086/587773)
30. Jafarzadeh S, Solanki SK, Feller A, Lagg A, Pietarila A, Danilovic S, Riethmüller TL, Martínez Pillet V. 2013, Structure and dynamics of isolated internetwork Ca II H bright points observed by SUNRISE. *A&A*, 549:A116. (doi: 10.1051/0004-6361/201220089)
31. Wedemeyer S, Bastian T, Brajša R, Hudson H, Fleishman G, Loukitcheva M, Fleck B, Kontar EP, De Pontieu B, Yagoubov P, Tiwari SK, Soler R, Black JH, Antolin P, Scullion E, Gunár S,

Labrosse N, Ludwig HG, Benz AO, White SM, Hauschildt P, Doyle JG, Nakariakov VM, Ayres T, Heinzel P, Karlicky M, Van Doorsselaere T, Gary D, Alissandrakis CE, Nindos A, Solanki SK, Rouppe van der Voort L, Shimojo M, Kato Y, Zaqarashvili T, Perez E, Selhorst CL, Barta M. 2016, Solar Science with the Atacama Large Millimeter/Submillimeter Array—A New View of Our Sun. *Space Sci. Rev.*, 200(1-4):1–73. (doi: 10.1007/s11214-015-0229-9)

32. Wilson TL, Rohlfs K, Hüttemeister S. 2013, *Tools of Radio Astronomy*. (doi: 10.1007/978-3-642-39950-3)
33. Shimojo M, Hudson HS, White SM, Bastian TS, Iwai K. 2017, The First ALMA Observation of a Solar Plasmoid Ejection from an X-Ray Bright Point. *ApJ*, 841(1):L5. (doi: 10.3847/2041-8213/aa70e3)
34. Nindos A, Alissandrakis CE, Bastian TS, Patsourakos S, De Pontieu B, Warren H, Ayres T, Hudson HS, Shimizu T, Vial JC, Wedemeyer S, Yurchyshyn V. 2018, First high-resolution look at the quiet Sun with ALMA at 3mm. *A&A*, 619:L6. (doi: 10.1051/0004-6361/201834113)
35. Nindos A, Alissandrakis CE, Patsourakos S, Bastian TS. 2020, Transient brightenings in the quiet Sun detected by ALMA at 3 mm. *arXiv e-prints*, art. arXiv:2004.07591
36. Wedemeyer S, Szydlarski M, Jafarzadeh S, Eklund H, Guevara Gomez JC, Bastian T, Fleck B, de la Cruz Rodriguez J, Rodger A, Carlsson M. 2020, The Sun at millimeter wavelengths. I. Introduction to ALMA Band 3 observations. *A&A*, 635:A71. (doi: 10.1051/0004-6361/201937122)
37. Patsourakos S, Alissandrakis CE, Nindos A, Bastian TS. 2020, Observations of solar chromospheric oscillations at 3 mm with ALMA. *A&A*, 634:A86. (doi: 10.1051/0004-6361/201936618)
38. Jafarzadeh S, Wedemeyer S, Fleck B, Stangalini M, , Jess DB, Morton RJ, Szydlarski M, Henriques VMJ, Zhu X, Wiegelmann T, Guevara Gómez JC, Grant SDG, Chen B, Reardon K, White SM. 2020, An overall view of temperature oscillations in the solar chromosphere with ALMA. *Phil. Trans. R. Soc. A.*, (current issue)
39. Guevara Gómez JC, Jafarzadeh S, Wedemeyer S, Szydlarski M, Stangalini M, Fleck B, Keys PH. 2020, High-frequency oscillations in small chromospheric bright features observed with ALMA. *Phil. Trans. R. Soc. A.*, (current issue)
40. Carlsson M, Hansteen VH, Gudiksen BV, Leenaarts J, De Pontieu B. 2016, A publicly available simulation of an enhanced network region of the Sun. *A&A*, 585:A4. (doi: 10.1051/0004-6361/201527226)
41. Gudiksen BV, Carlsson M, Hansteen VH, Hayek W, Leenaarts J, Martínez-Sykora J. 2011, The stellar atmosphere simulation code Bifrost. Code description and validation. *A&A*, 531:A154. (doi: 10.1051/0004-6361/201116520)
42. Loukitcheva M, White SM, Solanki SK, Fleishman GD, Carlsson M. 2017, Millimeter radiation from a 3D model of the solar atmosphere. II. Chromospheric magnetic field. *A&A*, 601:A43. (doi: 10.1051/0004-6361/201629099)
43. Carlsson M, Stein RF. 2002, Dynamic Hydrogen Ionization. *ApJ*, 572(1):626–635. (doi: 10.1086/340293)
44. Dulk GA. 1985, Radio emission from the sun and stars. *ARA&A*, 23:169–224. (doi: 10.1146/annurev.aa.23.090185.001125)
45. de la Cruz Rodríguez J, Rouppe van der Voort L, Socas-Navarro H, van Noort M. 2013, Physical properties of a sunspot chromosphere with umbral flashes. *A&A*, 556:A115. (doi: 10.1051/0004-6361/201321629)
46. Houston SJ, Jess DB, Keppens R, Stangalini M, Keys PH, Grant SDT, Jafarzadeh S, McFetridge LM, Murabito M, Ermolli I, Giorgi F. 2020, Magnetohydrodynamic Nonlinearities in Sunspot Atmospheres: Chromospheric Detections of Intermediate Shocks. *ApJ*, 892(1):49. (doi: 10.3847/1538-4357/ab7a90)
47. Houston SJ, Jess DB, Asensio Ramos A, Grant SDT, Beck C, Norton AA, Krishna Prasad S. 2018, The Magnetic Response of the Solar Atmosphere to Umbral Flashes. *ApJ*, 860(1):28. (doi: 10.3847/1538-4357/aab366)
48. Joshi J, de la Cruz Rodríguez J. 2018, Magnetic field variations associated with umbral flashes and penumbral waves. *A&A*, 619:A63. (doi: 10.1051/0004-6361/201832955)

49. Grant SDT, Jess DB, Zaqarashvili TV, Beck C, Socas-Navarro H, Aschwanden MJ, Keys PH, Christian DJ, Houston SJ, Hewitt RL. 2018, Alfvén wave dissipation in the solar chromosphere. *Nature Physics*, 14(5):480–483. (doi: 10.1038/s41567-018-0058-3)
50. Rodger AS, Labrosse N, Wedemeyer S, Szydlarski M, Simões PJA, Fletcher L. 2019, First Spectral Analysis of a Solar Plasma Eruption Using ALMA. *ApJ*, 875(2):163. (doi: 10.3847/1538-4357/aafdfb)
51. Jafarzadeh S, Wedemeyer S, Szydlarski M, De Pontieu B, Rezaei R, Carlsson M. 2019, The solar chromosphere at millimetre and ultraviolet wavelengths. I. Radiation temperatures and a detailed comparison. *A&A*, 622:A150. (doi: 10.1051/0004-6361/201834205)